Experimental & Numerical micro-EDM Surface Treatments of New Generation Titanium Biomedical Alloys

Shahid Ali, B.Eng. in Mechanical Engineering

Submitted in fulfillment of the requirements

for the degree of Master of Science

in Mechanical & Aerospace Engineering

NAZARBAYEV UNIVERSITY

School of Engineering and Digital Sciences

Department of Mechanical & Aerospace Engineering

Nazarbayev University

53 Kabanbay Batyr Avenue,

Nur-Sultan city, Kazakhstan, 010000

Supervisor: Associate Professor Asma Perveen

Co-supervisor: Associate Professor Didier Talamona

March 2024

Declaration form

I hereby declare that this manuscript, entitled “Experimental & Numerical micro-EDM Surface Treatments of New Generation Titanium Biomedical Alloys”, is the result of my work except for quotations and citations, which have been duly acknowledged.

I also declare that, to the best of my knowledge and belief, it has not been previously or concurrently submitted, in whole or in part, for any other degree or diploma at Nazarbayev University or any other national or international institution.

Name: Shahid Ali

Dated: April 05, 2024

Abstract

Despite advancements in material science, biomedicine, and orthopedic implant applications continue to encounter numerous challenges. The prevalence of implant failures in long-term applications serves as a significant motivation for ongoing research aimed at reducing the likelihood of such failures. Titanium and its new-generation alloys are widely employed in high-end applications due to their special properties, such as corrosion resistance, biocompatibility, Young's modulus, and strength-to-weight ratio. This unique blend of qualities positions titanium alloys as highly sought-after materials in sectors, such as biomedical, aerospace, automotive, sports equipment, etc. Modern industries frequently use micro–Electro micro-electro-discharge machining (μ-EDM), a non-conventional machining technique that is especially useful for processing hard materials like titanium alloys. μ-EDM can produce intricate shapes with excellent dimensional precision. The main emphasis of this work is an experimental analysis of the μ-EDM of TNZT alloys employing a tungsten carbide (WC) electrode. The results for micro-EDM of Ti-35Nb-7Zr-5Ta showed that with the increase in process parameters capacitance (C) from 10nF to 100nF at Voltage (V) 80V, the machining performance parameters such as material removal rate (MRR), overcut (OC), crater size, surface microhardness, surface roughness, and crater size increase by 6.38, 1.523, 4.496 1.069, and 1.803 times respectively. However, the circularity of the μ-hole decreases by 1.099 times. This study intends to show how the two key machining factors (C & V) influence significant machining performance parameters. The influence of capacitance on machining performance variables is more dominant.

Additionally, this study introduces an analytical model rooted in electro-thermal theory to estimate the size of micro-craters in micro-electrical discharge machining (μ-EDM). Addressing the challenge of the stochastic nature of the μ-EDM process, the model incorporates voltage and capacitance to predict crater size on the workpiece caused by individual discharges in micro-EDM. The simulation involved using COMSOL Multiphysics 5.6 software to simulate a single discharge in the μ-EDM process. This simulation accounted for the phase change material properties and the expansion of the plasma channel radius over time. The study further developed a numerical analysis to assess how input parameters (capacitance and voltage) influence the efficiency of the plasma channel in removing molten material. A regression model for plasma flushing efficiency (PFE%) based on experimental and numerical results was introduced to predict the actual crater size. The findings indicate contrasting effects of capacitance and voltage on plasma flushing efficiency. Specifically, an increase in capacitance contributes to an increase in plasma flushing efficiency.

Acknowledgments

I would like to express my deepest gratitude to the following people who have helped and supported me throughout the completion of this thesis: First and foremost, I would like to thank my thesis supervisor Professor Asma Perveen, and co-supervisor Didier Talamona, for providing me with invaluable guidance, encouragement, and feedback throughout the research process. Their expertise, knowledge, and patience have been instrumental in shaping this thesis and helping me achieve my academic goals.

Secondly, I am very thankful for the funding from project “Multi scale powder mixed EDM induced Functional Surfaces on Biomedical alloys for enhanced mechanical, electrochemical corrosion, tribological and biological performances.”

Additionally, I would like to thank Professor Tri Pham, Professor Alexandr S. Arbuz, and other core facility members for their assistance. I also would like to thank Mr. Salman Kiani from the Physics dept. for helping me with SEM characterization during the initial stages of measurements.

Lastly, I would like to thank my family, friends, and colleagues who have supported me throughout my academic journey. Their words of encouragement, emotional support, and understanding have been a source of strength and motivation for me. Thank you all for your support and encouragement.

List of related publications

- Ali, S., Omarov, S., Utebayeva, A., Pham, T., Talamona, D., & Perveen, A. (2024). Micro-WEDM of Ti-29Nb-13Ta-4.6Zr Alloy for Antibacterial Properties: Experimental Investigation & Optimization.- *Submitted to Metals.*
- Ali, S., Talamona, D., & Perveen, A. (2024). Investigating Micro-EDM machinability of Ti-35Nb-7Zr-5Ta (TNZT) alloy.- *Submitted to Materials and Manufacturing Processes.*
- Ali, S., Talamona, D., & Perveen, A. (2024). Numerical modelling and simulation of micro Electro-discharge machining: prediction of crater size- *Accepted for presentation 2024 at the 15th International Conference on Mechanical and Intelligent Manufacturing Technologies (ICMIMT).*

Table of Contents

List of Acronyms

EDM	Electro discharge machining
μ-EDM	Micro electro discharge machining
PMEDM	Powder mixed Electro discharge machining
WEDM	Wire electro discharge machining
OC	Overcut
MRR	Material removal rate
TWR	Tool wear rate
SR	Surface roughness
EDX	Energy-Dispersive X-Ray Spectrograph

Table of Figures

List of tables

Chapter 1: Introduction

1.1 Background

Due to the rising need for micro-devices in mechanical, electronic, and medicinal applications, the necessity for miniaturization has increased across many production sectors. This led to the development of various micro-machining techniques, including cutting, laser, ion and electron beams, ultrasonic, electrochemical, and electrical discharge machining (EDM) [1]. EDM is notable for being unconventional and a non-contact thermal method, The EDM process involves the erosion of the material by the application of multiple sparks (due to potential difference) on the surface of workpiece material from the electrode, an illustration of the EDM process is shown in Figure 1.1.

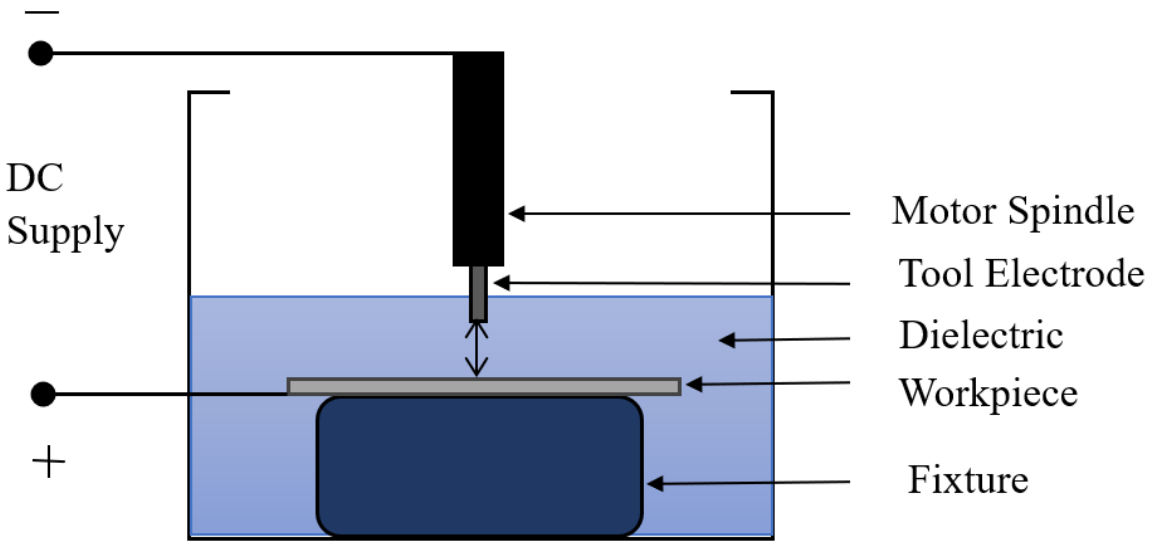

Figure 1.1: Schematic diagram of the EDM Process.

EDM offers specific benefits like high-precision machining, at macro and micro levels, of conductive materials irrespective of their hardness. Due to these advantages, micro-EDM has become a crucial method for micro-fabrication in the aerospace and medical sectors. It is praised for its outstanding performance in reaching a minimum machinable diameter of even 5 μm, which is related to its effectiveness in creating precise micro-metal holes [2,3]. Several researchers have delved into the world of μ-EDM and its complexities and analyzed that method of single-spark numerical modelling depicts very accurate crater size and temperature distribution [4-7].

Advancement in orthopaedics needs more precise machining that can be achieved using micro-EDM. Recently researched new materials for use in orthopaedic applications include titanium and its alloys. Titanium alloys perform better in biocompatibility than their predecessors

did [8]. The focus of the research, however, is currently on applying surface treatments that can improve their performance in the body. There are now some biocompatibility challenges that can be resolved by using the right surface treatment method on biomedical materials such as the mechanical characteristics and appropriate topography of implant surfaces. The very inert environment of the human body, along with constant and cyclic pressure on an implant by surrounding tissue, can cause damage to the surface of the implant, resulting in metal ions that could leak into the body or even result in implant failure. Additionally, proper topography promotes cell adhesion, which in turn promotes tissue ingrowth into materials [9].

1.2 Problem statement

Researchers in the fields of materials science and dental implants have been working for decades to develop & design better devices that may be used in clinical situations to replace injured body parts. The remarkable mechanical performance of titanium-based implants, which includes high bending, fatigue strength, and stiffness has attracted attention [10-12]. One of the most important requirements for effective orthopedic implants is that titanium and titanium alloys have mechanical properties that are closely matched to those of bone tissues [13].

Commercial pure titanium (CpTi) and Ti6Al4V implants are favored bioimplants [14], however, they still face some challenges such as their elastic modulus 100GPa and 120Gpa respectively [15], being substantially larger than bones (10-30GPa) [16, 17]. Additionally, the corrosion of Ti6Al4V could result in the cytotoxic effects of aluminum (Al) and vanadium (V) ions that could leach into the body [18], leading to severe reactions with neighboring tissues [19]. In response to the aforementioned issues, there is a need for biomedical alloys with similar mechanical properties without the presence of Al and V, the new generation of titanium alloys with non-toxic and allergy-free elements (Ta, Zr, Nb, and Mo) that are designed for orthopedic applications Table 1.1.

Table 1.1: New generation biomedical alloys.

Alloy name	Elastic modulus
Ti-29Nb-13Ta-4.6Zr	65GPa [20]
Ti-35Nb-7Zr-5Ta	55GPa [20]
Ti–12Mo–6Zr–2Fe	75GPa [20]

However, titanium and its alloys pose challenges in machining due to their inherent mechanical properties such as, low thermal conductivity hampers the dissipation of heat within the machining area, resulting in significant thermal gradients, leading to quick tool wear and or tool failure. Additionally, they have low elastic modulus, which is roughly half that of steel, resulting

in substantial workpiece deflections during machining with conventional ways [22]. As a result, non-traditional machining techniques like micro-electro discharge machining (μ-EDM) have become respectable substitutes. Micro-EDM is especially useful for cutting titanium alloys since there is no direct contact between the tool and the workpiece, so no cutting force.

1.3 Motivation

Traditional methods of machining titanium alloys pose challenges in machining, they have low elastic modulus, which is roughly half that of steel, resulting in substantial workpiece deflections during machining with conventional ways [22]. This investigation intends to explore non-traditional method, micro-scale EDM machining methods and efficient surface treatment methods for titanium alloys, to enhance their orthopedic implant effectiveness. The goal of this investigation is to examine the mechanical and biocompatible characteristics of Ti-35Nb-13Ta-Zr4.6 and Ti-29Nb-7Zr-5Ta, which can replace the super implant Ti-6Al-4V, as well as the effectiveness of various surface treatments and machining parameters.

This investigation aims to investigate the best surface treatment and machining process for the aforementioned alloys. Specifically, it compares the surface characteristics and biocompatibility among the treated and untreated surfaces. The results should help improve orthopedic implant design. This study may result in the development of a unique surface treatment method that strengthens the mechanical and biocompatible properties of titanium alloys, consequently increasing the long-term efficacy of orthopedic implants.

1.4 Research Aims and Objectives

The main objective of this investigation is to study and report the most effective micro electro-discharge machining parameters for improved surface modification. Enhancing the surface biocompatibility biomaterials by optimizing micro EDM process parameters (voltage and capacitance) of the titanium alloys (TNTZ). The project includes several particular objectives, including:

1. Optimization of μ-EDM parameters for the improved biocompatibility of Ti-29Nb-13Ta-Zr4.6 and Ti-35Nb-7Zr-5Ta.
    a. Investigating the MRR, Crater size, Kerf width, SR, and Anti-bacterial Adhesion for three levels of process parameters.
2. Optimization of micro-WEDM parameters for the improved biocompatibility of Ti-29Nb-13Ta-Zr4.6 and Ti-35Nb-7Zr-5Ta.
    a. Investigating the MRR, Crater size, Kerf width, SR, and Anti-bacterial Adhesion for three levels process parameters.

3. Numerical simulation of micro-drilling EDM to predict crater size.

The research aims to optimize the surface modification procedure for improving the biocompatibility of implant materials derived from TNTZ titanium alloy. This entails a thorough investigation of machining parameters, MRR, mechanical properties, which eventually results in a comprehensive evaluation of biocompatibility based on the gathered data.

Chapter 2: Literature Review

This chapter includes the survey of the relevant literature and provides an overview of earlier research to provide some context for fundamental concepts. Additionally, it contains several articles detailing the research and work proposed by other authors in the literature. Moreover, the convergence of biomedical titanium alloys and electro-discharge machining surface treatment are these two domains is also examined.

2.1 Biomedical materials

Biomaterials are artificial substances that interact with tissues in the body, and they might be made up of metallic alloys, polymers, ceramics, and natural materials. However, Ceramics and polymers lack low yield strength, moreover, they have tensile strengths that are substantially lower than those of metallic alloys [23]. While metallic alloys have a higher tensile strength, they also have several drawbacks, like, a relatively low overall strength and a tendency to corrode, wear, and have a different Young's modulus from bones.

There are several types of metallic alloys such as stainless steel is a cost-effective material with strong biocompatibility but has high modulus and low wear resistance. It is appropriate for transient biomedical devices like plates and screws. However, cobalt-based alloys provide greater fatigue strength together with enhanced wear and corrosion resistance, however, the disadvantages include a high modulus, high price, and possible biological toxicity [23].

Magnesium and its alloys, due to the biocompatibility, biodegradability, and low Young's modulus are well suited for usage in biodegradable orthopaedic devices such as bone pins and plates. However, struggles with poor corrosion resistance and hydrogen evolution when deteriorating [24].

The search for the ideal implant material that meets all biocompatibility requirements is still ongoing in the medical industry. Among these choices, titanium and its alloys have become the orthopaedic implant materials of preference. While compared to the other metallic implant materials, titanium stands out due to its remarkable combination of strength, Young's modulus, and biocompatibility [8]. Although Ti6Al4V has traditionally been regarded as a good option for implant applications, Table 1 presents some literature, which shows the effect of process variables on performance parameters. However, new research has revealed alarmingly high levels of vanadium (V) toxicity [25]. This challenge has led to a search for workable substitutes that can take the place of the traditional Ti6Al4V alloy.

One crucial factor that requires thorough consideration is the corrosion resistance of implant materials. This topic has attracted a lot of research attention owing to how important it is

for promising biocompatibility. This increased attention is due to the fact that the human body is a very active environment that is vulnerable to starting corrosive reactions in metals. Such reactions may have a negative effect on the life of the implant and perhaps prompt in implant failure. Additionally, the ion release brought on by insufficient corrosion resistance has the potential to result in grave consequences like cancer or hypersensitive reactions. When external stresses and wear are present, implant corrosion is more vulnerable [26].

When compared to more common materials like stainless steel and cobalt-chromium alloys, the distinctive ability of titanium alloys to quickly produce a protective titanium oxide layer stands out as a distinguishing benefit. It prevents corrosion by acting as a coating of oxide. The success and lifetime of implants are ultimately impacted by the corrosion resistance of implant materials, which can be further improved by increasing the endurance of the titanium oxide layer. Due to these issues the researchers [20, 21] in the field of material science has reported titanium alloys with non-toxic, corrosion resistant, allergy free elements such as, Tantalum (Ta), Zirconium (Zr), Niobium (Nb), and Molybdenum (Mo).

2.2 Micro-Electro-discharge machining (µ-EDM)

EDM is an advanced machining technology that offers several advantages over traditional procedures [1, 17, 27], the ability to produce difficult-to-process materials with remarkable accuracy and a higher level of surface quality. EDM is an efficient unconventional technique for manufacturing precise micro-components. EDM is a thermo-electric method that heats the workpiece material locally by repeatedly sparking in the spark gap. These sparks can raise the temperature of the workpiece to around 12,000°C [27]. The work surface melts and vaporizes due to the immense energy produced at such high temperatures. A constantly rotating dielectric medium effectively removes the molten debris from the cutting area. With little force applied between the workpiece and electrode, it enables contactless machining of electrically conductive hard, brittle, and ductile materials. When the correct parameters are used, it excels at high-quality and high-precision machining. Elongated electrodes can be used efficiently with micro-EDM, unlike other techniques like micro-milling, particularly with hard materials [28]. Table 2.1 displays the effect of EDM process (electrical) parameters on the machining of titanium alloys.

Table 2.1: Effect of process parameters on titanium-based alloys.

Author	Outcomes

Azad et al., [29]	• The author investigated the ramification of process variables (voltage, Current, and frequency) and optimized the effectiveness of performance parameters (MRR, TWR, OC, and surface integrity) of titanium alloy Ti6Al4V employing the Taguchi method.
Sagar et al., [30]	• Investigate the optimum performance parameters (MRR and side taper ratio) for micro-EDM drilling of Ti6Al4V with single and multi-objective optimization. • Analyse the ramification of the voltage, current, and time on side gap width, MRR, and taper ratio using Analysis of variance (ANOVA).
Kibria et al., [31]	• Author investigated the ramification of dielectric on the machining performance of Ti6Al4V. Mixing of boron carbide with deionized water enhances the machining performance.
Pradhan et al., [32]	• They established the mathematical model for MRR, TWR, OC, and Taper using regression analysis for the μ -EDM of Ti6Al4V as a function of current and pulse on time. • Higher the value of the current and pulse on time deteriorates the surface and also increases the width of the white layer.
Wang et al., [33]	• Find the relationship that surface roughness varies directly with the expansion in electrode size. • Surface roughness drops if deionized water is used as dielectric instead of the EDM oil because of the lower viscosity. • Reduction in discharge energy would decrease the number of surface defects, such as micro-voids and micro-cracks.

Like standard EDM, micro-EDM eliminate the material off the workpiece employing a series of electric spark discharges that recur quickly and happen across the tool electrode and the workpiece, in the presence of dielectric fluid, which is continuously flowing between them, Figure 2.1. depicts the experimental setup of micro-EDM. Interestingly, because of the minute amounts of material degraded during this machining process, which normally range from 0.05 to 500 μm^3, the energy consumption in the micro-EDM approach is comparatively low, typically ranging from 10^{-9} to 10^{-5} joules [4]. There are different types of μ-EDM, such as micro-EDM (μ-EDM), micro-wire EDM (μ-WEDM), and powder-mixed micro-EDM (μ-PMEDM), each with unique material removal rates and discharge energy values [28]. However, the build-up of these tiny particles of debris causes problems including uneven sparking and short-circuiting in the machining gap, Table 2.2. shows the green μ-EDM manufacturing. Several strategies, such as direct flushing, pressure-

based flushing, or suction-based flushing, have been put forth to remove the µ-scale debris from the machining zone in an effort to remove debris effectively.

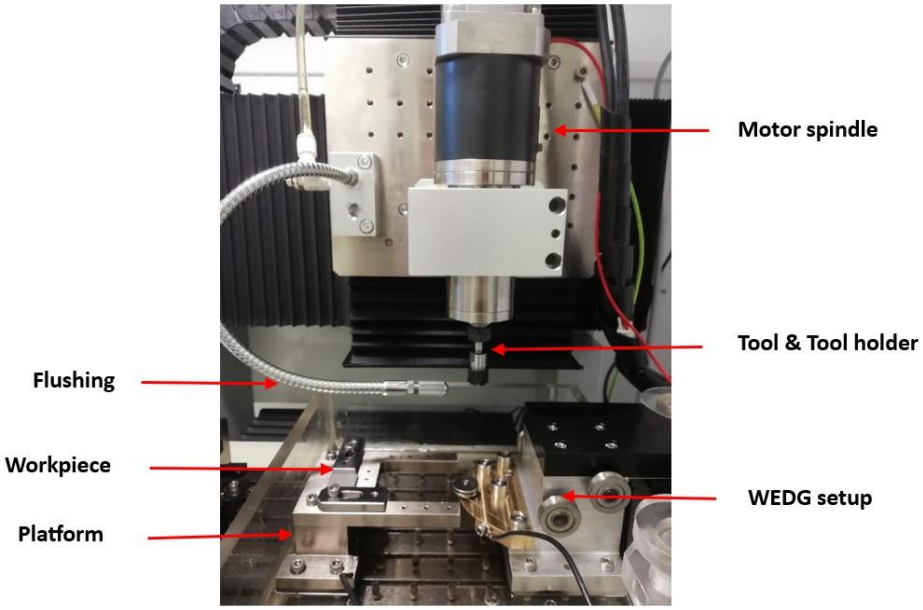

Figure 2.1: Experimental setup of µ-EDM

Table 2.2: µ-EDM green manufacturing.

Author	**Outcomes**
Yu et al., [34]	• The author reported that dry gases (low density), except for oxygen, as dielectric medium reduce the MRR due to the accumulation of debris that resists the spark intensity on the workpiece surface. • This reattachment of debris to the workpiece surface results in larger surface roughness.
Wang et al., [35]	• The author experimented dry EDM turning process on metal metal-bonded diamond wheel. The outcomes show that wear is minimal when compared to traditional machining.
Ramani et al., [36]	• Authors investigated the influence of helium and argon gas as dielectric fluid while drilling µ-holes with copper electrodes. • They analyzed that MRR increases with the escalation in the energy.

Eastwood et al., [37] described the current developments in the reverse micro-EDM (µ-EDM) technique, which produces a variety of microfeatures with a high density and high aspect

ratio on a metallic surface. Their research covered recent advancements in electrode materials, power supplies, and different flushing methods that are relevant to micro-EDM. In another investigation, Jeon et al., [38] described the several forms of external energy-assisted μ-machining methods, such as thermal, cryogenic, plasma, and laser assistance. To produce high aspect ratio m μ-rods or electrodes, Mujumdar et al., [39] reported the use of reverse μ-EDM, which involves reversing the polarity of electrodes. The study examined the relationship between response variables such as MRR, surface morphology, and the erosion rate of the tool electrode, and several process variables such as threshold voltage, capacitance, and feed. Table 2.3 displays the effect of process parameters on performance parameters for Ti-6Al-4V during μ-EDM.

Table 2.3: Summary of Micro-EDM of Titanium alloys.

Alloy	**parameters**	**Research findings**
Ti6Al4V [40]	**Process Parameters:** Ip, Ton, and V. **Output parameters:** MRR, TWR, taper, and OC.	• It is seen that Ip has more effect on MRR and TWR more rapidly, whereas the taper and OC decrease gradually. • However, with the increase in V, the MRR increases proportionately, whereas TWR decreases monotonously. • With an increase in Ton the MRR increases, whereas OC, and TWR decrease.
Ti6Al4V, SUS304, and SKH59 [41]	**Process Parameters:** C, Ton, and duty factor. **Output parameters:** Surface roughness.	• The surface morphology of the Ti-6Al-4V alloy machined by μ-EDM surpasses that of SUS304 and SKH59 because it has lower thermal conductivity. • Low discharge energy results in smaller craters, leading to a smooth surface and higher fractal dimension. However, both higher and lower gap voltage levels tend to produce more coarse surfaces with low fractal dimensions.
Ni-Ti SMA [42]	**Process Parameters:** C and V. **Output parameters:** OC, taper, and MRR.	• A high MRR is often achieved by using machining, but the poor quality of the micro-holes. Conversely, micro-holes produced by micro-EDM exhibit high quality with good surface morphology, albeit with a lower MRR.

		• During μ-EDM the MRR increases rapidly with an increase in energy, however, the OC and taperness increase proportionately.
Ti6Al4V [43]	**Process Parameters:** C, Ton, V, and tool rotation. **Output parameters:** OC and MRR.	• The author concluded that capacitance emerges as the most influential parameter for MRR, surpassing the effects of other variables such as pulse-on time, voltage, and tool rotation speed. In contrast, for the analysis of overcut (OC) the capacitance, voltage, and pulse-on time have significant effects. • However, tool rotation speed does not exhibit a significant effect on either MRR or OC.
Ti6Al4V [44]	**Process Parameters:** Ip, Ton, and Toff. **Output parameters:** OC, taper ratio, and TWR.	• Researchers investigated the machining of μ-holes in a 10mm thick workpiece, and they concluded that as the tool delves deeper into the work material, there is an observable trend towards smaller debris particle sizes, indicating a reduction in the MRR per spark discharge.
Ti6Al4V [45]	**Process Parameters:** V, Ton, and Toff. **Output parameters:** MRR, SR, and TWR.	• Sheng et al., conducted μ-EDM with powder employing three types of tool electrodes. They concluded that copper tungsten electrode has a larger MRR, however, the SR, TWR, and recast layers are thinner than by using brass and tungsten electrodes.

2.3 Micro-Wire-EDM (WEDM)

Wire Electro Discharge Machining (WEDM) is a renowned non-traditional material removal method that is particularly being exploited in the manufacturing of products with complex forms. It is a unique variation on the traditional EDM method, in which the sparking is started by a wire electrode continuously running between wire spools as depicted in Figure 2.2. WEDM is like EDM that can machine electrically conductive materials irrespective of their hardness [46].

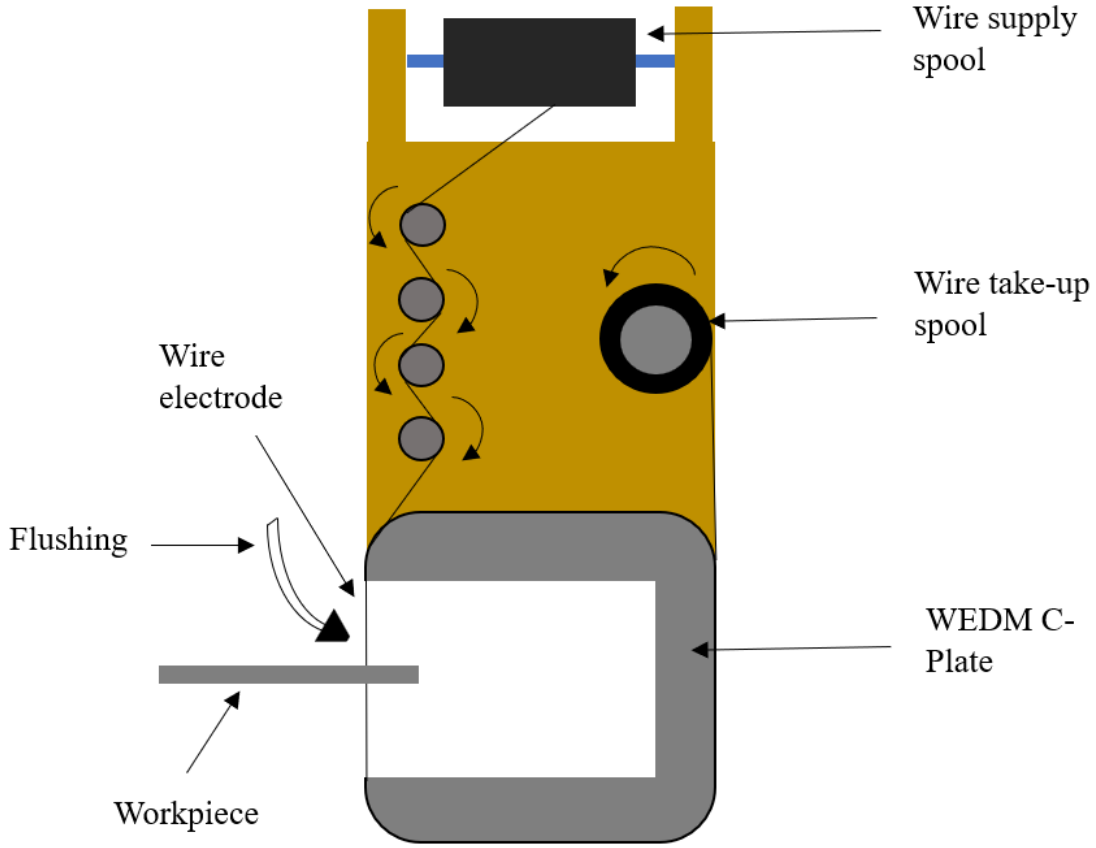

Figure 2.2: Schematic illustration of WEDM.

The Spark Theory used in WEDM corresponds closely with EDM. Multiple sparks can be seen while WEDM at the same moment since real discharges can happen more than 100,000 times per second for only a fraction of a second. The amount of material removed in this process depends on the specified process parameters, surface finish, and the intended cutting speed. The heat produced by each electrical spark can reach upto 15,000° to 21,000° ºF, which results in a small quantity of material melting and evaporating from both the workpiece and the wire. The resulting chips from the process can be removed by using top and bottom flushing nozzles to direct a stream of dielectric (EDM oil or de-ionized water) away from cutting zone, the flow of dielectric also prevents the accumulation of heat in the workpiece [47].

Numerous process parameters influence the WEDM while machining conductive materials with high quality. The electrical parameters that influence WEDM are peak current, supply voltage, polarity, pulse on time, and pulse off time, Table 2.4 represents the influence of process variables on WEDM effectiveness. Additionally, non-electrical variables such as wire speed, wire feed rate, and flushing rate are used to achieve better surface while WEDM. Furthermore, electrode-based factors such as wire diameter and composition are critical in defining the Wire EDM processed specimen surface characteristics.

Table 2.4: Influence of process parameters on the performance of WEDM.

Author	**Outcomes**
Manna & Bhattacharyya [48]	• The authors analyzed the best parameter settings for the machining of aluminum-reinforced silicon carbide metal matrix composite. • They developed analytical models employing the Gauss elimination approach for SR and MRR to explain the machining performance.
Singh & Garg [49]	• The study discussed how WEDM process parameters affect MRR. The results depicted that the material removal rate increases in direct proportion to increases in peak current and pulse on time. • In contrast, the MRR decreased as the pulse off time and servo voltage increased.
Arvind et al., [50]	• The authors employed the Taguchi experimental method to optimize the best machining parameters MRR and SR while WEDM of brass material. • The study found that the two main variables affecting MRR and surface finish were pulse-on time and feed rate. Notably, it was concluded that increasing feed rate and pulse-off duration increased MRR while concurrently lowering SR.
Anish Kumar et al., [51]	• The authors conducted Scanning Electron Microscopy (SEM) micrographs from the Metallographic Analysis of Pure Titanium (Grade-2) Surface using WEDM. The study concluded that the WEDM surface had a more irregular topography with a variety of defects, including globules of debris, spherical particles, craters of different sizes, and μ-cracks. • According to the investigation, the most important factors causing the surface texture to deteriorate, were peak current and pulse on time. • Furthermore, residuals of carbon, zinc, and copper were found in the machined samples by EDX analysis. This is explained by the brass wire electrode melting, evaporating, and then

	solidifying again. These elements are then transferred to the workpiece during the WEDM process.
Parashar et al., [52]	• The study examined the influence of WEDM parameters on kerf width in stainless steel machining. The results indicated that the two most significant elements impacting kerf width were pulse on time and dielectric cleansing pressure. • Furthermore, it was concluded that wire feed, gap voltage, and pulse off time had less of an impact on the kerf width during the machining process.

2.4 Finite Element Method (FEM) for simulating μ-EDM process

Several process parameters influence the Electro Discharge Machining (EDM) process. These include the type of dielectric fluid, flushing pressure, open voltage, electrode size, polarity of the electrode and workpiece, discharge current, and pulse on & off time. An aggregation of single pulse discharges occurs during the material removal process while continuous discharges. Nevertheless, obtaining the combined effects of several discharge occurrences by simply superimposing the individual discharge outcomes linearly is a difficult task. This challenge results from variations in the pressure and composition of the dielectric in the gap across time and space, including the makeup of solid particles and bubbles. As such, it turns out to be a difficult undertaking to simulate the EDM process [53].

The material removal theory is based on the electro-thermal mechanism, in which the intense current passing through the plasma channel causes extremely high temperatures, which in turn causes material removal at the electrode and workpiece surface. Snoeys and Van Dijck [54] established an electro-thermal model using a semi-infinite cylinder with circular heat input, the power at each electrode from the energy input was supposed to be divided evenly in their model. Subsequently, Van Dijck and Dutre [55] expanded this work by using a two-dimensional heat flow model in which the medium is radially confined by an adiabatic cylindrical surface. In their model, they took into account two scenarios: one for the finite z direction and another for the infinite z direction. However, using the experimental parameters in this model [56], the Material Removal Rate (MRR) at a voltage of 25 V and a current of 12.8 A was determined to be 4.461 mm^3/min. This value exceeds the relevant experimental results by about 8.83 times.

An alternative method using a semi-infinite cylinder with a disc-shaped heat source was presented by Pandey and Jilani [57]. In this concept, it was assumed that the surfaces beyond the disc heat source zone remained insulated. The temperature distribution within the material was

defined as dimensionless variables under the assumptions of constant thermal characteristics and constant heat flux. Furthermore, erosion was postulated to occur in the melting zone at the electrode. Dibitonto et al. [56] employed a single-point heat source for the cathode eroding and a circular heat source for the anode. Through the use of experimental data, these models were verified and shown to provide a better estimation of the removal of material, especially for extended discharges and large current inputs.

Notwithstanding of the models listed above, they cannot be directly used for μ-EDM due to the significant distinctions between it and standard EDM. When it comes to μ-EDM, models usually overshoot the temperature distribution because the pulse-on-time and discharge energy are usually less than 5μs and 500W, respectively. Consequently, this overestimation results in inaccurate material removal estimations. As reported by Dibitonto et al. [56], the cathode erosion model at voltage input of 25 V, current input of 2.34 A, and pulse-on-time of 5.6 μs yielded a theoretical Material Removal Rate (MRR) a much higher value of 13.82 mm^3/min, however, the practical MRR was found to be 0.3 mm^3/min, resulting in a fraction of 46.07. As such, the accuracy and applicability of analytical models designed for micro-EDM remain constrained.

A numerical model was presented by Ben Salah et al. [58] to examine the temperature distribution during the Electrical Discharge Machining (EDM). They predicted the rate of material removal as well as the total surface roughness using the thermal results obtained from this model. Notably, their analysis took into account the fact that 0.08 (8%) of the heat produced reached the workpiece. It was emphasized numerical accuracy was greatly improved by the consideration of the temperature dependency of conductivity they concluded that the results were more in line with experimental findings. In another study, Kansal et al. [59] presented a model for powder-mixed electrical discharge machining to simulate the temperature distribution within the workpiece material. According to their model, the workpiece absorbed 9% of the total heat. Additionally, they calculated the MRR utilizing the results of the finite element simulation. Moreover, they reported that the accuracy is significantly increased for predicting MRR due to the inclusion of temperature-dependent material properties.

Chapter 3: Material and Methods

3.1 Materials

The workpieces undergoing processing are TNTZ alloys Ti-35Nb-7Zr-5Ta and Ti-29Nb-13Ta-4.6Zr, however, for thermal simulations Ti-6Al-4V was employed. These alloys have low density and remarkable resistance to corrosion making them preferred over implant biomaterials currently in use. As such, it has attracted a great deal of attention in orthopedic applications. Additionally, the chosen alloys as the study material after a thorough evaluation of all available possibilities, mainly because of their lower elastic modulus [20,60,61]. Moreover, these alloys have not yet been explored employing the EDM process. Table 3.1 displays the chemical composition of these alloys, and Table 3.2 displays the EDS analysis of the aforementioned alloys. The tool material was tungsten carbide (WC), EDS analysis of tool material is displayed in Table 3.3. The tool electrode for micro-EDM was a 300 µm-diameter tungsten carbide which is further reduced to 182um. Tungsten wire 50 µm diameter is used in WEDM experiments.

Table 3.1: Chemical composition of Titanium alloys.

Alloy	Elements (wt%)					
	Ti	Nb	Ta	Zr	Al	V
Ti-35Nb-7Zr-5Ta	53	35	5	7	-	-
Ti-29Nb-13Ta-4.6Zr	53.4	29	13	4.6	-	-
Ti-6Al-4V	90	-	-	-	6	4

Table 3.2: EDS analysis of the untreated surface of Titanium alloys.

Alloy	SEM image	Element	Line	Mass%	Atom%
Ti-35Nb-7Zr-5Ta	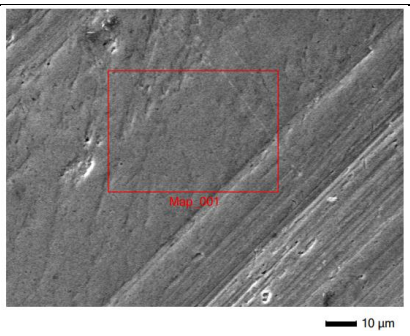	C	K	6.17±0.02	21.39±0.08
		O	K	9.06±0.06	23.59±0.15
		Ti	K	42.84±0.06	37.25±0.05
		Zr	L	6.04±0.04	2.76±0.02
		Nb	L	30.98±0.06	13.89±0.03
		Ta	M	4.91±0.04	1.13±0.01
Ti-29Nb-13Ta-4.6Zr		C	K	6.32±0.02	22.44±0.08
		O	K	8.97±0.05	23.92±0.14
		Ti	K	43.67±0.05	37.10±0.05
		Zr	L	3.78±0.04	1.77±0.02
		Nb	L	24.74±0.06	11.36±0.03

	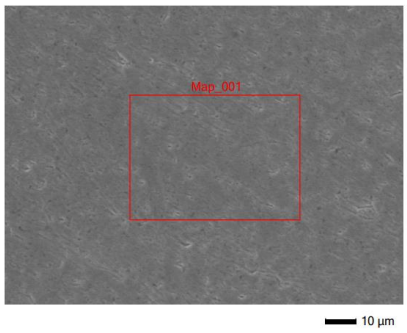	Ta	M	12.52±0.05	3.42±0.01
Ti-6Al-4V	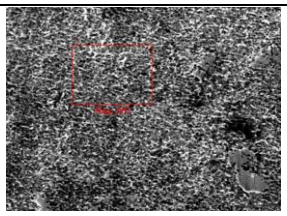	O	K	6.08±0.1	15.67±0.26
		Al	K	5.45±0.03	8.34±0.05
		Ti	K	84.74±0.12	72.97±0.03
		V	K	3.73±0.04	3.02±0.03

Table 3.3: EDS analysis of tungsten electrode.

Material	SEM image	Element	Line	Mass%	Atom%
Tungsten carbide (WC)	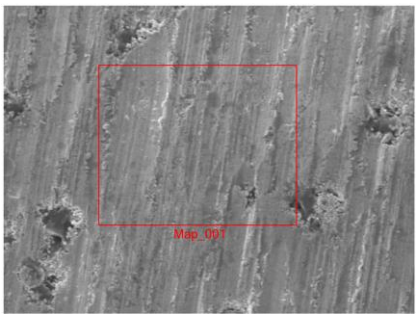	C	K	18.06	69.13
		O	K	2.77	7.95
		K	K	0.1	0.11
		Cr	K	0.17	0.15
		Co	K	5.52	4.31
		W	M	73.38	18.35

3.2 Performance parameters

3.2.1 Material removal rate (MRR)

The average volume of material removed [62] during the machining period is computed using the subsequent formula and is commonly expressed in cubic microns per minute.

$$MRR = \frac{V_a}{t} \tag{3.1}$$

This formula uses "V_a" to indicate the average hole volume in cubic micrometers and "t" to indicate the machining time in minutes.

$$V_a = \frac{\pi D_a^2 * h}{4} \tag{3.2}$$

Where “Da” and “h” represent the average diameter and depth of the hole respectively.

3.2.2 Overcut (OC)

In the realm of micro-EDM, overcut refers to the discrepancy between the diameter of the hole resulting from the machining procedure and the tool diameter as illustrated in Figure 3.1. In particular, the diametral overcut is determined by taking the difference between the entry diameter of the hole and the diameter of the micro-tool. This computation can be written as follows [62]:

$$OC = \frac{D_{hole} - D_{tool}}{2} \tag{3.3}$$

Where D_{hole} and D_{tool} represent the diameter of the hole and tool respectively.

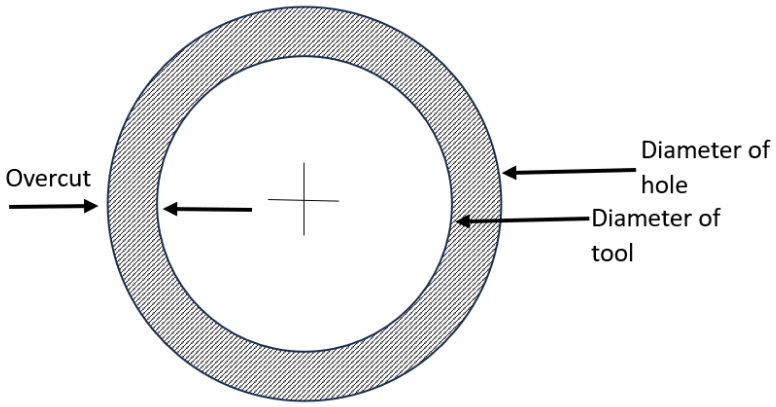

Figure 3.1: The schematic representation of overcut.

3.2.3 Circularity

The degree to which the shape of an object resembles an ideal circle is measured using a concept called circularity. It measures how far an object deviates from a true circle in terms of shape as shown in Figure 3.2. Circularity is seen as a "higher-the-better", when it gets close to 1, it means that the form of the object is almost exactly a perfect circle. On the other hand, when the circularity value is zero, it means that the shape of the item is becoming more and more like an extended polygon [63]. Circularity can be represented numerically as follows:

$$Circularity = \frac{4 * \pi * Area}{Perimeter^2} \tag{3.4}$$

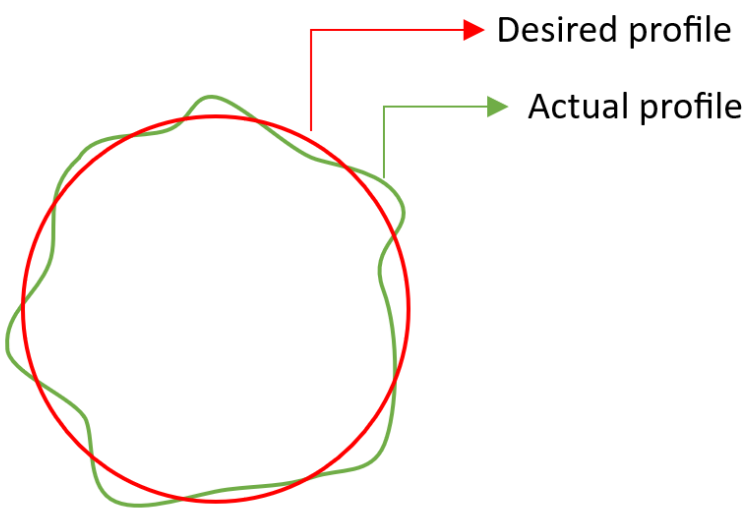

Figure 3.2: Schematic of circularity.

3.2.4 Crater size, microhardness, and surface roughness

The average diameters of three craters were determined from scanning electron microscope (SEM JEOL JSM-IT200(LA)) images. The accuracy of the study was improved by this method, which made it possible to measure the size of the crater precisely. A Vickers microhardness tester was used to measure the surface microhardness in this investigation. A 200-gram force indenter load and a 12-second dwell period were used for the experiments. For every experiment, three microhardness measurements were made to ensure precision and consistency. Moreover, for the 3D mapping and average surface roughness of the machined area, the Atomic Force Microscope (AFM) SmartSPM 1000 is used. The resolution and scan area for the surface profiling were 256px256p and 60µmx60µm respectively.

3.2.5 Kerf width

In essence, kerf width is the amount of material that the wire removes throughout the wire-EDM process. It is the measure of cut that the wire electrode makes in the workpiece as it passes through it as shown in Figure 3.3.

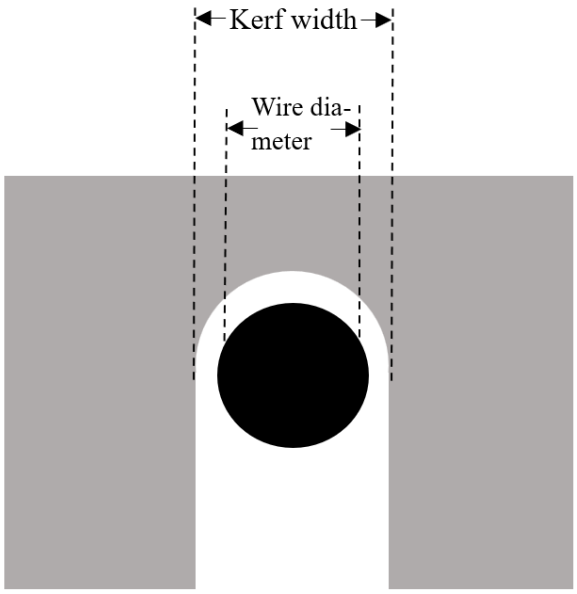

Figure 3.3: Schematic of wire diameter.

3.2.6 Antibacterial Tests

The goal of the test was to evaluate Wire Electrical Discharge Machining's (WEDM) antibacterial efficacy against multiple strains of bacteria, such as Escherichia coli (DH5α), Bacillus subtilis, Pseudomonas aeruginosa, and Staphylococcus aureus. This was accomplished by assessing the biofilm growth on various metal surfaces following a 72-hour broth culture inoculation. Fresh 24-hour liquid cultures of every species of bacteria were used to prepare the bacterial inoculum, aiming for an initial optical density (OD 600) of 0.1 or a McFarland turbidity of 0.5. A microplate reader was used to measure the OD 600 of the 16-hour culture broth in order to calculate the precise amount of bacteria that needed to be provided to fresh media in a 50 mL Falcon tube, leading to a final volume of 50 mL with an OD of 0.1. Every single specimen of the metal alloy was suspended in a different 50 mL Falcon tube that held a single species of bacteria in the culture medium. After that, these tubes were incubated for 72 hours in an aerobic environment at 37°C and 220 RPM in a shaker incubator.

The formation of biofilms and bacterial cells were then observed on the metal surfaces by staining them with crystal violet (CV) dye for a duration of thirty minutes. Following staining, the specimens were allowed to air dry for an hour at room temperature prior being imaged. They were then rinsed three times using distilled water. Employing a Zeiss AxioZoom V16 macroscope, bright-field and red fluorescent photos were taken with exposure periods of 20 ms and 800 ms, respectively. Using specially created MATLAB programs, a comparative study of the biofilm coverage was carried out. For the purpose of comparison, only biofilms larger than five times the surface area of a single bacterium and with a signal intensity of in excess of 250 were gathered.

The metals were first submerged in a 30% acetic acid solution for 15 minutes to eliminate any biofilms on the machined surfaces, ensuring the cleanliness and disinfection of the metals prior to the next investigations. Following a 30-minute immersion in a 70% ethanol solution, they were rinsed with distilled water and subjected to a 5-minute plasma cleaning process. To guarantee thorough disinfection before to culture them with bacteria, all metals were exposed to UV light for thirty minutes prior to each biofilm development test. With the exception of Staphylococcus aureus, which was cultivated in tryptone soy broth (TSB), all bacterial strains were cultured in Luria-Bertani (LB) broth. To avoid cross-contamination, all studies were carried out in an aseptic environment.

3.3 Micro EDM

A micro-EDM machine DTi110 RC-type (resistor-capacitor) based pulse generator was used in this investigation. The objective of the experimentation was to use micro-EDM to optimize the titanium alloy machining parameters based on discharge energy. The effect of the capacitance (C) and voltage (V) on the power of micro-discharge EDM is expressed by the following formula [50]:

$$E = \frac{1}{2}CV^2 \tag{3.5}$$

Three levels were identified for both the voltage and capacitance settings 80-130(V) and 10-400(nF) respectively, Table 3.4 represents the complete L9 experimental designs with two factors for micro-EDM.

The goal of each experimental session was to drill a depth of 0.050 mm (50 μm) at a feed rate of 0.09 mm/min. This systematic experimentation demonstrates an effort to systematically evaluate and determine the optimal parameters for the micro-EDM process on titanium alloy by experimenting with different amounts of capacitance and voltage while keeping constant feed rates and depth.

Table 3.4: Experimental design for μ-EDM.

Capacitance (nF)	Voltage (V)
10	80
	105
	130
100	80
	105
	130

400	80
	105
	130

3.4 Micro WEDM

A μ-WEDM machine DTi110 RC-type (resistor-capacitor) based pulse generator was used in this investigation. The objective of the experimentation was to optimize the titanium alloy machining parameters based on capacitance and voltage. The effect of the capacitance (C) and voltage (V) on the power of micro-discharge EDM is expressed by using equation 3.5 [50].

Three levels were identified for both the voltage and capacitance settings 80-130(V) and 1-100(nF) respectively, Table 3.5 represents the complete L9 experimental designs with two factors for micro-WEDM. The capacitance levels were selected after the feasibility test. According to the feasibility test, the wire was kept on breaking at 400nF. The goal of each experimental session was to make a slot of 0.050 mm (50 μm) at a feed rate of 0.09 mm/min. This systematic experimentation demonstrates an effort to systematically evaluate and determine the optimal parameters for the micro-EDM process on titanium alloy by experimenting with different amounts of capacitance and voltage while keeping constant feed rates and depth.

Table 3.5: Experimental design for μ-WEDM.

Capacitance (nF)	Voltage (V)
1	80
	105
	130
10	80
	105
	130
100	80
	105
	130

3.5 Numerical simulation for predicting crater size

Titanium alloy (Ti-6Al-4V) was used as the workpiece material, while the tool material was tungsten carbide. The thermal properties of Ti-6Al-4V are displayed in Table 3.6. A DT-110i Mikrotools EDM machine was used for the experiments. A total of 24 experiments were performed and the dielectric fluid used during experiments was Hydrocarbon oil in which both the electrode

and the workpiece were immersed. For the experimentation, three levels of capacitance and eight levels of voltage configurations were used. Details of the experiments are listed in the Table 3.7.

Table 3.6: Thermal properties of Ti-6Al-4V.

Property	**Magnitude**
Thermal conductivity under solid/liquid	6.3/30 W/(m*K) [65]
Density under solid/liquid	4500/4200 kg/m^3 [66]
Specific heat capacity under solid/liquid	620/895.2 [66]
Melting temperature	1928 K [66]

Table 3.7: Experimental conditions.

Capacitance (nF)	1,10,100
Voltage (V)	80,85,90,95,100,105,110,115
Spindle speed (rpm)	1000
Feed rate (mm/min)	0.09
Polarity	Workpiece positive
Tool material	Tungsten carbide, Dia=750μm
Workpiece material	Ti-6Al-4V

3.5.1 Micro-EDM FEM model

Figure 3.4 outlines the methodology utilized for single-spark numerical simulation. It initially depicts the assumptions and input parameters. The corresponding Gaussian heat flux was solved to determine the crater size. During the EDM process at the beginning of discharge, the breakdown between the anode and cathode is followed by the development of the plasma channel. This channel receives an exceptionally high current that raises the temperature of both electrodes noticeably. After each discharge cycle, material that has melted or evaporated is released into the dielectric, leaving a crater behind. A similar effect is assumed to occur in μ-EDM, however, with a higher energy density in a much smaller gap and for a significantly shorter duration.

Generally, the development of a μ-EDM thermal model is predicated on certain assumptions:

- The 2D-Axissymmetric model is developed for a single spark.
- The pulse energy is solely influenced by the capacitance and voltage.
- Workpiece material can be modeled as phase change material.
- During the discharge process, the pulse energy distribution remains the same.
- Heat transfer from the tool to the workpiece only through conduction.
- Heat loss from radiation and material removal can be neglected.
- Workpiece material is homogeneous and isotropic.

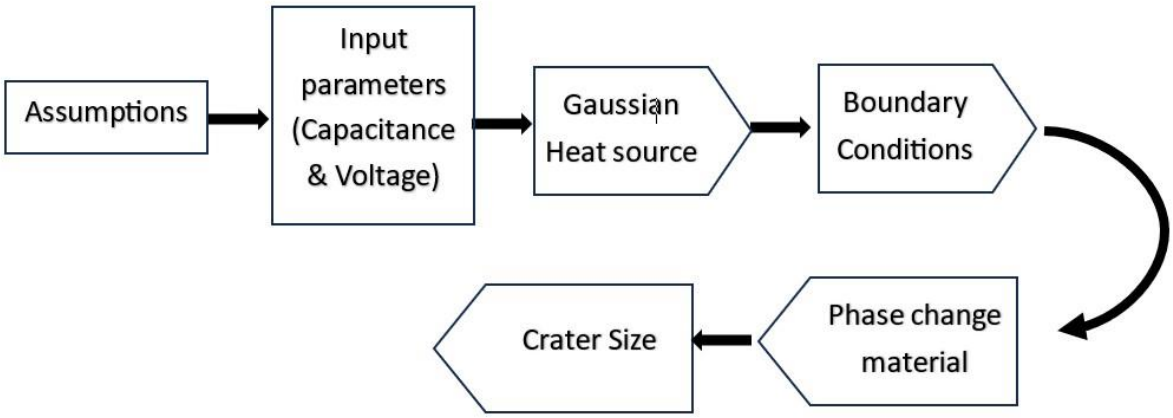

Figure 3.4: Flow chart for simulating crater size in single spark µ-EDM

The basic equation for thermal modeling describes the distribution of heat during each discharge excluding internal heat generation [67]. This differential equation, which deals with heat transfer, is expressed as:

$$\frac{1}{r}\frac{\partial}{\partial r}\left(r\frac{\partial T}{\partial r}\right)+\frac{\partial^2 T}{\partial z^2}=\frac{1}{\alpha}\frac{\partial T}{\partial t} \tag{3.6}$$

In this case, α denotes thermal diffusivity which can be defined as the fraction for the density and specific heat to the thermal conductivity, of the material. T indicates temperature, and t indicates time. In addition, the coordinate axes and boundary conditions are indicated in Figure 3.4.

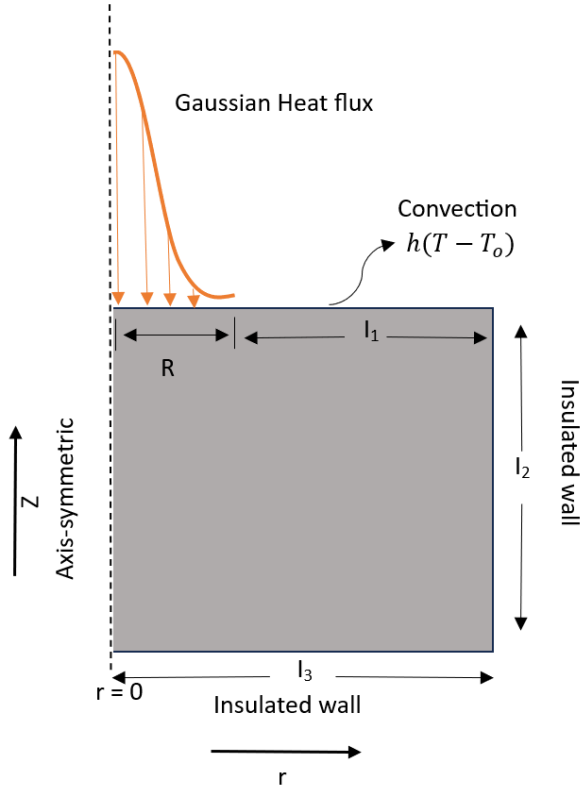

Figure 3.5: Boundary conditions for the FEM model.

Boundary conditions (BC) can be expressed as:

$$I_1 : k\frac{\partial T}{\partial z} = \begin{cases} h_c(T - T_o) & r > R \\ q(r) & r \leq R \end{cases} \tag{3.7}$$

$$I_2 = I_3 : \frac{\partial T}{\partial n} = 0 \tag{3.8}$$

Pulse heat from tool to workpiece is considered to be Gaussian distribution in spark radius [67], the equation can be expressed as:

$$q(r) = q_o exp\left(-4.5\left(\frac{r}{R}\right)^2\right) \tag{3.9}$$

Where R represents the plasma radius [68] and its equation can be expressed as,

$$R = 0.0284 * {t_d}^{0.9115} \tag{3.10}$$

Where t_d is the discharge pulse duration. Additionally, q_o in equation (3.9) represents the maximum heat flux [69], equation for maximum heat flux can be expressed as:

$$q_o = 4.5\left(\frac{E}{t_d * \pi * R^2}\right) \tag{3.11}$$

3.5.2 Thermal modeling of the crater

The numerical analysis conducted in this study incorporated Gaussian distributed heat flux during a single spark of the EDM process. The crater after a single pulse was simulated by using the COMSOL Multiphysics 5.6 software. This software is noted for its capability to consider phase change material properties, thus enhancing the accuracy of simulations by aligning them more closely with experimental observations. Crucial aspects such as the latent heat of melting in the worlpiece were integrated into the numerical analysis, significantly affecting the results. The thermal model “Heat transfer in solids incorporating the phase change material” based on transient thermal analysis was performed to determine the crater size in the workpiece. The size of the thermal analysis domain was contingent upon the EDM process parameters, specifically the plasma channel radius calculated from the machining settings (Eq. (3.8))

Chapter 4: Results and discussion

4.1 Micro EDM of Ti-35Nb-7Zr-5Ta

4.1.1 Analysis of MRR

Figure 4.1 depicts the changes in Material Removal Rate (MRR) with variations in capacitance (C) ranges from 10 to 400 nF, where each curve on the plot represents a different voltage level (80, 105, and 130V). The observation from Figure 8 demonstrates that the MRR displays a rapid increase when the capacitance increases from 10 to 100 nF. However, the skewness of MRR begins to decrease when the capacitance increases from 100 to 400 nF. This gradual increase is due to the considerably high energy level in this phase, which raises the temperature between the workpiece and the tool. This rapid increase in temperature breaks the hydrocarbon in flushing oil and forms a layer of carbon debris on the workpiece surface. This layer of carbon debris accumulates on the surface of the workpiece, preventing smooth machining in addition to limiting the effective and steady electrical sparks. Consequently, the MRR increases marginally. The finding emphasizes the intricate relationship between the process parameters and MRR on the effectiveness of the EDM process, as well as the potential consequences of high temperatures and energy on machining efficiency.

With an increase in capacitance from 10 to 100nF at voltage levels of 80V, 105V, and 130V the MRR increases 6.38, 4.45, and 3.773 times respectively. Similarly, with the increase in the capacitance from 100nF to 400nF at voltage levels of 80V, 105V, and 130V the MRR increases 1.74, 1.042, and 1.256 times respectively. However, with an increase of voltage from 80V to 105V at capacitance levels of 10nF, 100nF, and 400nF the MRR increases upto 2.06, 1.497, and 2.167

times respectively. Moreover, with an increase of voltage from 105V to 130V at capacitance levels of 10nF, 100nF, and 400nF the MRR increases upto 1.29, 1.095, and 1.32 times respectively.

At a standard significance level of 0.05, the intercept, the coefficient for predictor x1 (capacitance), and x12 demonstrate statistical significance, the p-values for intercept and x1 are 0.00040942 and 0.002733, 0.0036934, and 0.019132 respectively. However, the coefficients for x2 (voltage), the interaction terms x1:x2 and $x2^2$ do not exhibit statistical significance as displayed in Table A.1. The R-squared value for the model is 0.965 suggesting that approximately 96.5% of the variability observed in the MRR can be accounted for by the capacitance and voltage.

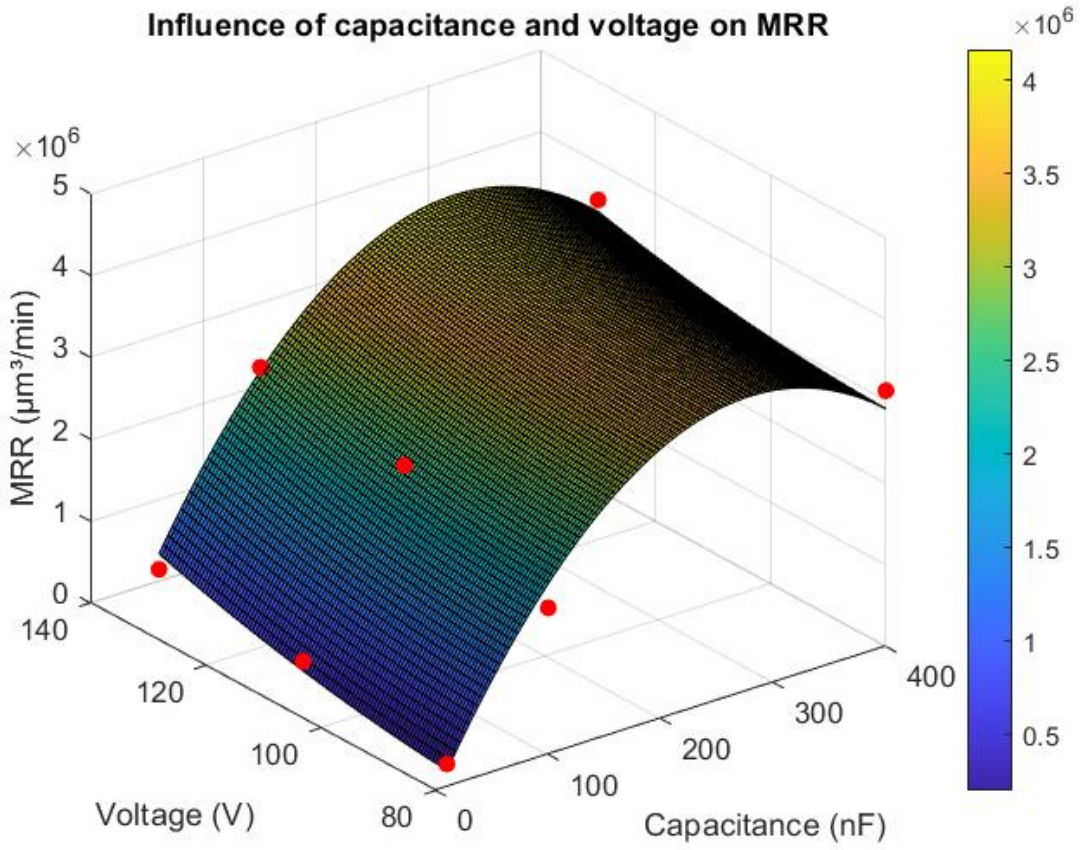

Figure 4.1: Influence of capacitance and voltage variation on Material Removal Rate for µ-EDM of Ti-35Nb-7Zr-5Ta.

4.1.2 Analysis of overcut

Figure 4.2 depicts the Overcut (OC) as it varies with the capacitance ranging from 10 to 400 nF while keeping the spindle speed constant at 1000 rpm, and positive workpiece polarity. The figure shows that OC exhibits a gradual and monotonically increasing trend as capacitance increases. Lower discharge energy levels cause smaller craters to form, which in turn causes less overcut because there is less material removed in each discharge. On the other hand, overcut tends

to rise with larger discharge energy levels. This can also be explained by the greater span of discharge columns, which last longer than those at low energy levels. However, after 100nF, OC is found to increase marginally may be due to the accumulation of debris at the tool and workpiece surface at high energy levels [62].

As capacitance escalates from 10 to 100nF across voltage thresholds of 80V, 105V, and 130V, the overcut of µ-holes amplifies by factors of 1.523, 1.464, and 1.646 respectively. Similarly, with the increase in the capacitance from 100nF to 400nF at voltage levels of 80V, 105V, and 130V the overcut of µ-holes increases by 1.145, 1.184, and 1.121 times respectively. However, with an increase of voltage from 80V to 105V at capacitance levels of 10nF, 100nF, and 400nF the overcut of µ-holes upto 1.127, 1.083, and 1.12 times respectively. Moreover, with an increase of voltage from 105V to 130V at capacitance levels of 10nF, 100nF, and 400nF the overcut of µ-holes increases upto 1.027, 1.155, and 1.094 times respectively.

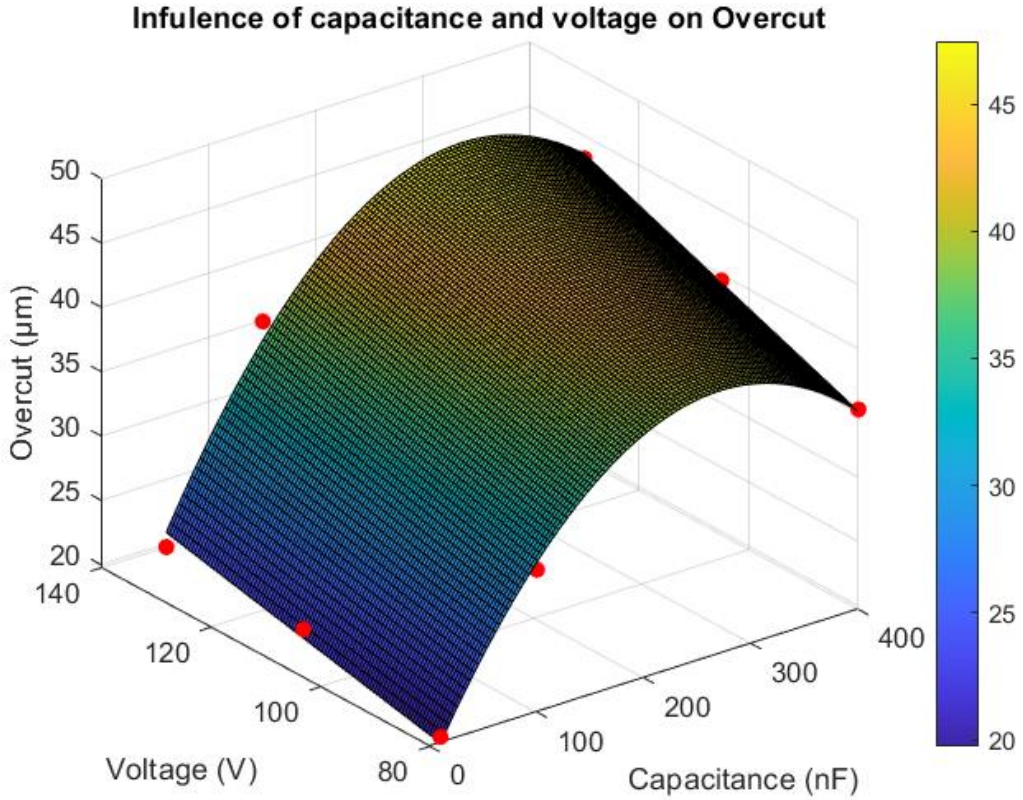

Figure 4.2: Influence of Capacitance and voltage variation on overcut during µ-EDM of Ti-35Nb-7Zr-5Ta.

It is evident that the intercept and the coefficient at a standard significance level of 0.05 pertaining to predictor x1 (capacitance), the coefficient for predictor x2 (voltage), and x12 demonstrate statistical significance, the p-values for intercept and x1 are 7.1594e-05, 0.00064424, 0.010538, and 0.019132 respectively. In contrast, the coefficients linked to x1:x2, x12, and x2 do not exhibit the requisite criteria for statistical significance, as elucidated in Table A.2. The R-

squared value of the model is computed to be 0.99, indicating that approximately 99% of the variance observed in the overcut can be ascribed to the interplay between capacitance and voltage.

4.1.3 Analysis of crater size

In an RC-type pulse generator, the material removal process is greatly influenced by the discharge energy per pulse, as it has a direct relation with capacitance and voltage [70]. Figure 4.3 depicts the surface topography at different capacitances and voltages, with constant electrode rotating speed. The results show that a higher capacitance causes bigger craters and a rougher surface finish at different levels of voltage. At the smallest capacitance (10nF) and voltage (80 V) as seen in Figure 4.3(A), the surface finish is finer, and it gets rougher as shown in Figure 4.3(B and C). This is because the lowest capacitance and voltage results in the lowest discharge energy. Figure 4.3(C, D, and F), illustrates that when the energy levels are high, there is a significant formation of larger craters that also exhibit more overlapping. The presence of larger-sized craters and craters overlapping typically indicates a rough surface texture.

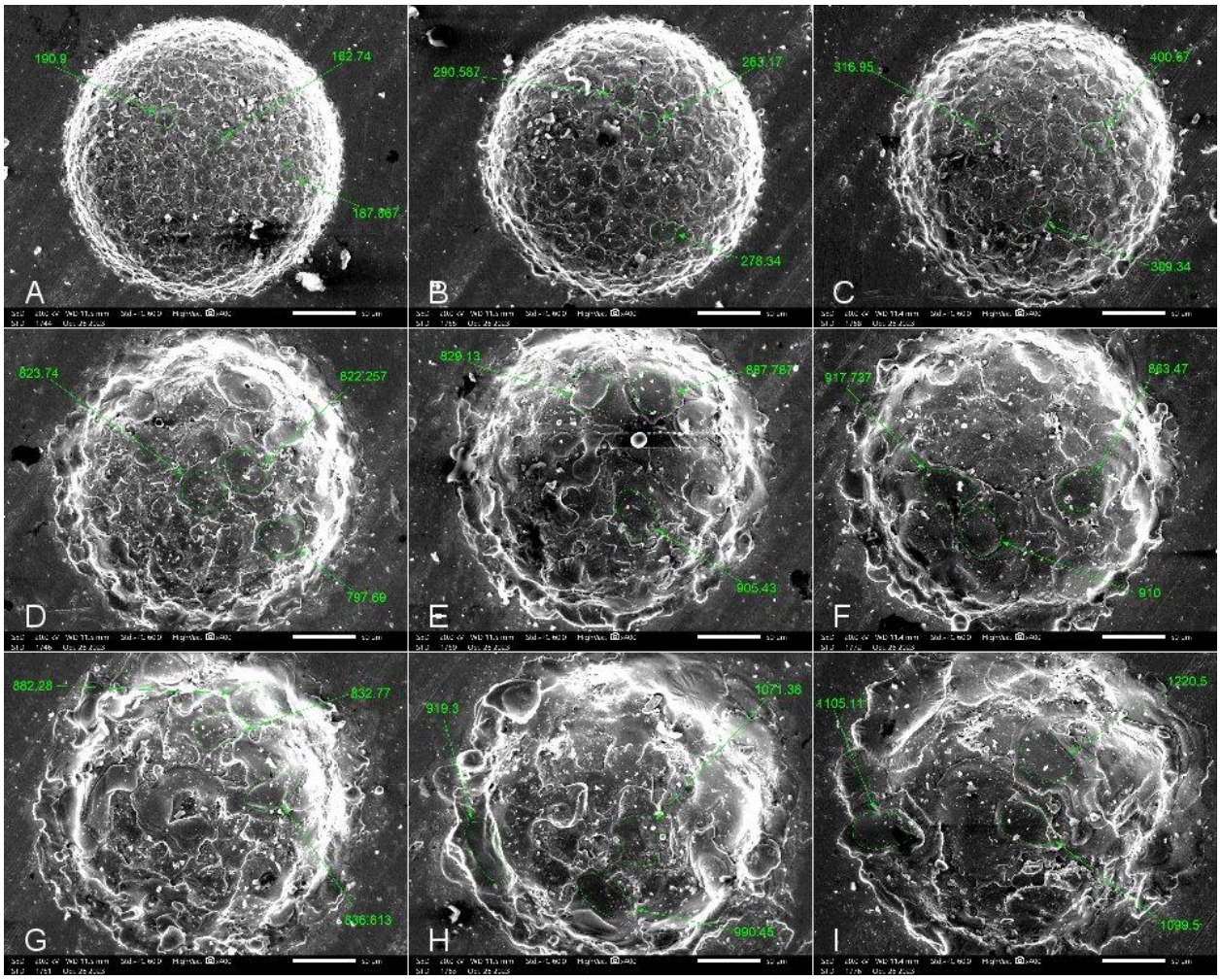

Figure 4.3: Effect of capacitance and voltage on crater size for µ-EDM of Ti-35Nb-7Zr-5Ta; (A) C=10nF & V=80V, (B) C=10nF & V=105V, (C) C=10nF & V=130V, (D) C=100nF & V=80V, (E) C=100nF & V=105V, (F) C=100nF & V=130V, (G) C=400nF & V=80V, (H) C=400nF & V=105V, (I) C=400nF & V=130V.

Figure 4.4 depicts the plot of the average crater area with changes in process parameters (capacitance and voltage), the average crater size is determined using ImageJ 1.54d software. The plot depicts that the average crater size tends to rise as discharge energy per pulse increases. This phenomenon happens due to a discharge column that is comparably broader at higher energy levels [62, 63]. Higher energy tends to generate large-sized craters, so increases the crater overlapping, surface roughness, and MRR.

Increasing capacitance from 10 to 100nF while maintaining voltage at 80V, 105V, and 130V results in an augmentation of the crater size by factors of 3.496, 3.152, and 2.83 times respectively. Similarly, with the increase in the capacitance from 100nF to 400nF at voltage levels of 80V, 105V, and 130V the crater size increases by 1.044, 1.136, and 1.181 times respectively. However, with an increase of voltage from 80V to 105V at capacitance levels of 10nF, 100nF, and 400nF the crater size increases upto 1.53, 1.04, and 1.168 times respectively. Moreover, with an increase of voltage from 105V to 130V at capacitance levels of 10nF, 100nF, and 400nF the crater size increases upto 1.234, 1.106, and 1.223 times respectively.

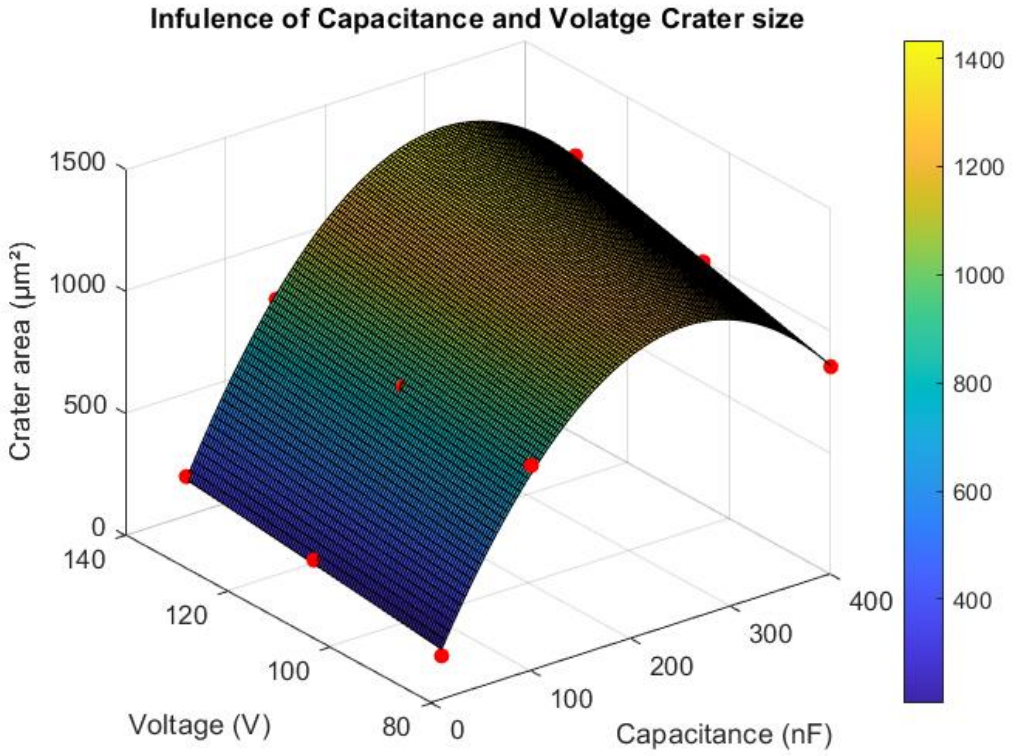

Figure 4.4: Influence of Capacitance and voltage variation on crater size for µ-EDM of Ti-35Nb-7Zr-5Ta.

It is discerned that employing a standard significance level of 0.05, the intercept and the coefficient associated with predictor x1 (capacitance), x2 (voltage), alongside x12, evince statistical significance. The p-values for the intercept and x1 are notably diminutive, at 3.2374e-05, 7.4492e-05, 0.0048521, and 0.00026818, respectively. Conversely, the coefficients for x22 and

the interaction terms x1:x2 do not exhibit statistical significance, as delineated in Table A.3. The R-squared value is computed at 0.997, signifying that approximately 99.7% of the variance observed in the crater size can be explicated by the interplay between capacitance and voltage.

4.1.4 Analysis of circularity

Figure 4.5 displays the results of the measurement of the circularity of the micro-holes drilled on Ti-35Nb-7Zr-5Ta using ImageJ version 1.45d software. This figure shows how circularity varies with capacitance horizontally keeping the voltage constant and varies with voltage vertically keeping the capacitance constant.

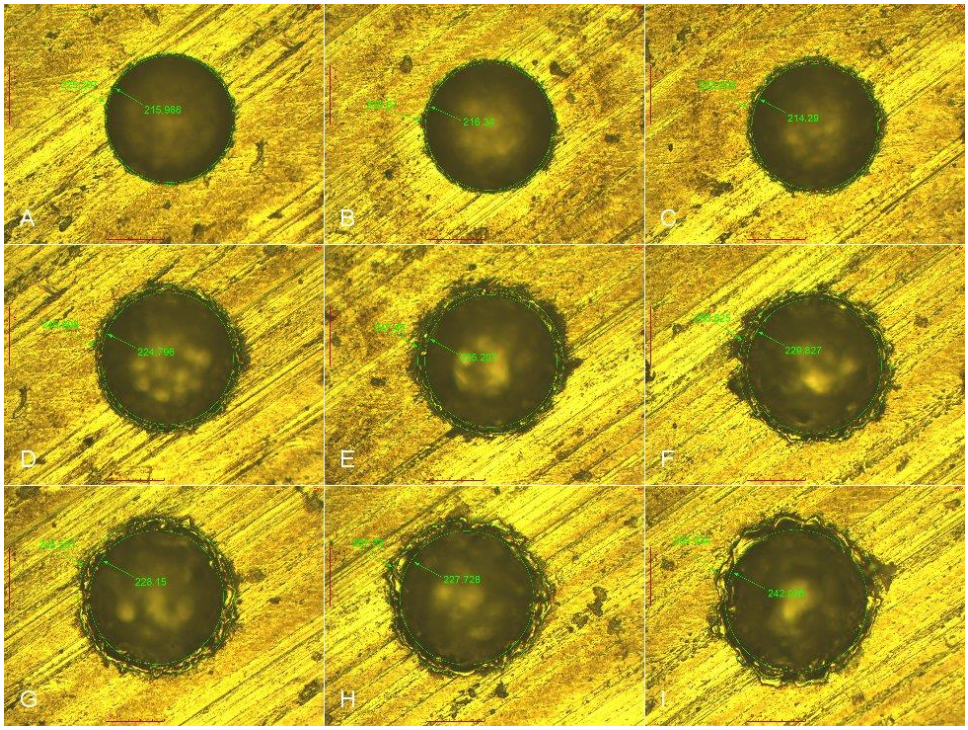

Figure 4.5: Effect of capacitance and voltage on circularity for µ-EDM of Ti-35Nb-7Zr-5Ta; (A) C=10nF & V=80V, (B) C=10nF & V=105V, (C) C=10nF & V=130V, (D) C=100nF & V=80V, (E) C=100nF & V=105V, (F) C=100nF & V=130V, (G) C=400nF & V=80V, (H) C=400nF & V=105V, (I) C=400nF & V=130V.

Figure 4.6 depicts the variation of circularity with the change in process parameters while keeping the rotation of the electrode constant. The circularity of the micro-holes created on the specimen is better at lower values of capacitance than the micro-holes acquired by machining at higher capacitance values. When the capacitance is lower, the circularity of µ-holes produced on Ti-35Nb-7Zr-5Ta is superior compared to machining with higher capacitance. This disparity arises because, at capacitance values, the current density is lower during the pulse-on time. Consequently, there is reduced wear on the µ-tool, leading to enhanced circularity in the machined micro-hole [63]. This phenomenon underscores the importance of controlling capacitance levels to optimize machining outcomes.

The augmentation in capacitance from 10 to 100nF at voltage levels of 80V, 105V, and 130V leads to a drop in the circularity of µ-holes by factors of 1.099, 1.068, and 1.071 respectively. Similarly, with the increase in the capacitance from 100nF to 400nF at voltage levels of 80V, 105V, and 130V the circularity of µ-holes drops by the factor of 1.133, 1.14, and 1.086 times respectively. However, with an increase of voltage from 80V to 105V at capacitance levels of 10nF, 100nF, and 400nF the circularity of µ-holes decreases upto 1.04, 1.01, and 1.016 times respectively. Moreover, with an increase of voltage from 105V to 130V at capacitance levels of 10nF, 100nF, and 400nF the circularity of µ-holes decreases upto 1.047, 1.05, and 1.0002 times respectively.

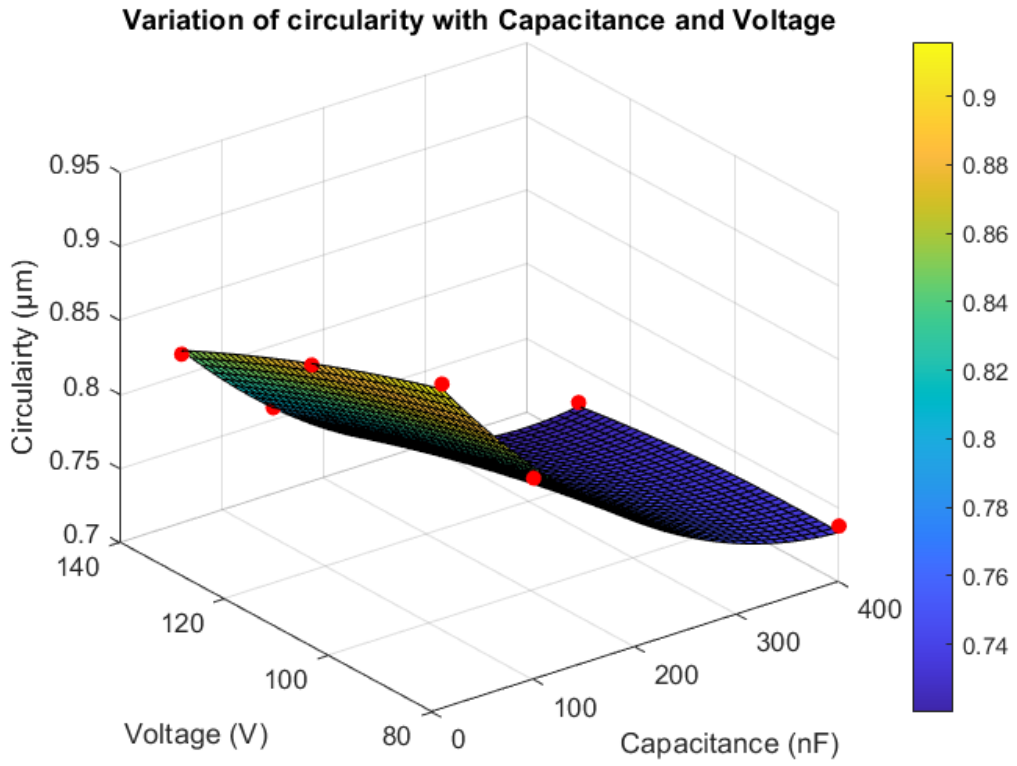

Figure 4.6: Influence of Capacitance and voltage Energy variation on the circularity of µ-holes for µ-EDM of Ti-35Nb-7Zr-5Ta.

It is observed that at a conventional significance threshold of 0.05 all coefficients, the intercept, the coefficient linked to the predictor x1 (capacitance), the coefficient linked to the predictor x2 (voltage), the coefficient of x12, and interaction terms x1:x2 exhibit statistical significance. The p-values for the intercept and x1, x2, x12, and x1:x2 are 2.3099e-06, 0.00040666, 0.0069218, 0.016336, and 0.033786 respectively. However, the coefficients pertaining to x22 do not demonstrate statistical significance, as outlined in Table A.4. The R-squared value is determined to be 0.995, suggesting that approximately 99.5% of the variability observed in the circularity can be accounted for by the capacitance and voltage.

4.1.5 Analysis of surface microhardness

One of the most significant parameters for assessing surface modifications produced by EDM operations is surface microhardness. The average μ-hardness of the un-machined surface is 284.39HV. The study of surface microhardness about capacitance and voltage during the micro-EDM of Ti-35Nb-7Zr-5Ta is depicted in Figure 4.7. There is a noticeable trend when the value of micro-hardness trends within this discharge energy range. This distinct pattern is observed because of the difference between consecutive voltage levels. Higher energy levels in the EDM process indeed raise the temperature differential between the tool and the workpiece. Increased temperature causes more material to melt and anneal on the surface [71]. Due to the flushing and environment, the molten material solidifies quickly on the workpiece surface, which might alter the mechanical properties of the machined surface. Consequently, increasing the surface micro-hardness may be attributed to this quick solidification.

Increasing capacitance from 10 to 100nF while maintaining the voltage at 80V, 105V, and 130V results in an augmentation of the microhardness of μ-hole surfaces by factors of 1.069, 1.019, and 1.023 respectively. Similarly, with the increase in the capacitance from 100nF to 400nF at voltage levels of 80V, 105V, and 130V microhardness of the μ-EDM treated surface augmented by 1.046, 1.049, and 1.008 times respectively. However, with an increase of voltage from 80V to 105V at capacitance levels of 10nF, 100nF, and 400nF the microhardness of the μ-EDM treated surface increases by the factor of 1.103, 1.031, and 1.034 times respectively. Moreover, with an increase of voltage from 105V to 130V at capacitance levels of 10nF, 100nF, and 400nF the microhardness of the μ-EDM treated surface increases by the factor of 1.042, 1.047, and 1.0059 times respectively.

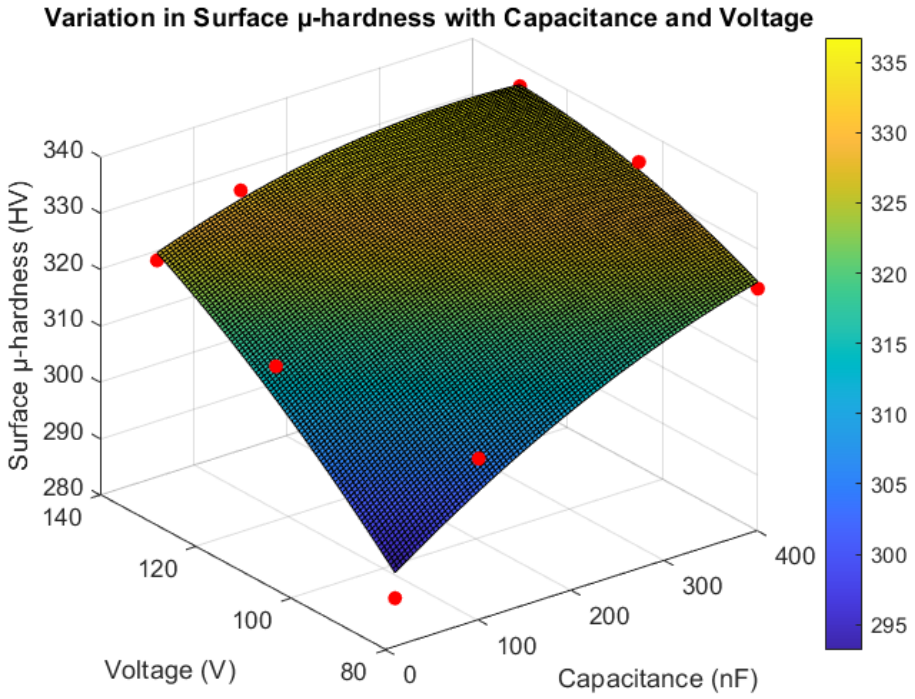

Figure 4.7: Influence of Capacitance and voltage variation on surface micro-hardness for µ-EDM of Ti-35Nb-7Zr-5Ta.

Employing a standard significance level of 0.05, it is evident that the intercept. the coefficient corresponding to the predictor and x2 (voltage) reveals statistical significance. The p-values for the intercept, x1, and x2 are 1.9951e-05, and 0.022955 respectively. In contrast, the coefficients related to x1 (capacitance) and the interaction terms x1:x2, x12, and x22 do not exhibit statistical significance, as shown in Table A.5. The model's R-squared value stands at 0.919, indicating that roughly 91.9% of the variability observed in the microhardness can be elucidated by the capacitance and voltage.

4.1.6 Analysis of surface roughness

Each spark in the µ-EDM process removes a small quantity of material from the workpiece, resulting in the formation of minute craters. The overall material removal is the cumulative outcome of numerous successive sparks. The achieved specific surface roughness (SR) appears to be intricately connected to the morphological characteristics of these craters, which is influenced by various machining parameters (C &V). Certainly, the volume of the crater is notably influenced by the pulse energy, with higher energy levels generally resulting in larger craters [72]. Figure 4.8 depicts the 3D mapping of the machined surface of the Ti-35Nb-7Zr-5Ta. This illustration demonstrates a distinct trend: as the voltage level rises from left to right and the capacitance level rises from top to bottom.

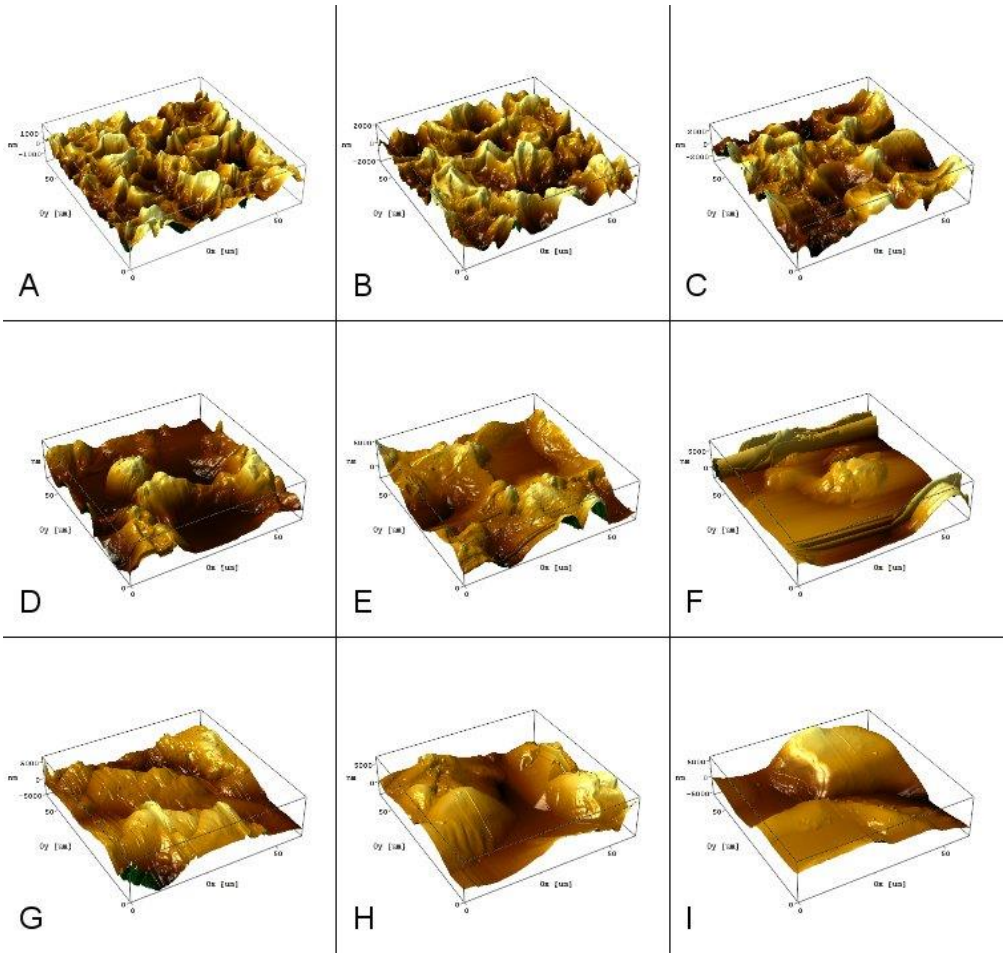

Figure 4.8: Effect of capacitance and voltage on surface roughness for µ-EDM of Ti-35Nb-7Zr-5Ta; (A) C=10nF & V=80V, (B) C=10nF & V=105V, (C) C=10nF & V=130V, (D) C=100nF & V=80V, (E) C=100nF & V=105V, (F) C=100nF & V=130V, (G) C=400nF & V=80V, (H) C=400nF & V=105V, (I) C=400nF & V=130V.

Figure 4.9 displays the average surface roughness values at various Capacitance and voltage levels. There is a clear direct correlation between the energy level and the average surface roughness values, suggesting that surface roughness and the energy used in the EDM process are related. The surface roughness of µ-holes demonstrates an increase by factors of 1.803, 2.012, and 1.74 times respectively as capacitance rises from 10 to 100nF at voltage levels of 80V, 105V, and 130V. Similarly, with the increase in the capacitance from 100nF to 400nF at voltage levels of 80V, 105V, and 130V the surface roughness of the µ-EDM treated surface increased by 1.198, 1.486, and 1.56 times respectively. However, with an increase of voltage from 80V to 105V at capacitance levels of 10nF, 100nF, and 400nF the surface roughness of µ-EDM treated surface increases by a factor of 1.376, 1.024, and 1.269 times respectively. Moreover, with an increase of voltage from 105V to 130V at capacitance levels of 10nF, 100nF, and 400nF the surface roughness of the µ-EDM treated surface increases upto 1.304, 1.079, and 1.146 times respectively.

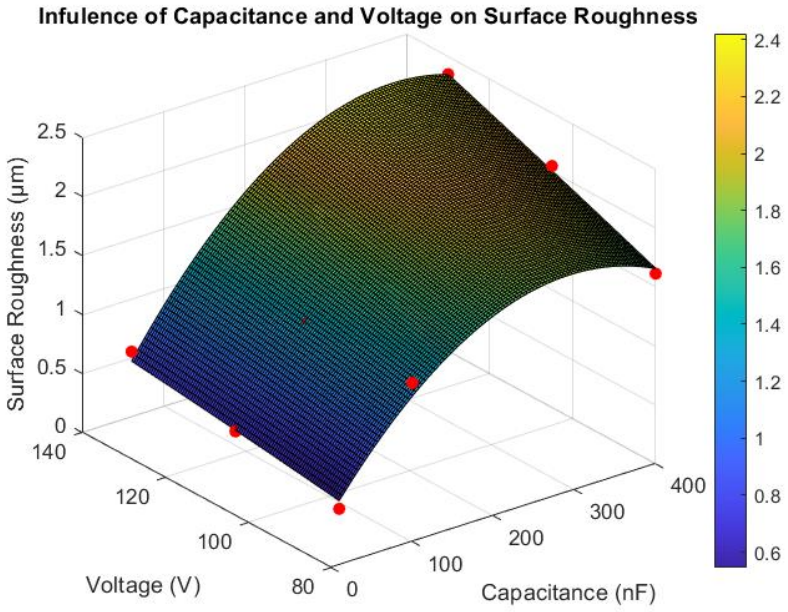

Figure 4.9: Influence of Capacitance and voltage Energy variation on surface roughness for µ-EDM of Ti-35Nb-7Zr-5Ta.

Utilizing a standard significance level of 0.05, it becomes evident that the intercept, the coefficient corresponding to predictor x1 (capacitance), $x1^2$, and x2 (voltage) exhibit statistical significance. The p-values for the intercept, x1, x2, and $x1^2$ are 0.00040942, 0.00097354, and 0.012474 respectively. However, the coefficient related to $x2^2$ and interaction terms does not meet the threshold for statistical significance, as outlined in Table A.6. The R-squared value stands at 0.995, indicating that roughly 99.5% of the variability observed in the surface roughness can be elucidated by the interplay between capacitance and voltage.

4.1.7 EDS analysis of Ti-35Nb-7Zr-5Ta

Energy Dispersive Spectroscopy (EDS) analysis was conducted on the surface of the sample before and after machining depicted in Figure 4.10, and the elemental chemical composition of the surface was investigated. The results of the EDS analysis are presented in Table 5. As anticipated and observed, the dominant elements in the chemical composition of the machined surface are titanium, niobium, tantalum, and zirconium (TNTZ), which are the constituent components of the Ti-35Nb-7Zr-5Ta alloy. Alongside these primary components, other elements such as carbon and oxygen are also present on the machined surface. The presence of carbon is attributed mainly to the decomposition of the dielectric fluid used during the EDM process. There is also some tungsten migration from the tool to the workpiece surface as evident from Table 4.1.

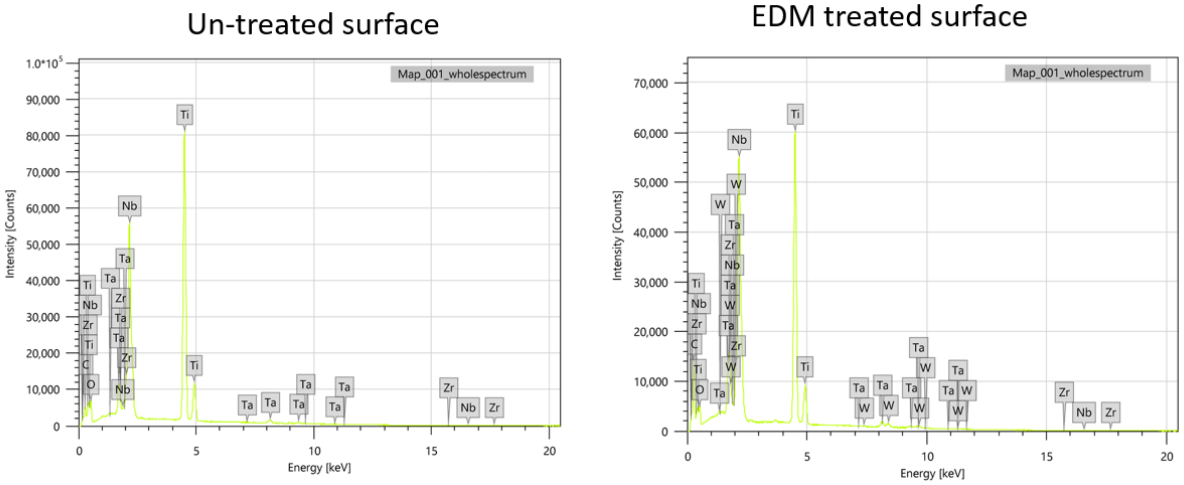

Figure 4.10: EDS analysis of Ti-35Nb-7Zr-5Ta of untreated and EDM surface.

Table 4.1 Chemical composition of Ti-35Nb-7Zr-5Ta un-treated and EDM surface.

Elements	Untreated surface		EDM surface	
	Mass%	**Atom%**	**Mass%**	**Atom%**
C	6.17±0.02	21.39±0.08	20.49±0.04	55.53±0.11
O	9.06±0.06	23.59±0.15	5.10±0.04	10.37±0.09
Ti	42.84±0.06	37.25±0.05	30.51±0.04	20.05±0.03
Zr	6.04±0.04	2.76±0.02	5.51±0.04	1.97±0.01
Nb	30.98±0.06	13.89±0.03	29.40±0.06	10.30±0.02
Ta	4.91±0.04	1.13±0.01	4.51±0.04	0.92±0.01
W	-	-	4.88±0.04	0.86±0.01
Total	**100.00**	**100.00**	**100.00**	**100.00**

4.2 Micro EDM of Ti-29Nb-13Ta-4.6Zr

4.2.1 Analysis of MRR

Figure 4.11 depicts the changes in Material Removal Rate (MRR) with variations in capacitance (C) ranges from 10 to 400 nF, where each curve on the plot represents a different voltage level (80, 105, and 130V). The observation from Fig. 18 demonstrates that the MRR displays a rapid increase when the capacitance increases from 10 to 100 nF. However, the skewness of MRR begins to decrease when the capacitance increases from 100 to 400 nF. This gradual increase is due to the considerably high energy level in this phase, which raises the temperature between the workpiece and the tool. This rapid increase in temperature breaks the hydrocarbon in flushing oil and forms a layer of carbon debris on the workpiece surface. This layer of carbon debris accumulates on the surface of the workpiece, preventing smooth machining in addition to

limiting the effective and steady electrical sparks. Consequently, the MRR increases marginally. The finding emphasizes the intricate relationship between the process parameters and MRR on the effectiveness of the EDM process, as well as the potential consequences of high temperatures and energy on machining efficiency.

With an increase in capacitance from 10 to 100nF at voltage levels of 80V, 105V, and 130V the MRR increases 4.098, 4.445, and 3.953 times respectively. Similarly, with the increase in the capacitance from 100nF to 400nF at voltage levels of 80V, 105V, and 130V the MRR increases 1.661, 1.146, and 1.221 times respectively. However, with an increase of voltage from 80V to 105V at capacitance levels of 10nF, 100nF, and 400nF the MRR increases upto 1.575, 1.708, and 1.178 times respectively. Moreover, with an increase of voltage from 105V to 130V at capacitance levels of 10nF, 100nF, and 400nF the MRR increases upto 1.28, 1.138, and 1.223 times respectively.

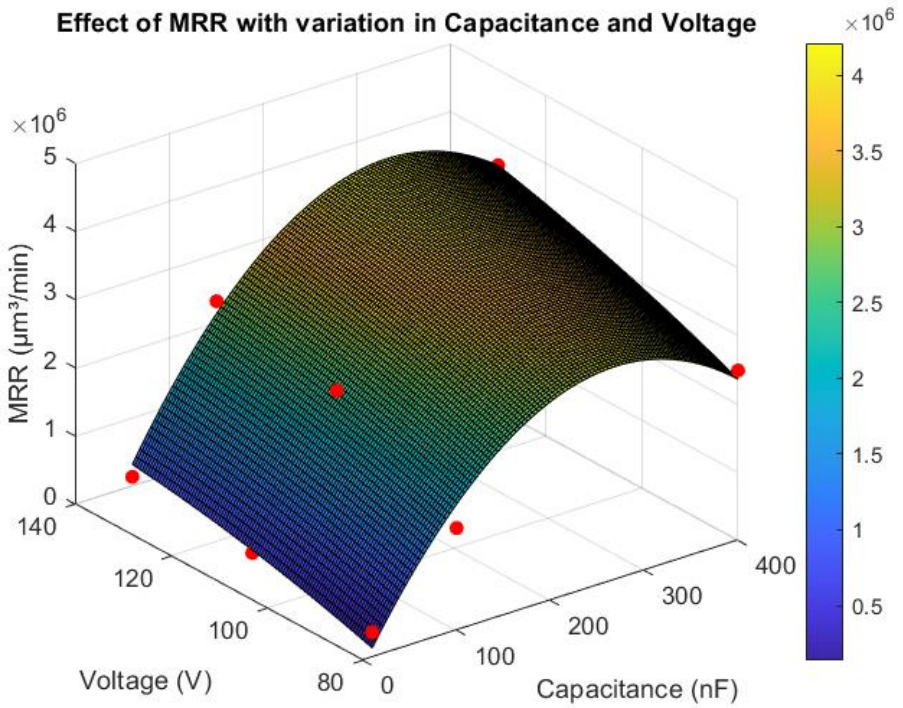

Figure 4.11: Influence of Capacitance and Voltage Variation on Material Removal Rate for µ-EDM of Ti-29Nb-7Zr-4.6Zr.

At a standard significance level of 0.05, the intercept, the coefficient for predictor x1 (capacitance), $x1^2$, and x2 (voltage) demonstrate statistical significance, the p-values for intercept and x1 are 0.0017781 and 0.0028481, 0.034791, and 0.014909 respectively. However, the coefficients for $x2^2$, the interaction terms x1:x2 and x22 do not exhibit statistical significance as displayed in Table A.7. The R-squared value for the model is 0.973 suggesting that approximately 97.3% of the variability observed in the MRR can be accounted for by the capacitance and voltage.

4.2.2 4.2.2 Analysis of overcut

Figure 4.12 depicts the Overcut (OC) as it varies with the capacitance ranging from 10 to 400 nF while keeping the spindle speed constant at 1000 rpm, and positive workpiece polarity. The figure shows that OC exhibits a gradual and monotonically increasing trend as capacitance increases. Lower discharge energy levels cause smaller craters to form, which in turn causes less overcut because there is less material removed in each discharge. On the other hand, overcut tends to rise with larger discharge energy levels. This can also be explained by the greater span of discharge columns, which last longer than those at low energy levels. However, after 100nF, OC is found to increase marginally, which may be due to the accumulation of debris at the tool and workpiece surface at high energy levels [62].

As capacitance escalates from 10 to 100nF across voltage thresholds of 80V, 105V, and 130V, the overcut of µ-holes amplifies by factors of 1.721, 1.84, and 1.67 respectively. Similarly, with the increase in the capacitance from 100nF to 400nF at voltage levels of 80V, 105V, and 130V the overcut of µ-holes increases by 1.143, 1.335, and 1.236 times respectively. However, with an increase of voltage from 80V to 105V at capacitance levels of 10nF, 100nF, and 400nF the overcut of µ-holes upto 1.098, 1.175, and 1.372 times respectively. Moreover, with an increase of voltage from 105V to 130V at capacitance levels of 10nF, 100nF, and 400nF the overcut of µ-holes increases upto 1.312, 1.195, and 1.107 times respectively.

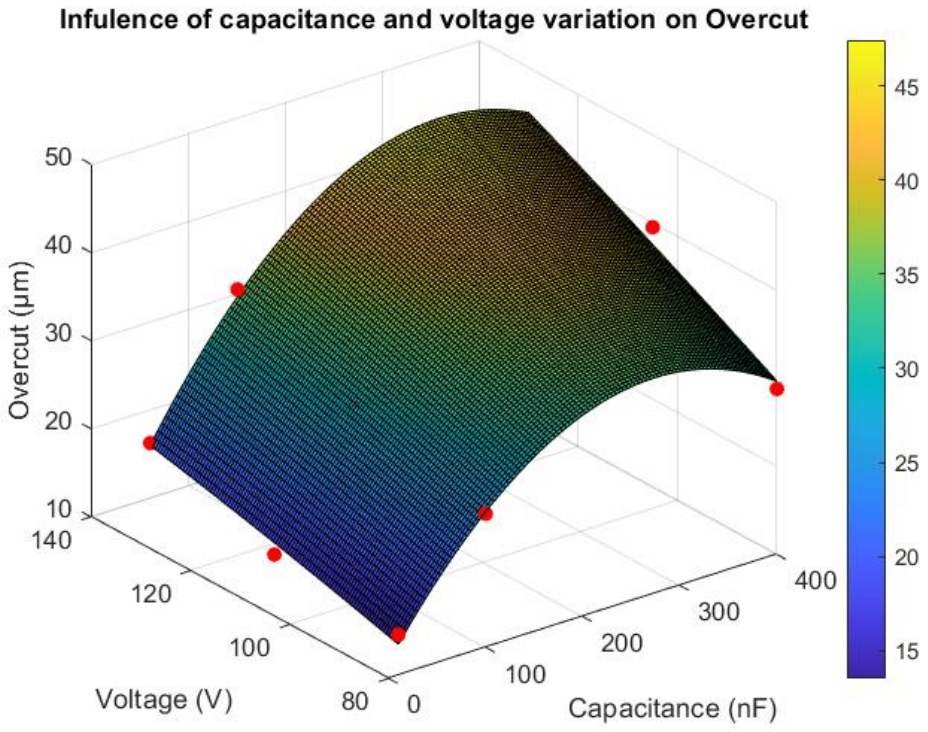

Figure 4.12: Influence of Capacitance and voltage variation on overcut during µ-EDM of Ti-29Nb-13Ta-4.6Zr.

It is evident that the intercept and the coefficient at a standard significance level of 0.05 pertaining to predictor x1 (capacitance), the coefficient for predictor x2 (voltage), and $x1^2$ demonstrate statistical significance, the p-values for intercept, x1, x2, and $x1^2$ are 0.000243, 0.001199, 0.006044, and 0.009469 respectively. In contrast, the coefficients linked to x1:x2, and $x2^2$ do not exhibit the requisite criteria for statistical significance, as elucidated in Table A.8. The R-squared value of the model is computed to be 0.987, indicating that approximately 98.7% of the variance observed in the overcut can be ascribed to the interplay between capacitance and voltage.

4.2.3 Analysis of crater size

In an RC-type pulse generator, the material removal process is greatly influenced by the discharge energy per pulse, as it has a direct relation with capacitance and voltage [70]. Figure 4.13 depicts the surface topography at different capacitances and voltages, with constant electrode rotating speed. The results show that a higher capacitance causes bigger craters and a rougher surface finish at different levels of voltage. At the smallest capacitance (10nF) and voltage (80 V) as seen in Figure 4.13(A), the surface finish is finer, and it gets rougher as shown in Figure 4.13(B and C). This is because the lowest capacitance and voltage results in the lowest discharge energy. Figure 4.13(C, D, and F) illustrates that when the energy levels are high, there is a significant formation of larger craters that also exhibit more overlapping. The presence of larger-sized craters and craters overlapping typically indicates a rough surface texture.

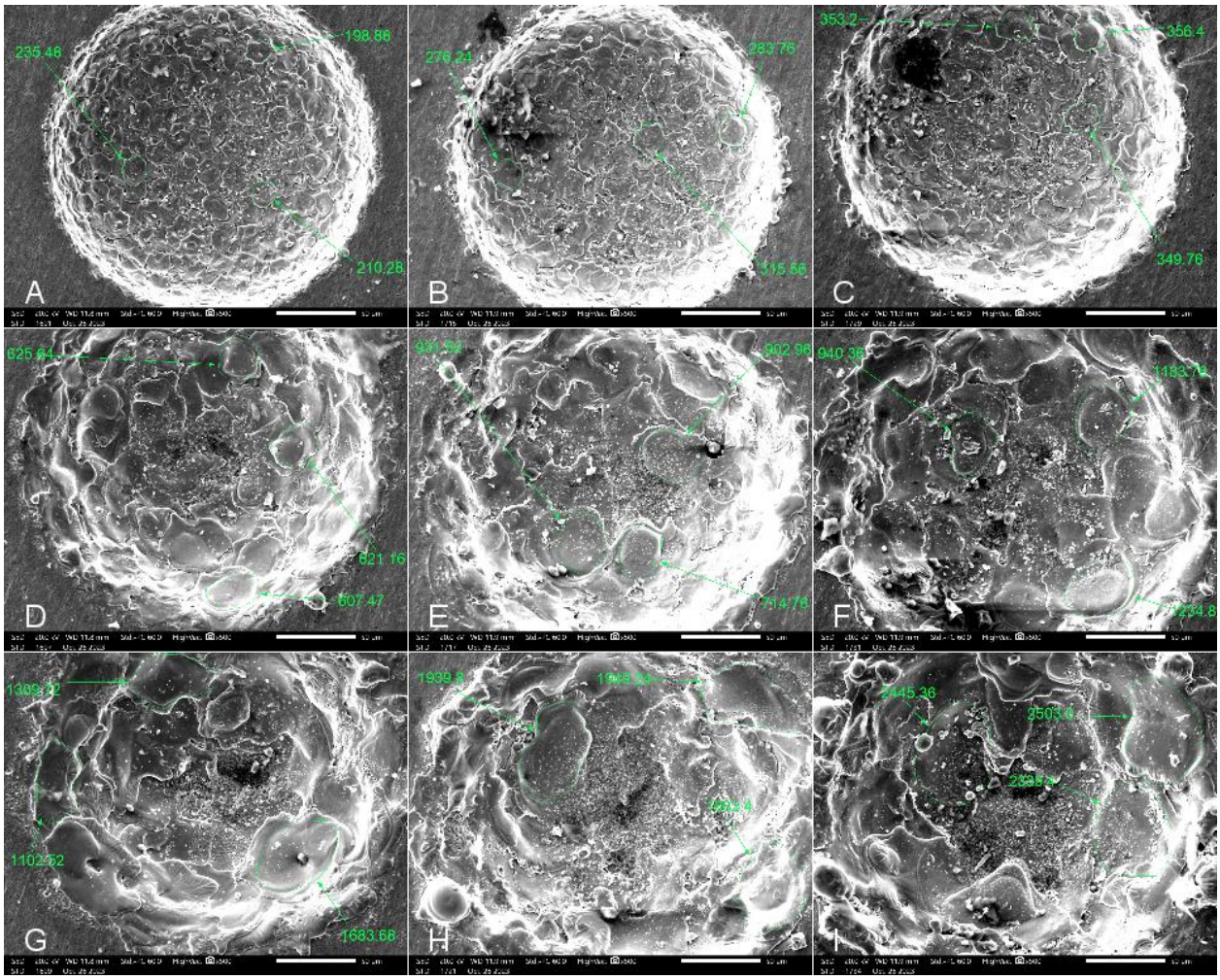

Figure 4.13: Effect of capacitance and voltage on crater size for µ-EDM of Ti-29Nb-13Ta-4.6Zr; (A) C=10nF & V=80V, (B) C=10nF & V=105V, (C) C=10nF & V=130V, (D) C=100nF & V=80V, (E) C=100nF & V=105V, (F) C=100nF & V=130V, (G) C=400nF & V=80V, (H) C=400nF & V=105V, (I) C=400nF & V=130V.

Figure 4.14 depicts the plot of the average crater area with changes in process parameters (capacitance and voltage), the average crater size is determined using ImageJ 1.54d software. The plot depicts that the average crater size tends to rise as discharge energy per pulse increases. This phenomenon happens due to a discharge column that is comparably broader at higher energy levels [62, 63]. Higher energy tends to generate large-sized craters, so increases the crater overlapping, surface roughness, and MRR.

Increasing capacitance from 10 to 100nF while maintaining voltage at 80V, 105V, and 130V results in an augmentation of the crater size by factors of 2.876, 2.686, and 3.17 times respectively. Similarly, with the increase in the capacitance from 100nF to 400nF at voltage levels of 80V, 105V, and 130V the crater size increases by 2.209, 2.232, and 2.17 times respectively. However, with an increase of voltage from 80V to 105V at capacitance levels of 10nF, 100nF, and 400nF the crater size increases upto 1.472, 1.375, and 1.389 times respectively. Moreover, with an increase of voltage from 105V to 130V at capacitance levels of 10nF, 100nF, and 400nF the crater size increases upto 1.116, 1.317, and 1.28 times respectively.

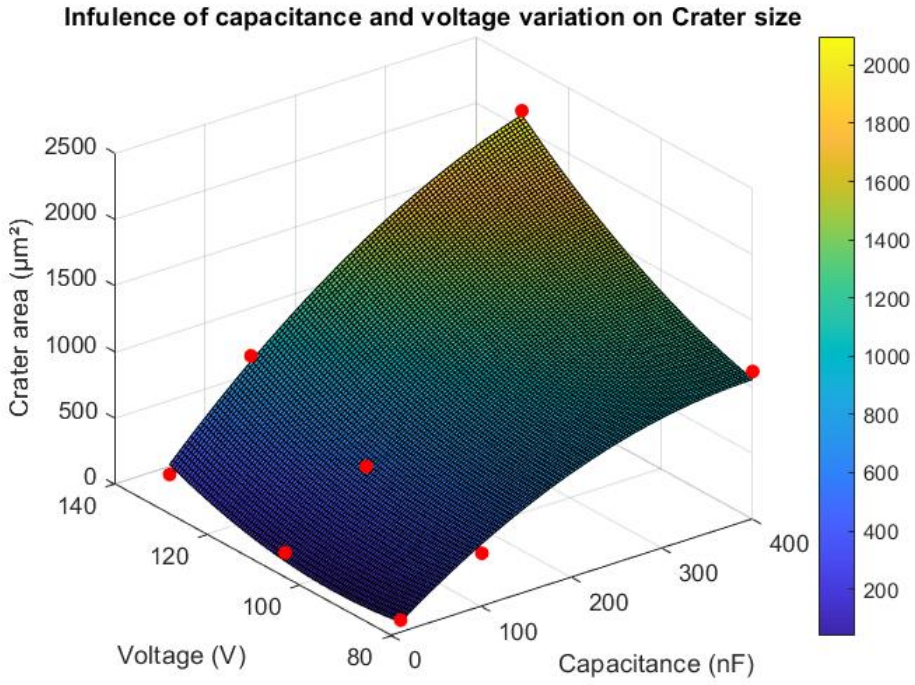

Figure 4.14: Influence of Capacitance and voltage variation on crater size for µ-EDM of Ti-29Nb-13Ta-4.6Zr.

It is discerned that employing a standard significance level of 0.05, the intercept and the coefficient associated with predictor x1 (capacitance), x2 (voltage), and interaction term x1:x2, evince statistical significance. The p-values for the intercept, x1, x2, and x1:x2 are notably diminutive, at 0.0031062, 0.0012443, 0.0065883, and 0.02574, respectively. Conversely, the coefficients for $x1^2$ and $x2^2$ do not exhibit statistical significance, as delineated in Table A.9. The R-squared value is computed at 0.991, signifying that approximately 99.1% of the variance observed in the crater size can be explicated by the interplay between capacitance and voltage.

4.2.4 Analysis of circularity

Figure 4.15 displays the results of the measurement of the circularity of the micro-holes drilled on Ti-29Nb-13Ta-4.6Zr using ImageJ version 1.45d software. This figure shows how circularity varies with capacitance horizontally keeping the voltage constant and varies with voltage vertically keeping the capacitance constant.

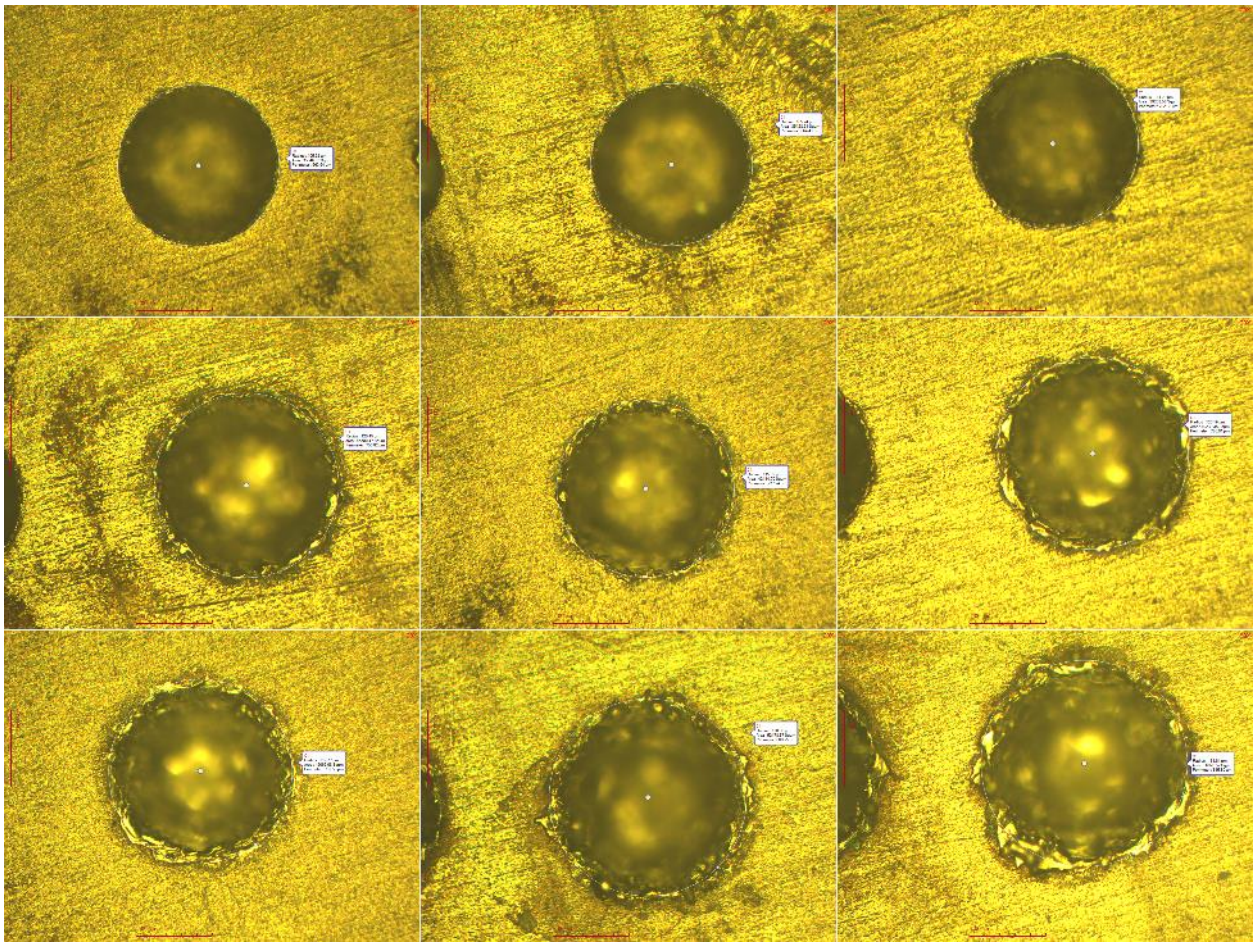

Figure 4.15: Effect of capacitance and voltage on circularity for µ-EDM of Ti-29Nb-13Ta-4.6Zr; (A) C=10nF & V=80V, (B) C=10nF & V=105V, (C) C=10nF & V=130V, (D) C=100nF & V=80V, (E) C=100nF & V=105V, (F) C=100nF & V=130V, (G) C=400nF & V=80V, (H) C=400nF & V=105V, (I) C=400nF & V=130V.

Figure 4.16 depicts the variation of circularity with the change in process parameters while keeping the rotation of the electrode constant. The circularity of the micro-holes created on the specimen is better at lower values of capacitance than the micro-holes acquired by machining at higher capacitance values. When the capacitance is lower, the circularity of µ-holes produced on Ti-29Nb-13Ta-4.6Zr is superior compared to machining with higher capacitance. This disparity arises because, at capacitance values, the current density is lower during the pulse-on time. Consequently, there is reduced wear on the µ-tool, leading to enhanced circularity in the machined micro-hole [63]. This phenomenon underscores the importance of controlling capacitance levels to optimize machining outcomes.

The augmentation in capacitance from 10 to 100nF at voltage levels of 80V, 105V, and 130V leads to a drop in the circularity of µ-holes by factors of 1.10047, 1.0635, and 1.0953 respectively. Similarly, with the increase in the capacitance from 100nF to 400nF at voltage levels of 80V, 105V, and 130V the circularity of µ-holes drops by the factor of 1.133, 1.135, and 1.099 times respectively. However, with an increase of voltage from 80V to 105V at capacitance levels of 10nF, 100nF, and 400nF the circularity of µ-holes decreases upto 1.045, 1.01, and 1.014 times

respectively. Moreover, with an increase of voltage from 105V to 130V at capacitance levels of 10nF, 100nF, and 400nF the circularity of µ-holes decreases upto 1.018, 1.048, and 1.015 times respectively.

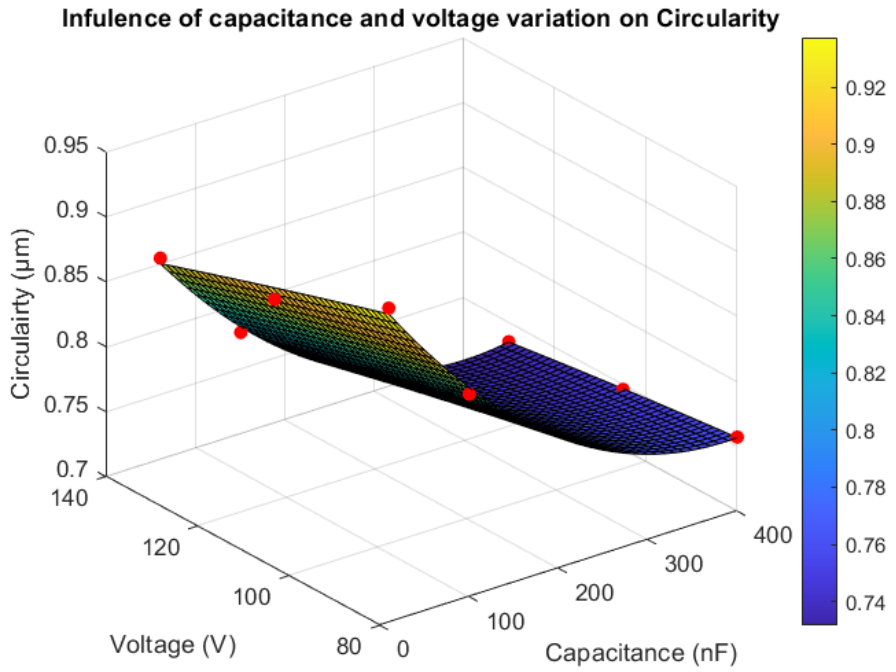

Figure 4.16: Influence of Capacitance and voltage Energy variation on the circularity of µ-holes for µ-EDM of Ti-29Nb-13Ta-4.6Zr.

It is observed that at a conventional significance threshold of 0.05 all coefficients, the intercept, the coefficient linked to the predictor x1 (capacitance), the coefficient linked to the predictor x2 (voltage), and the coefficient of $x1^2$, exhibit statistical significance. The p-values for the intercept and x1, x2, $x1^2$, and x1:x2 are 2.979e-06, 0.000434, 0.011, and 0.014627 respectively. However, the coefficients pertaining to $x2^2$ and interaction term x1:x2 do not demonstrate statistical significance, as outlined in Table A.10. The R-squared value is determined to be 0.995, suggesting that approximately 99.4% of the variability observed in the circularity can be accounted for by the capacitance and voltage.

4.2.5 Analysis of surface microhardness

One of the most significant parameters for assessing surface modifications produced by EDM operations is surface microhardness. The average µ-hardness of the un-machined surface is 284.39HV. The study of surface microhardness about capacitance and voltage during the micro-EDM of Ti-29Nb-13Ta-4.6Zr is depicted in Figure 4.17. There is a noticeable trend when the value of micro-hardness trends within this discharge energy range. This distinct pattern is observed because of the difference between consecutive voltage levels. Higher energy levels in the EDM

process indeed raise the temperature differential between the tool and the workpiece. Increased temperature causes more material to melt and anneal on the surface [71]. Due to the flushing and environment, the molten material solidifies quickly on the workpiece surface, which might alter the mechanical properties of the machined surface. Consequently, increasing the surface micro-hardness may be attributed to this quick solidification.

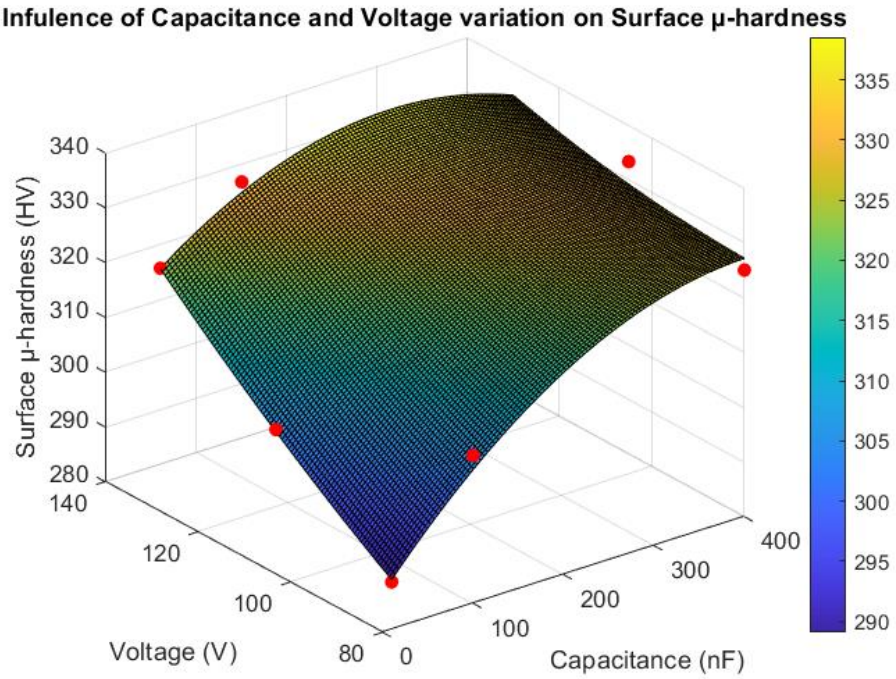

Figure 4.17: Influence of Capacitance and voltage variation on surface micro-hardness for µ-EDM of Ti-29Nb-13Ta-4.6Zr.

Employing a standard significance level of 0.05, it is evident that the intercept. the coefficient corresponding to the predictor and x1 (capacitance), x2 (voltage), and x1:x2 reveals statistical significance. In contrast, the coefficients related to $x1^2$ and $x2^2$ do not exhibit statistical significance, as shown in Table A.11. The model's R-squared value stands at 0.996, indicating that roughly 99.6% of the variability observed in the microhardness can be elucidated by the capacitance and voltage.

4.2.6 Analysis of surface roughness

Each spark in the µ-EDM process removes a small quantity of material from the workpiece, resulting in the formation of minute craters. The overall material removal is the cumulative outcome of numerous successive sparks. The achieved specific surface roughness (SR) appears to be intricately connected to the morphological characteristics of these craters, which is influenced by various machining parameters (C &V). Certainly, the volume of the crater is notably influenced by the pulse energy, with higher energy levels generally resulting in larger craters [72]. Figure 4.18 depicts the 3D mapping of the machined surface of the Ti-29Nb-13Ta-4.6Zr. This illustration

demonstrates a distinct trend: as the voltage level rises from left to right and the capacitance level rises from top to bottom.

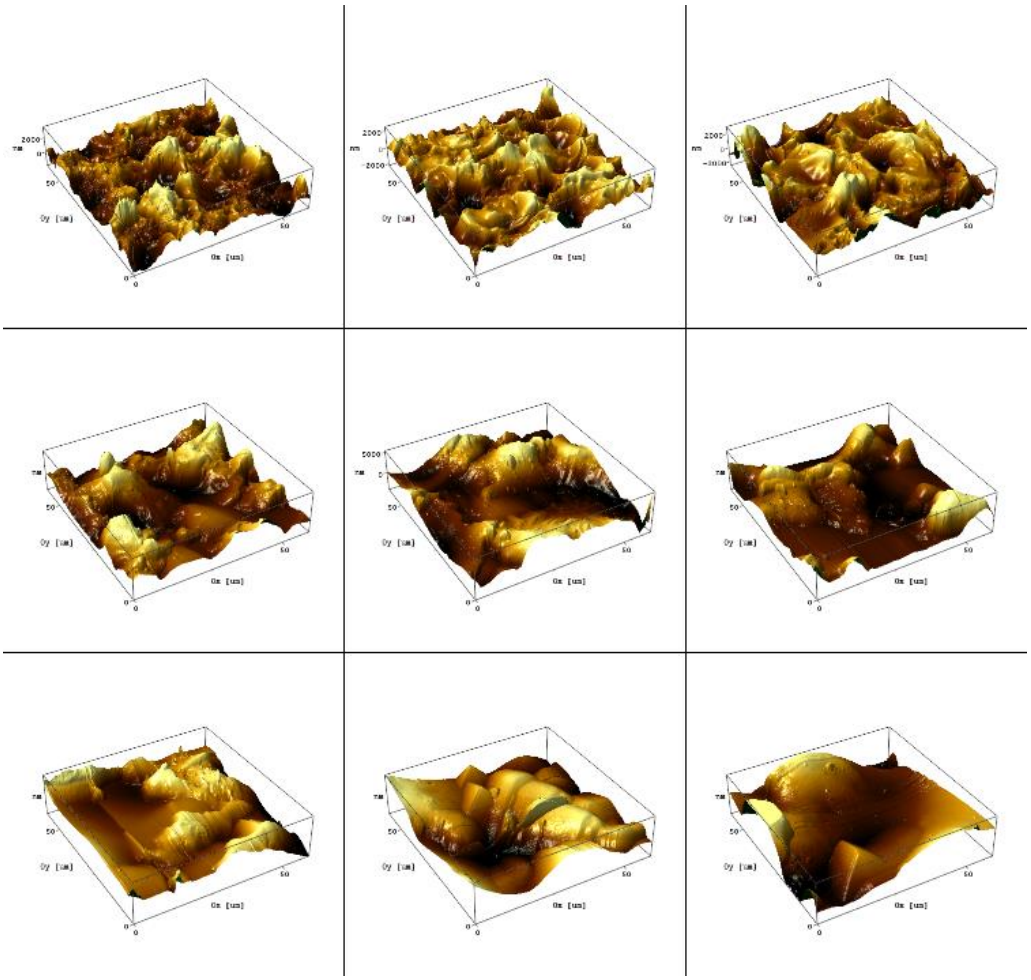

Figure 4.18: Effect of capacitance and voltage on surface roughness for µ-EDM of Ti-29Nb-13Ta-4.6Zr; (A) C=10nF & V=80V, (B) C=10nF & V=105V, (C) C=10nF & V=130V, (D) C=100nF & V=80V, (E) C=100nF & V=105V, (F) C=100nF & V=130V, (G) C=400nF & V=80V, (H) C=400nF & V=105V, (I) C=400nF & V=130V.

Figure 4.19 displays the average surface roughness values at various Capacitance and voltage levels. There is a clear direct correlation between the energy level and the average surface roughness values, suggesting that surface roughness and the energy used in the EDM process are related. The surface roughness of µ-holes demonstrates an increase by factors of 1.803, 2.012, and 1.74 times respectively as capacitance rises from 10 to 100nF at voltage levels of 80V, 105V, and 130V. Similarly, with the increase in the capacitance from 100nF to 400nF at voltage levels of 80V, 105V, and 130V the surface roughness of the µ-EDM treated surface increased by 1.198, 1.486, and 1.56 times respectively. However, with an increase of voltage from 80V to 105V at capacitance levels of 10nF, 100nF, and 400nF the surface roughness of µ-EDM treated surface increases by a factor of 1.376, 1.024, and 1.269 times respectively. Moreover, with an increase of voltage from 105V to 130V at capacitance levels of 10nF, 100nF, and 400nF the surface roughness of the µ-EDM treated surface increases upto 1.304, 1.079, and 1.146 times respectively.

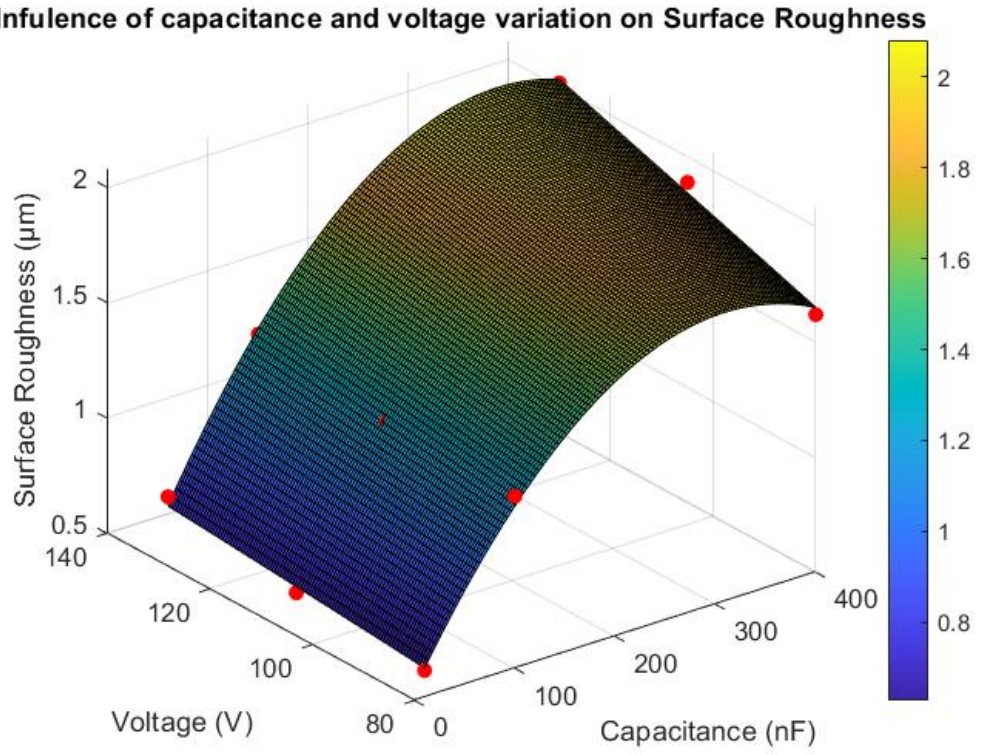

Figure 4.19: Influence of Capacitance and voltage Energy variation on surface roughness for µ-EDM of Ti-29Nb-13Ta-4.6Zr.

Utilizing a standard significance level of 0.05, it becomes evident that the intercept, the coefficient corresponding to predictor x1 (capacitance), $x1^2$, and x2 (voltage) exhibit statistical significance. However, the coefficient related to $x2^2$ and interaction terms does not meet the threshold for statistical significance, as outlined in Table A.12. The R-squared value stands at 0.996, indicating that roughly 99.6% of the variability observed in the surface roughness can be elucidated by the interplay between capacitance and voltage.

4.2.7 EDS analysis of Ti-29Nb-13Ta-4.6Zr

Energy Dispersive Spectroscopy (EDS) analysis was conducted on the surface of the sample before and after machining depicted in Figure 4.20, and the elemental chemical composition of the surface was investigated. The results of the EDS analysis are presented in Table 5. As anticipated and observed, the dominant elements in the chemical composition of the machined surface are titanium, niobium, tantalum, and zirconium (TNTZ), which are the constituent components of the Ti-29Nb-13Ta-4.6Zr alloy. Alongside these primary components, other elements such as carbon and oxygen are also present on the machined surface. The presence of carbon is attributed mainly to the decomposition of the dielectric fluid used during the EDM process. There is also some tungsten migration from the tool to the workpiece surface as evident from Table 4.2.

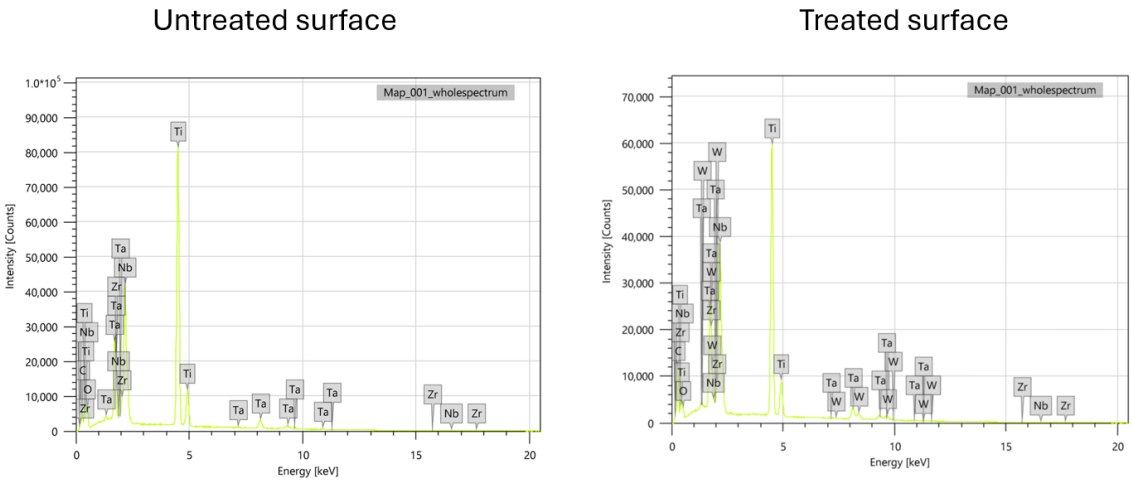

Figure 4.20: EDS analysis of Ti-29Nb-13Ta-4.6Zr of untreated and EDM surface.

Table 4.2 Chemical composition of Ti-29Nb-13Ta-4.6Zr un-treated and EDM surface.

Elements	Untreated surface		EDM surface	
	Mass%	**Atom%**	**Mass%**	**Atom%**
C	6.32±0.02	22.44±0.08	17.72±0.04	55.06±0.12
O	8.97±0.05	23.92±0.14	2.26±0.03	5.26±0.07
Ti	43.67±0.05	37.10±0.05	31.13±0.05	24.25±0.04
Zr	3.78±0.04	1.77±0.02	3.34±0.04	1.41±0.02
Nb	24.74±0.06	11.36±0.03	23.96±0.06	9.61±0.02
Ta	12.52±0.04	3.42±0.01	12.49±0.05	2.58±0.01
W	-	-	9.02±0.06	1.83±0.01
Total	**100.00**	**100.00**	**100.00**	**100.00**

4.3 Micro-WEDM of Ti-35Nb-7Zr-5Ta

4.3.1 Analysis of kerf width

Figure 4.21 displays the results of the measurement of the kerf width of the cuts machined on Ti-35Nb-7Zr-5Ta using ImageJ version 1.45d software. This figure shows how kerf width varies with capacitance horizontally keeping the voltage constant and varies with voltage vertically keeping the capacitance constant.

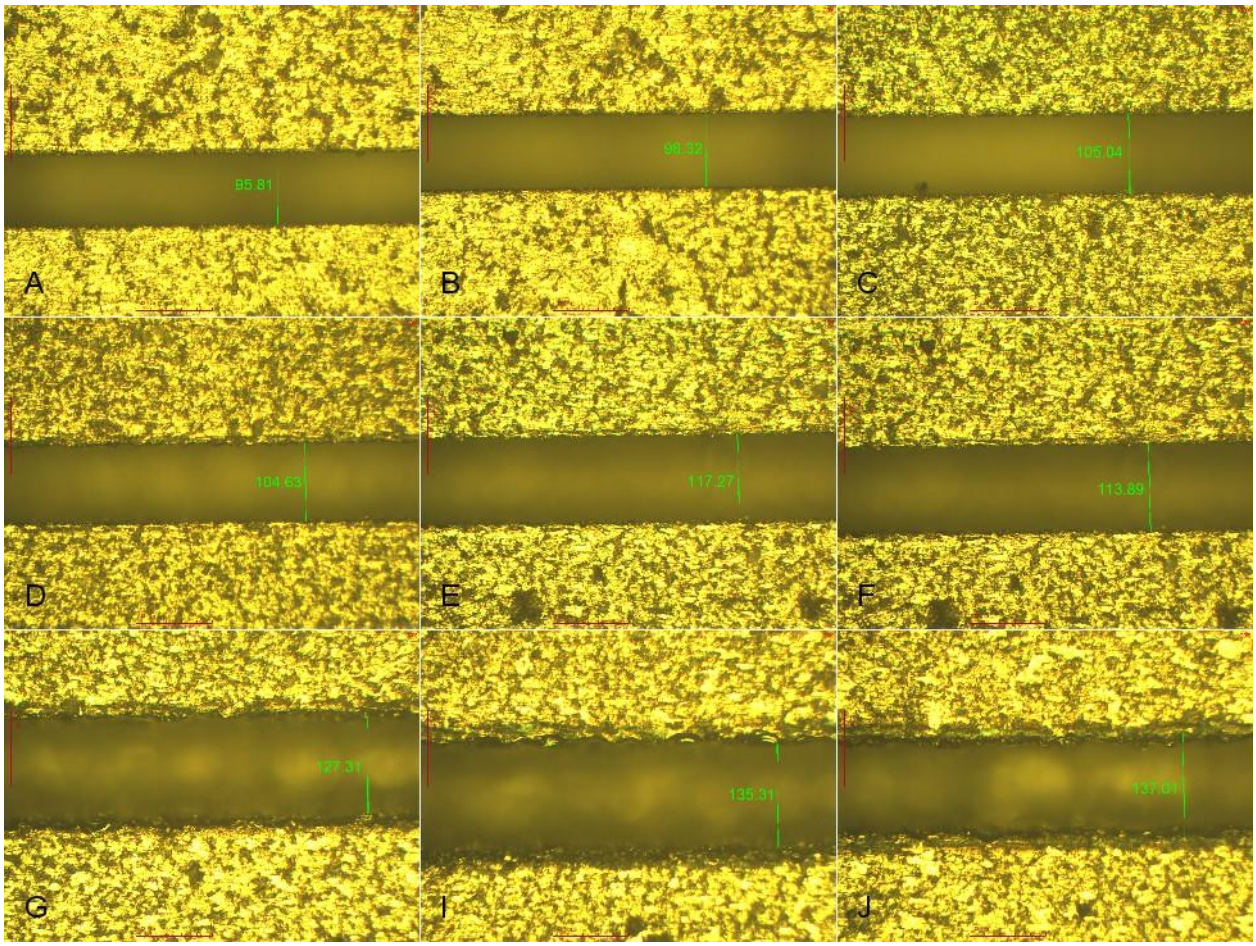

Figure 4.21: Effect of capacitance and voltage on kerf width during µ-WEDM of Ti-35Nb-7Zr-5Ta; (A) C=10nF & V=80V, (B) C=10nF & V=105V, (C) C=10nF & V=130V, (D) C=100nF & V=80V, (E) C=100nF & V=105V, (F) C=100nF & V=130V, (G) C=400nF & V=80V, (H) C=400nF & V=105V, (I) C=400nF & V=130V.

Figure 4.22 depicts the kerf width as it varies with the capacitance ranging from 10 to 400 nF while keeping the spindle speed constant at 1000 rpm, and positive workpiece polarity. The figure shows that kerf width exhibits a gradual and monotonically increasing trend as capacitance increases. Lower discharge energy levels cause smaller craters to form, which in turn causes less overcut because there is less material removed in each discharge. On the other hand, kerf tends to rise with larger discharge energy levels. This can also be explained by the greater span of discharge columns, which last longer than those at low energy levels.

As capacitance escalates from 1 to 10nF across voltage thresholds of 80V, 95V, and 110V, the kerf width amplifies by factors of 1.102, 1.119, and 1.161 respectively. Similarly, with the increase in the capacitance from 10nF to 100nF at voltage levels of 80V, 95V, and 110V the kerf width increases by 1.196, 1.062, and 1.095 times respectively. However, with an increase of voltage from 80V to 95V at capacitance levels of 1nF, 10nF, and 100nF the kerf width upto 1.021, 1.112, and 1.011 times respectively. Moreover, with an increase of voltage from 95V to 110V at capacitance levels of 1nF, 10nF, and 100nF the kerf width increases upto 1.051, 1.018, and 1.045 times respectively.

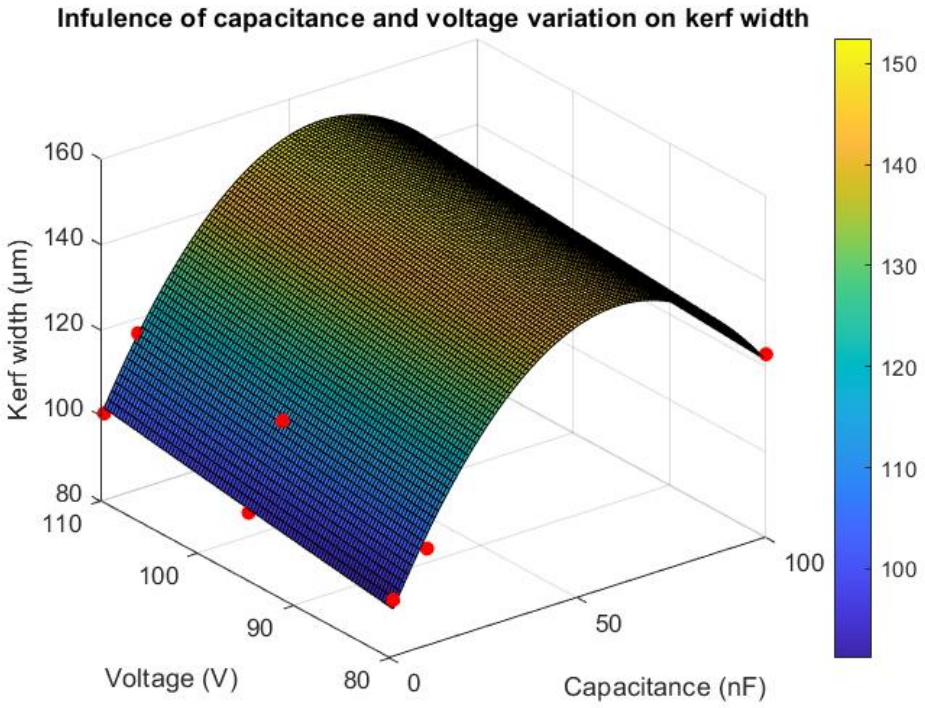

Figure 4.22: Influence of Capacitance and voltage variation on kerf width during µ-WEDM of Ti-35Nb-7Zr-5Ta.

It is evident that the intercept and the coefficient at a standard significance level of 0.05 pertaining to predictor x1 (capacitance), the coefficient for predictor x2 (voltage), and $x1^2$ demonstrate statistical significance. In contrast, the coefficients linked to x1:x2, and x^2 do not exhibit the requisite criteria for statistical significance, as elucidated in Table A.13. The R-squared value of the model is computed to be 0.97, indicating that approximately 97% of the variance observed in the overcut can be ascribed to the interplay between capacitance and voltage.

4.3.2 Analysis of crater size

In an RC-type pulse generator, the material removal process is greatly influenced by the discharge energy per pulse, as it has a direct relation with capacitance and voltage [70]. Figure 4.23 depicts the surface topography at different capacitances and voltages, with constant wire speed. The results show that a higher capacitance causes bigger craters and a rougher surface finish at different levels of voltage. At the smallest capacitance (1nF) and voltage (80 V) as seen in Figure 4.23(A), the surface finish is finer, and it gets rougher as shown in Figure 4.23(B and C). This is because the lowest capacitance and voltage results in the lowest discharge energy. Figure 4.23(C, D, and F) illustrates that when the energy levels are high, there is a significant formation of larger craters that also exhibit more overlapping. The presence of larger-sized craters and craters overlapping typically indicates a rough surface texture.

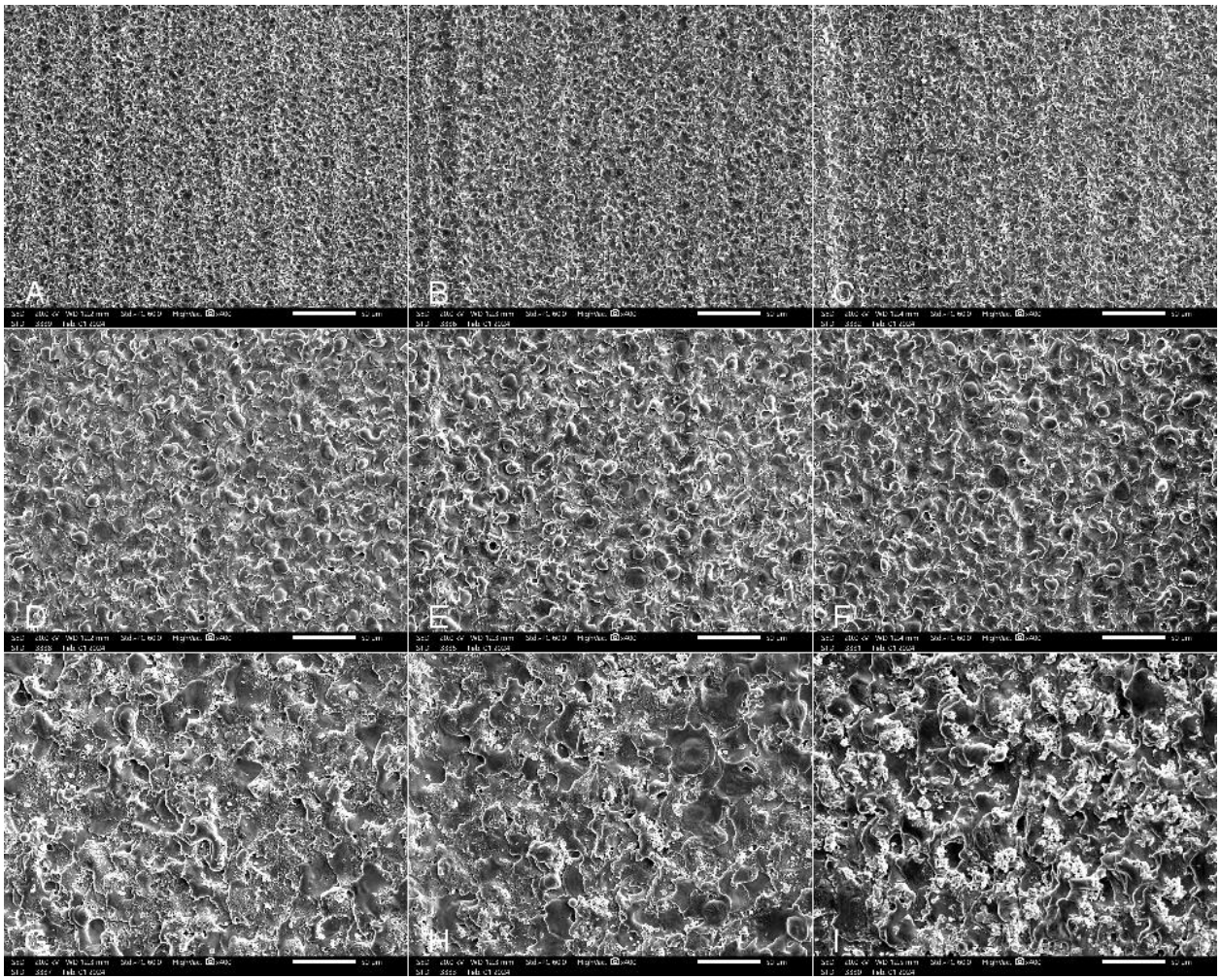

Figure 4.23: Effect of capacitance and voltage on crater size for µ-WEDM of Ti-35Nb-7Zr-5Ta; (A) C=10nF & V=80V, (B) C=10nF & V=105V, (C) C=10nF & V=130V, (D) C=100nF & V=80V, (E) C=100nF & V=105V, (F) C=100nF & V=130V, (G) C=400nF & V=80V, (H) C=400nF & V=105V, (I) C=400nF & V=130V.

Figure 4.24 depicts the plot of the average crater area with changes in process parameters (capacitance and voltage), the average crater size is determined using ImageJ 1.54d software. The plot depicts that the average crater size tends to rise as discharge energy per pulse increases. This phenomenon happens due to a discharge column that is comparably broader at higher energy levels [62, 63]. Higher energy tends to generate large-sized craters, so it increases the crater overlapping, surface roughness, and MRR.

Increasing capacitance from 1 to 10nF while maintaining voltage at 80V, 95V, and 110V results in an augmentation of the crater size by factors of 5.999, 4.84, and 4.80 times respectively. Similarly, with the increase in the capacitance from 10nF to 100nF at voltage levels of 80V, 95V, and 110V the crater size increases by 5.676, 6.031, and 6.483 times respectively. However, with an increase of voltage from 80V to 95V at capacitance levels of 1nF, 10nF, and 100nF the crater size increases upto 1.295, 1.045, and 1.110 times respectively. Moreover, with an increase of

voltage from 95V to 110V at capacitance levels of 1nF, 10nF, and 100nF the crater size increases upto 1.165, 1.158, and 1.244 times respectively.

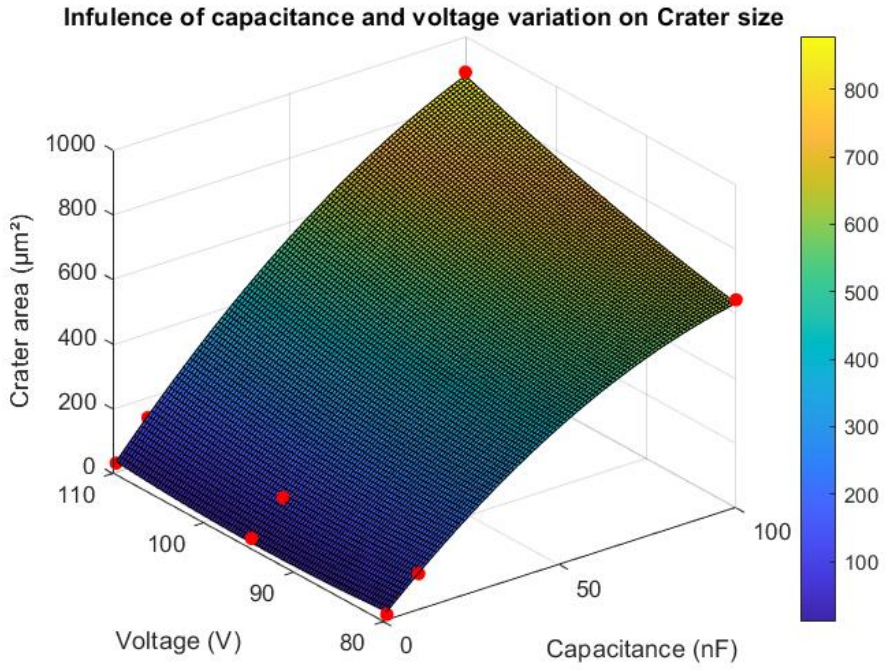

Figure 4.24: Influence of Capacitance and voltage variation on crater size for µ-WEDM of Ti-35Nb-7Zr-5Ta.

It is discerned that employing a standard significance level of 0.05, the intercept and the coefficient associated with predictor x1 (capacitance), x2 (voltage), alongside x1:x2, evince statistical significance. Conversely, the coefficients for $x1^2$ and the $x2^2$ do not exhibit statistical significance, as delineated in Table A.14. The R-squared value is computed at 0.999, signifying that approximately 99.9% of the variance observed in the crater size can be explicated by the interplay between capacitance and voltage.

4.3.3 Analysis of surface microhardness

One of the most significant parameters for assessing surface modifications produced by µ-WEDM operations is surface microhardness. The average µ-hardness of the un-machined surface is 284.39HV. The study of surface microhardness about capacitance and voltage during the micro-EDM of Ti-35Nb-7Zr-5Ta is depicted in Figure 4.25. There is a noticeable trend when the value of micro-hardness trends within this discharge energy range. This distinct pattern is observed because of the difference between consecutive voltage levels. Higher energy levels in the WEDM process indeed raise the temperature differential between the tool and the workpiece. Increased temperature causes more material to melt and anneal on the surface [71]. Due to the flushing and environment, the molten material solidifies quickly on the workpiece surface, which might alter

the mechanical properties of the machined surface. Consequently, increasing the surface micro-hardness may be attributed to this quick solidification.

Increasing capacitance from 1 to 10nF while maintaining the voltage at 80V, 95V, and 110V results in an augmentation of the microhardness of machined surfaces by factors of 1.137, 0.967, and 1.013 respectively. Similarly, with the increase in the capacitance from 10nF to 100nF at voltage levels of 80V, 95V, and 110V microhardness of the µ-WEDM treated surface augmented by 1.051, 1.018, and 1.05 times respectively. However, with an increase of voltage from 80V to 95V at capacitance levels of 1nF, 10nF, and 100nF the microhardness of the µ-WEDM treated surface increases by the factor of 1.196, 1.017, and 1.016 times respectively. Moreover, with an increase of voltage from 95V to 110V at capacitance levels of 1nF, 10nF, and 100nF the microhardness of the µ-WEDM treated surface increases by the factor of 1.018, 1.065, and 1.162 times respectively.

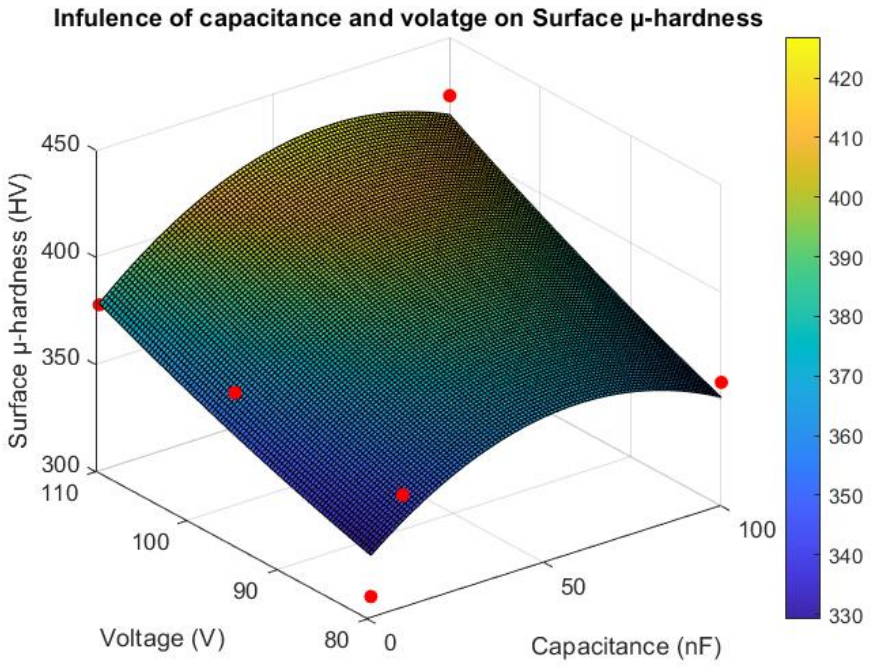

Figure 4.25: Influence of Capacitance and voltage variation on surface micro-hardness for µ-WEDM of Ti-35Nb-7Zr-5Ta.

Employing a standard significance level of 0.05, it is evident that the intercept. the coefficient corresponding to the predictor x1 (capacitance), and $x1^2$ reveals statistical significance. In contrast, the coefficients related to x2 (voltage) and the interaction terms x1:x2, $x1^2$, and $x2^2$ do not exhibit statistical significance, as shown in Table A.15. The model's R-squared value stands at 0.99, indicating that roughly 99% of the variability observed in the microhardness can be elucidated by the capacitance and voltage.

4.3.4 Analysis of surface roughness

Each spark in the µ-WEDM process removes a small quantity of material from the workpiece, resulting in the formation of minute craters. The overall material removal is the cumulative outcome of numerous successive sparks. The achieved specific surface roughness (SR) appears to be intricately connected to the morphological characteristics of these craters, which is influenced by various machining parameters (C &V). Certainly, the volume of the crater is notably influenced by the pulse energy, with higher energy levels generally resulting in larger craters [72]. Figure 4.26 depicts the 3D mapping of the machined surface of the Ti-35Nb-7Zr-5Ta. This illustration demonstrates a distinct trend: as the voltage level rises from left to right and the capacitance level rises from top to bottom.

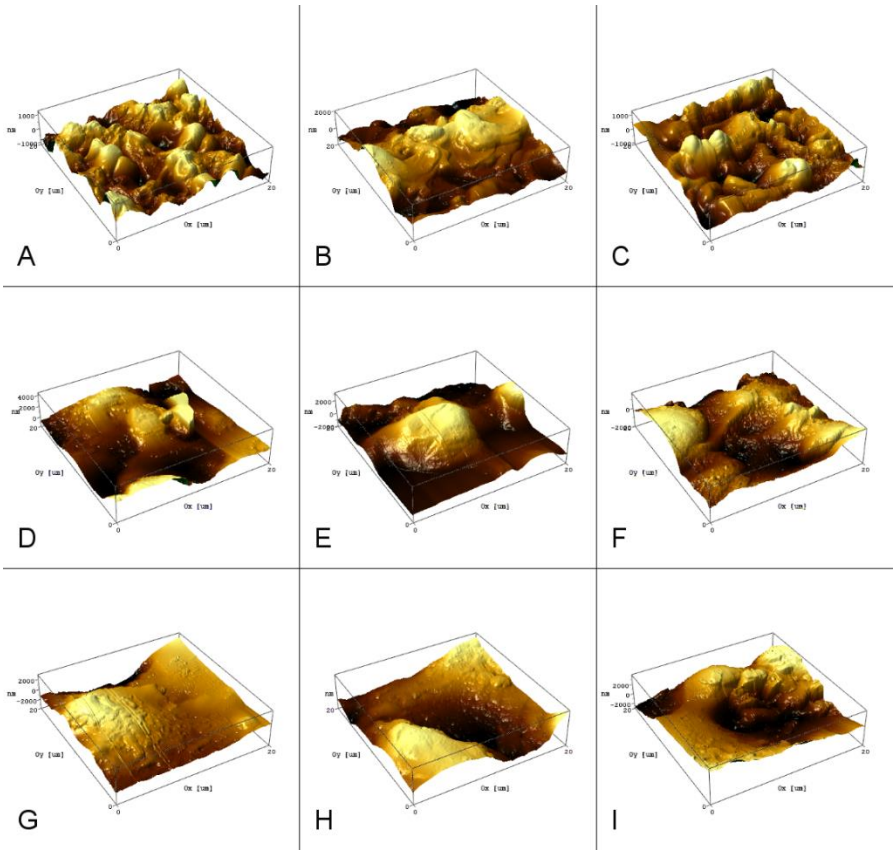

Figure 4.26: Effect of capacitance and voltage on surface roughness for µ-WEDM of Ti-35Nb-7Zr-5Ta; (A) C=10nF & V=80V, (B) C=10nF & V=105V, (C) C=10nF & V=130V, (D) C=100nF & V=80V, (E) C=100nF & V=105V, (F) C=100nF & V=130V, (G) C=400nF & V=80V, (H) C=400nF & V=105V, (I) C=400nF & V=130V.

Figure 4.27 displays the average surface roughness values at various Capacitance and voltage levels. There is a clear direct correlation between the energy level and the average surface roughness values, suggesting that surface roughness and the energy used in the EDM process are related. The surface roughness of the machined surface demonstrates an increase by factors of 1.889, 1.533, and 1.45 times respectively as capacitance rises from 1 to 10nF at voltage levels of 80V, 95V, and 110V. Similarly, with the increase in the capacitance from 10nF to 100nF at voltage

levels of 80V, 95V, and 110V the surface roughness of the µ-WEDM treated surface increased by 1.735, 1.596, and 1.876 times respectively. However, with an increase of voltage from 80V to 95V at capacitance levels of 1nF, 10nF, and 100nF the surface roughness of µ-WEDM treated surface increases by a factor of 1.402, 1.138, and 1.047 times respectively. Moreover, with an increase of voltage from 95V to 110V at capacitance levels of 10nF, 100nF, and 400nF the surface roughness of the µ-EDM treated surface increases upto 1.101, 1.042, and 1.224 times respectively.

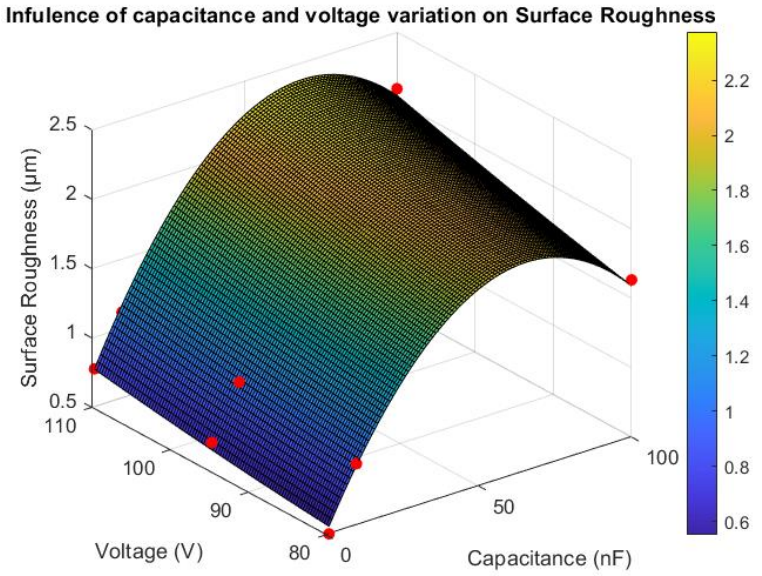

Figure 4.27: Influence of Capacitance and voltage Energy variation on surface roughness for µ-WEDM of Ti-35Nb-7Zr-5Ta.

Utilizing a standard significance level of 0.05, it becomes evident that the intercept, the coefficient corresponding to predictor x1 (capacitance), $x1^2$, and x2 (voltage) exhibit statistical significance. However, the coefficient related to $x2^2$ and interaction terms does not meet the threshold for statistical significance, as outlined in Table A.16. The R-squared value stands at 0.99, indicating that roughly 99% of the variability observed in the surface roughness can be elucidated by the interplay between capacitance and voltage.

4.3.5 EDS analysis of Ti-35Nb-7Zr-5Ta

Energy Dispersive Spectroscopy (EDS) analysis was conducted on the surface of the sample before and after machining depicted in Figure 4.28, and the elemental chemical composition of the surface was investigated. The results of the EDS analysis are presented in Table 15. As anticipated and observed, the dominant elements in the chemical composition of the machined surface are titanium, niobium, tantalum, and zirconium (TNTZ), which are the constituent components of the Ti-35Nb-7Zr-5Ta alloy. Alongside these primary components, other

elements such as carbon and oxygen are also present on the machined surface. The presence of carbon is attributed mainly to the decomposition of the dielectric fluid used during the EDM process. There is also some tungsten migration from the tool to the workpiece surface as evident from Table 4.3.

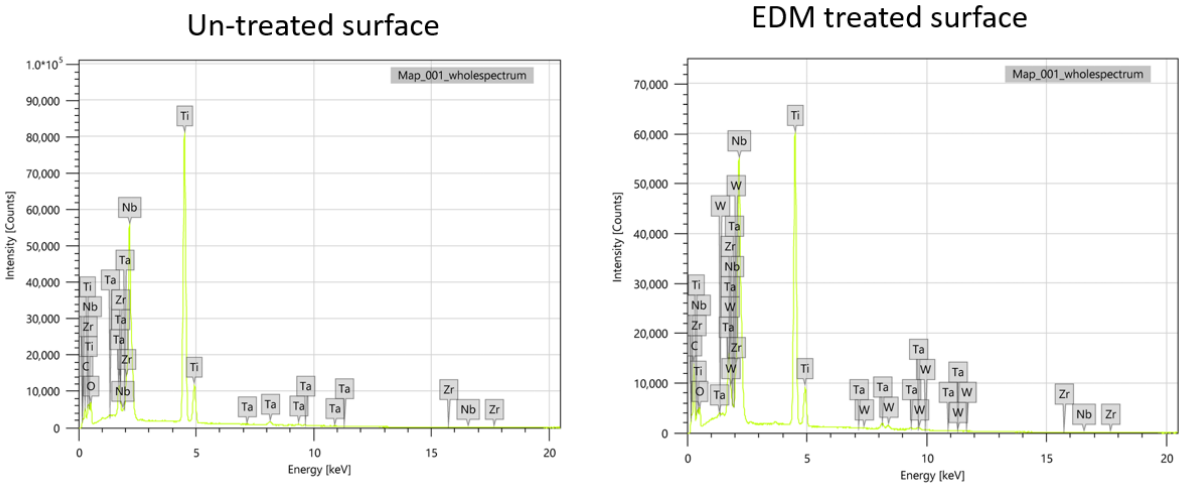

Figure 4.28: EDS analysis of Ti-35Nb-7Zr-5Ta of untreated and EDM surface.

Table 4.3 Chemical composition of Ti-35Nb-7Zr-5Ta un-treated and EDM surface.

Elements	Untreated surface		EDM surface	
	Mass%	**Atom%**	**Mass%**	**Atom%**
C	7.17±0.02	22.39±0.08	18.49±0.04	53.53±0.11
O	8.06±0.06	22.59±0.15	5.10±0.04	10.37±0.09
Ti	42.84±0.06	37.25±0.05	30.51±0.04	20.05±0.03
Zr	5.14±0.04	2.76±0.02	5.51±0.04	1.97±0.01
Nb	31.88±0.06	13.89±0.03	30.52±0.06	10.45±0.02
Ta	4.91±0.04	1.13±0.01	4.51±0.04	0.92±0.01
W	-	-	5.76±0.04	0.73±0.01
Total	**100.00**	**100.00**	**100.00**	**100.00**

4.4 Micro-WEDM of Ti-29Nb-13Ta-4.6Zr

4.4.1 Analysis of kerf width

Figure 4.29 displays the results of the measurement of the kerf width of the cuts machined on Ti-29Nb-13Ta-4.6Zr using ImageJ version 1.45d software. This figure shows how kerf width varies with capacitance horizontally keeping the voltage constant and varies with voltage vertically keeping the capacitance constant.

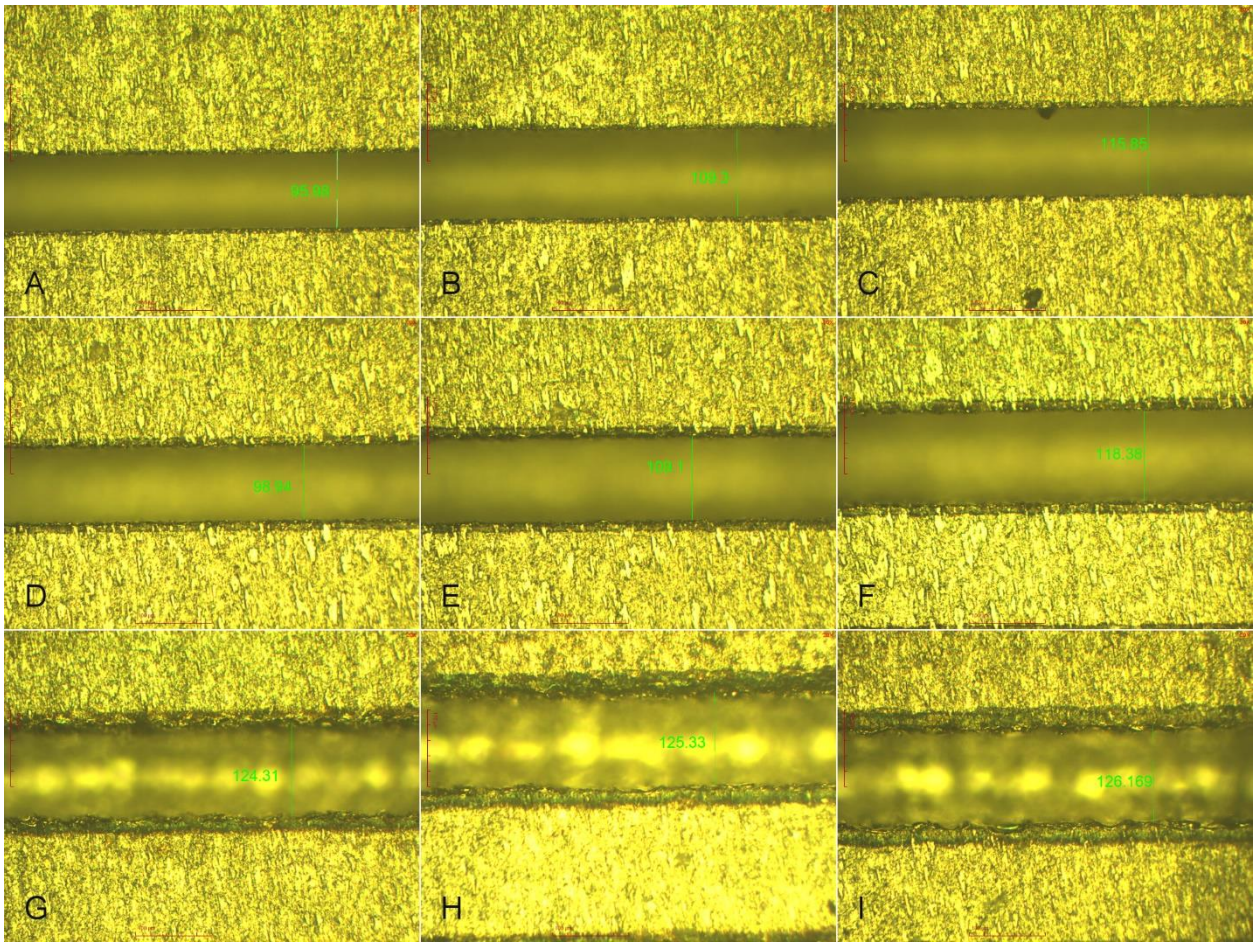

Figure 4.29: Effect of capacitance and voltage on kerf width during µ-WEDM of Ti-29Nb-13Ta-4.6Zr; (A) C=10nF & V=80V, (B) C=10nF & V=105V, (C) C=10nF & V=130V, (D) C=100nF & V=80V, (E) C=100nF & V=105V, (F) C=100nF & V=130V, (G) C=400nF & V=80V, (H) C=400nF & V=105V, (I) C=400nF & V=130V.

Figure 4.30 depicts the kerf width as it varies with the capacitance ranging from 10 to 400 nF while keeping the spindle speed constant at 1000 rpm, and positive workpiece polarity. The figure shows that kerf width exhibits a gradual and monotonically increasing trend as capacitance increases. Lower discharge energy levels cause smaller craters to form, which in turn causes less overcut because there is less material removed in each discharge. On the other hand, kerf tends to rise with larger discharge energy levels. This can also be explained by the greater span of discharge columns, which last longer than those at low energy levels.

As capacitance escalates from 1 to 10nF across voltage thresholds of 80V, 95V, and 110V, the kerf width amplifies by factors of 1.001, 1.028, and 1.029 respectively. Similarly, with the increase in the capacitance from 10nF to 100nF at voltage levels of 80V, 95V, and 110V the kerf width increases by 1.117, 1.060, and 1.140 times respectively. However, with an increase of voltage from 80V to 95V at capacitance levels of 1nF, 10nF, and 100nF the kerf width upto 1.038, 1.067, and 1.012 times respectively. Moreover, with an increase of voltage from 95V to 110V at capacitance levels of 1nF, 10nF, and 100nF the kerf width increases upto 1.033, 1.035, and 1.112 times respectively.

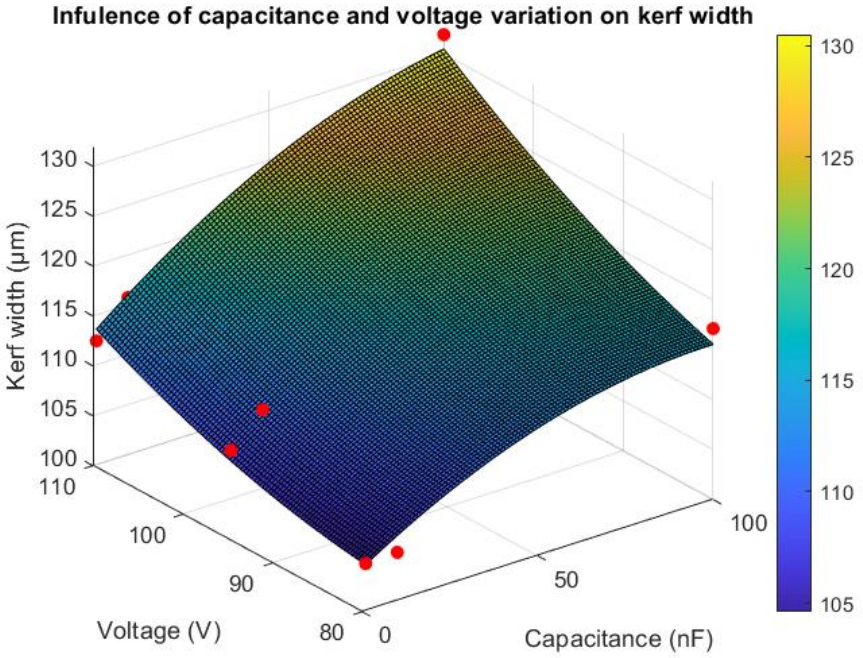

Figure 4.30: Influence of Capacitance and voltage variation on kerf width during µ-WEDM of Ti-29Nb-13Ta-4.6Zr.

It is evident that the intercept and the coefficient at a standard significance level of 0.05 pertaining to predictor x2 (voltage) demonstrate statistical significance. In contrast, the coefficients linked to x1, x1:x2, $x1^2$, and $x2^2$ do not exhibit the requisite criteria for statistical significance, as elucidated in Table A.17. The R-squared value of the model is computed to be 0.959, indicating that approximately 95.9% of the variance observed in the overcut can be ascribed to the interplay between capacitance and voltage.

4.4.2 Analysis of crater size

In an RC-type pulse generator, the material removal process is greatly influenced by the discharge energy per pulse, as it has a direct relation with capacitance and voltage [70]. Figure 38 depicts the surface topography at different capacitances and voltages, with constant wire speed. The results show that a higher capacitance causes bigger craters and a rougher surface finish at different levels of voltage. At the smallest capacitance (1nF) and voltage (80 V) as seen in Figure 4.31(A), the surface finish is finer, and it gets rougher as shown in Figure 4.31(B and C). This is because the lowest capacitance and voltage results in the lowest discharge energy. Figure 4.31(C, D, and F) illustrates that when the energy levels are high, there is a significant formation of larger craters that also exhibit more overlapping. The presence of larger-sized craters and craters overlapping typically indicates a rough surface texture.

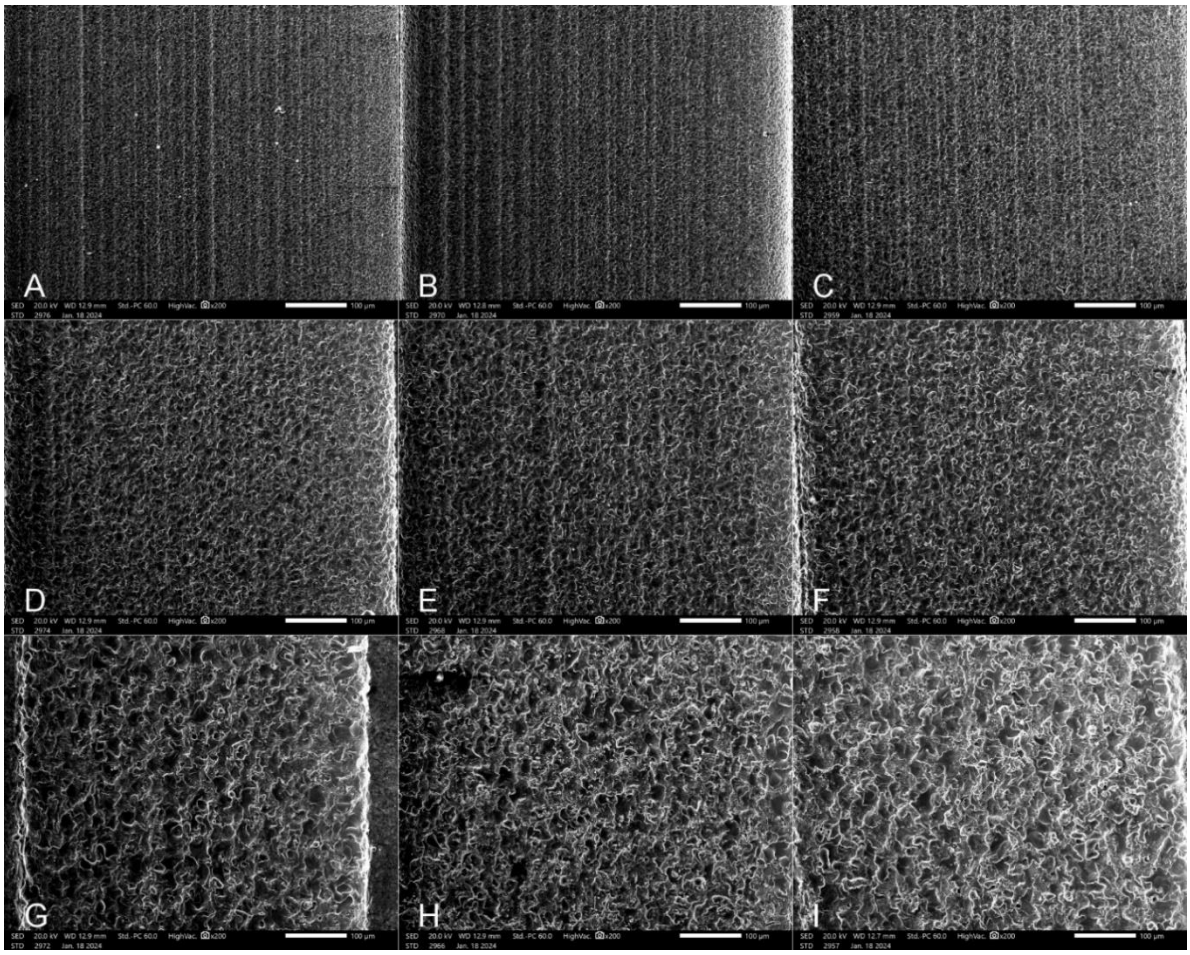

Figure 4.31: Effect of capacitance and voltage on crater size for µ-WEDM of Ti-29Nb-13Ta-4.6Zr; (A) C=10nF & V=80V, (B) C=10nF & V=105V, (C) C=10nF & V=130V, (D) C=100nF & V=80V, (E) C=100nF & V=105V, (F) C=100nF & V=130V, (G) C=400nF & V=80V, (H) C=400nF & V=105V, (I) C=400nF & V=130V.

Figure 4.32 depicts the plot of the average crater area with changes in process parameters (capacitance and voltage), the average crater size is determined using ImageJ 1.54d software. The plot depicts that the average crater size tends to rise as discharge energy per pulse increases. This phenomenon happens due to a discharge column that is comparably broader at higher energy levels [62, 63]. Higher energy tends to generate large-sized craters, so it increases the crater overlapping, surface roughness, and MRR.

Increasing capacitance from 1 to 10nF while maintaining voltage at 80V, 95V, and 110V results in an augmentation of the crater size by factors of 3.601, 3.727, and 4.176 times respectively. Similarly, with the increase in the capacitance from 10nF to 100nF at voltage levels of 80V, 95V, and 110V the crater size increases by 4.947, 4.296, and 3.718 times respectively. However, with an increase of voltage from 80V to 95V at capacitance levels of 1nF, 10nF, and 100nF the crater size increases upto 1.222, 1.264, and 1.098 times respectively. Moreover, with an increase of voltage from 95V to 110V at capacitance levels of 1nF, 10nF, and 100nF the crater size increases upto 1.153, 1.292, and 1.119 times respectively.

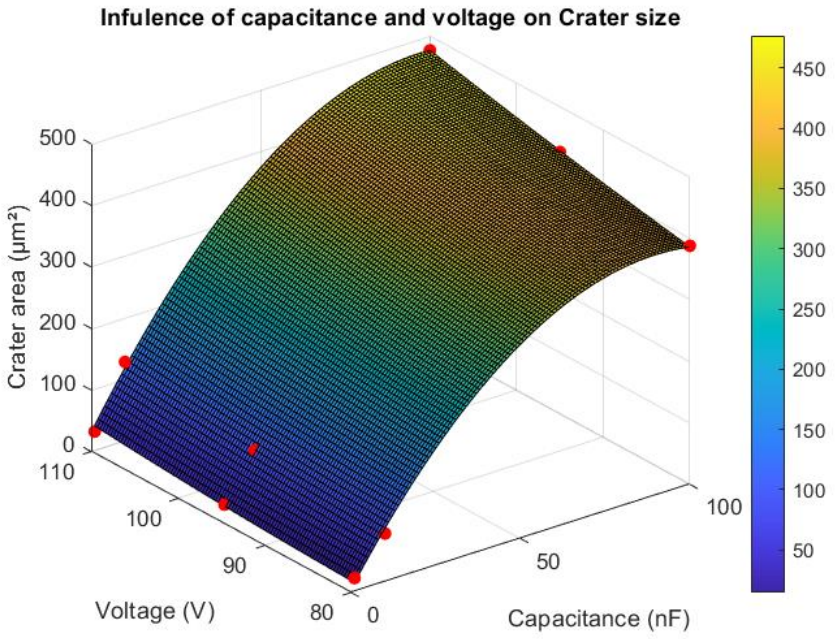

Figure 4.32: Influence of Capacitance and voltage variation on crater size for µ-WEDM of Ti-29Nb-13Ta-4.6Zr.

It is discerned that employing a standard significance level of 0.05, the intercept and the coefficient associated with predictor x1 (capacitance), x2 (voltage), $x1^2$, alongside x1:x2, evince statistical significance. Conversely, the coefficients for $x2^2$ do not exhibit statistical significance, as delineated in Table A.18. The R-squared value is computed at 0.999, signifying that approximately 99.9% of the variance observed in the crater size can be explicated by the interplay between capacitance and voltage.

4.4.3 4.4.3 Analysis of surface microhardness

One of the most significant parameters for assessing surface modifications produced by µ-WEDM operations is surface microhardness. The average µ-hardness of the un-machined surface is 284.39HV. The study of surface microhardness about capacitance and voltage during the micro-EDM of Ti-29Nb-13Ta-4.6Zr is depicted in Figure 4.33. There is a noticeable trend when the value of micro-hardness trends within this discharge energy range. This distinct pattern is observed because of the difference between consecutive voltage levels. Higher energy levels in the WEDM process indeed raise the temperature differential between the tool and the workpiece. Increased temperature causes more material to melt and anneal on the surface [71]. Due to the flushing and environment, the molten material solidifies quickly on the workpiece surface, which might alter the mechanical properties of the machined surface. Consequently, increasing the surface micro-hardness may be attributed to this quick solidification.

Increasing capacitance from 1 to 10nF while maintaining the voltage at 80V, 95V, and 110V results in an augmentation of the microhardness of machined surfaces by factors of 2.825, 1.019,

and 1.02 respectively. Similarly, with the increase in the capacitance from 10nF to 100nF at voltage levels of 80V, 95V, and 110V, the microhardness of the µ-WEDM treated surface augmented by 1.046, 1.0693, and 1.023 times respectively. However, with an increase of voltage from 80V to 95V at capacitance levels of 1nF, 10nF, and 100nF the microhardness of the µ-WEDM treated surface increases by the factor of 1.102, 1.011, and 1.034 times respectively. Moreover, with an increase of voltage from 95V to 110V at capacitance levels of 1nF, 10nF, and 100nF the microhardness of the µ-WEDM treated surface increases by the factor of 1.023, 1.067, and 1.005 times respectively.

Employing a standard significance level of 0.05, it is evident that the intercept. the coefficient corresponding to the predictor x1 (capacitance), and $x1^2$ reveals statistical significance. In contrast, the coefficients related to x2 (voltage) and the interaction terms x1:x2, and $x2^2$ do not exhibit statistical significance, as shown in Table A.19. The model's R-squared value stands at 0.991, indicating that roughly 99.1% of the variability observed in the microhardness can be elucidated by the capacitance and voltage.

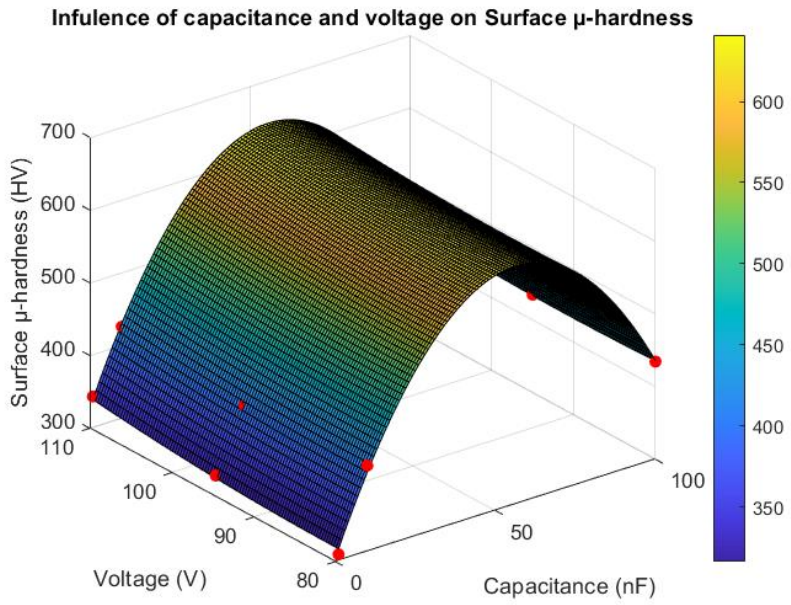

Figure 4.33: Influence of Capacitance and voltage variation on surface micro-hardness for µ-EDM of Ti-29Nb-13Ta-4.6Zr.

4.4.4 Analysis of surface roughness

Each spark in the µ-WEDM process removes a small quantity of material from the workpiece, resulting in the formation of minute craters. The overall material removal is the cumulative outcome of numerous successive sparks. The achieved specific surface roughness (SR) appears to be intricately connected to the morphological characteristics of these craters, which is influenced by various machining parameters (C &V). Certainly, the volume of the crater is notably

influenced by the pulse energy, with higher energy levels generally resulting in larger craters [72]. Figure 4.34 depicts the 3D mapping of the machined surface of the Ti-29Nb-13Ta-4.6Zr. This illustration demonstrates a distinct trend: as the voltage level rises from left to right and the capacitance level rises from top to bottom.

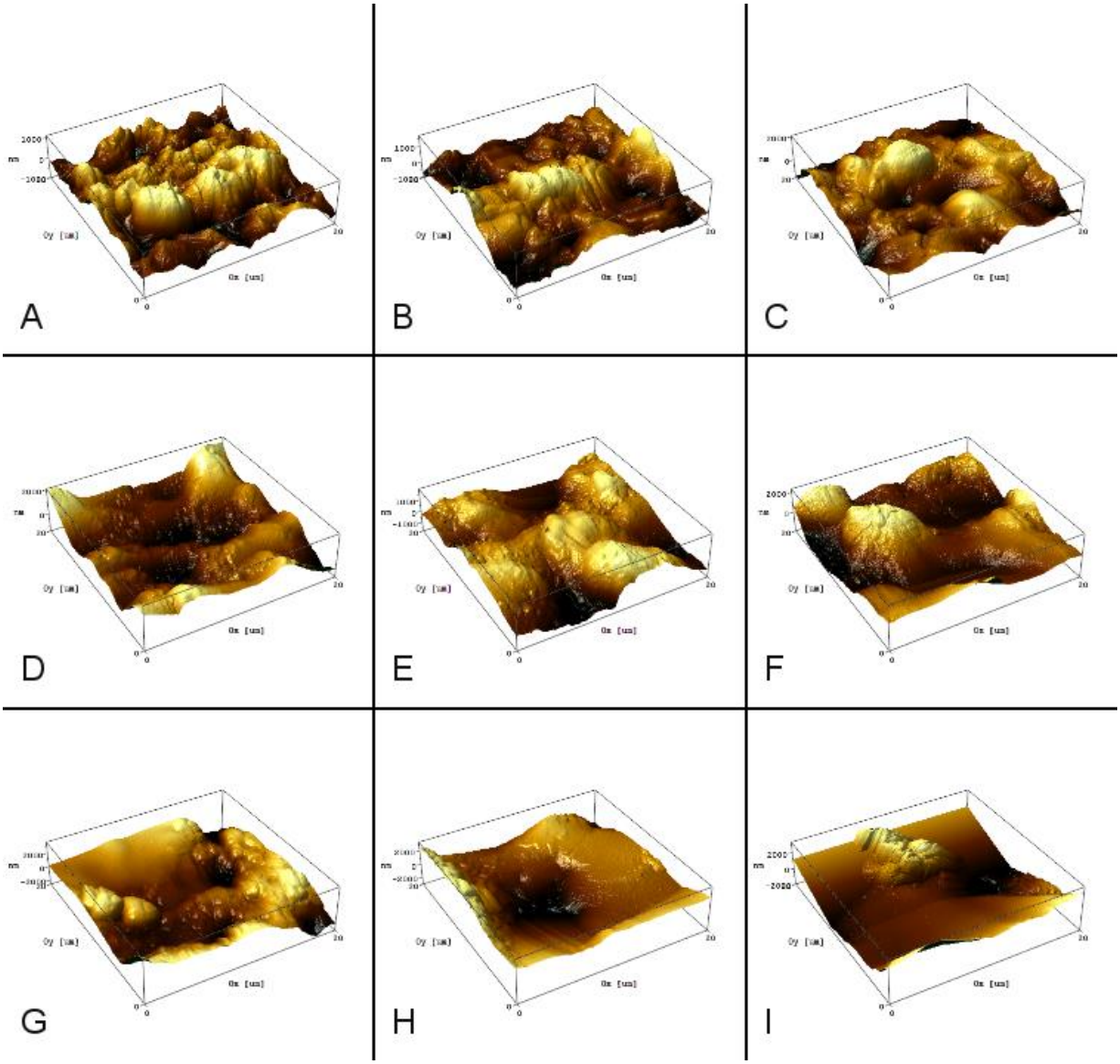

Figure 4.34: Effect of capacitance and voltage on surface roughness for μ-WEDM of Ti-29Nb-13Ta-4.6Zr; (A) C=10nF & V=80V, (B) C=10nF & V=105V, (C) C=10nF & V=130V, (D) C=100nF & V=80V, (E) C=100nF & V=105V, (F) C=100nF & V=130V, (G) C=400nF & V=80V, (H) C=400nF & V=105V, (I) C=400nF & V=130V.

Figure 4.35 displays the average surface roughness values at various Capacitance and voltage levels. There is a clear direct correlation between the energy level and the average surface roughness values, suggesting that surface roughness and the energy used in the EDM process are related. The surface roughness of the machined surface demonstrates an increase by factors of 2.825, 2.102, and 1.74 times respectively as capacitance rises from 1 to 10nF at voltage levels of 80V, 95V, and 110V. Similarly, with the increase in the capacitance from 10nF to 100nF at voltage

levels of 80V, 95V, and 110V the surface roughness of the µ-WEDM treated surface increased by 1.198, 1.486, and 1.579 times respectively. However, with an increase of voltage from 80V to 95V at capacitance levels of 1nF, 10nF, and 100nF the surface roughness of µ-WEDM treated surface increases by a factor of 1.376, 1.023, and 1.269 times respectively. Moreover, with an increase of voltage from 95V to 110V at capacitance levels of 10nF, 100nF, and 400nF the surface roughness of the µ-EDM treated surface increases upto 1.304, 1.079, and 1.146 times respectively.

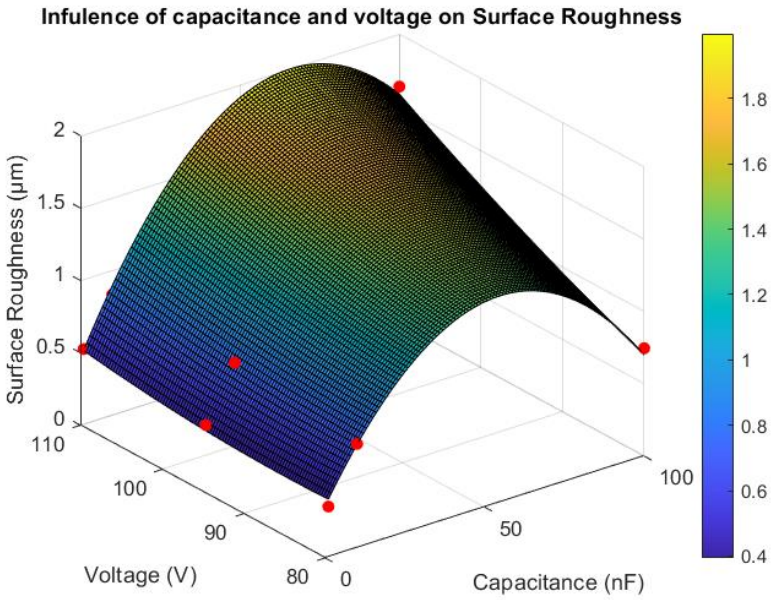

Figure 4.35: Influence of Capacitance and voltage Energy variation on surface roughness for µ-EDM of Ti-29Nb-13Ta-4.6Zr.

Utilizing a standard significance level of 0.05, it becomes evident that the intercept, the coefficient corresponding to predictor x1 (capacitance), $x1^2$, and x2 (voltage) exhibit statistical significance. However, the coefficient related to $x2^2$ and interaction terms does not meet the threshold for statistical significance, as outlined in Table A.20. The R-squared value stands at 0.99, indicating that roughly 99% of the variability observed in the surface roughness can be elucidated by the interplay between capacitance and voltage.

4.4.5 EDS analysis of Ti-29Nb-13Ta-4.6Zr

Energy Dispersive Spectroscopy (EDS) analysis was conducted on the surface of the sample before and after machining depicted in Figure 43, and the elemental chemical composition of the surface was investigated. The results of the EDS analysis are presented in Table 5. As anticipated and observed, the dominant elements in the chemical composition of the machined surface are titanium, niobium, tantalum, and zirconium (TNTZ), which are the constituent components of the Ti-29Nb-13Ta-4.6Zr alloy. Alongside these primary components, other elements such as carbon and oxygen are also present on the machined surface. The presence of

carbon is attributed mainly to the decomposition of the dielectric fluid used during the EDM process. There is also some tungsten migration from the tool to the workpiece surface as evident from Table 16.

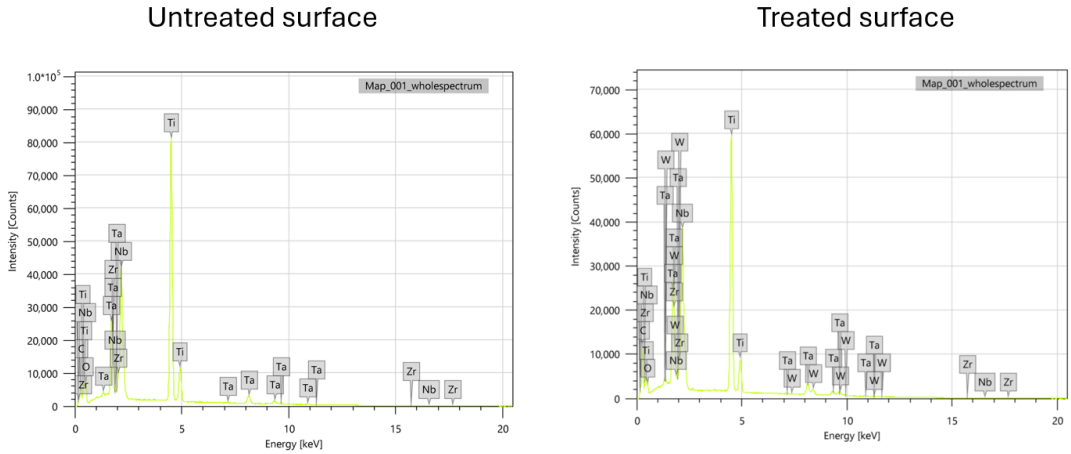

Figure 4.36: EDS analysis of Ti-29Nb-13Ta-4.6Zr of untreated and EDM surface.

Table 4.4 Chemical composition of Ti-29Nb-13Ta-4.6Zr un-treated and EDM surface.

Elements	Untreated surface		EDM surface	
	Mass%	**Atom%**	**Mass%**	**Atom%**
C	5.12±0.02	22.44±0.08	11.72±0.04	55.06±0.12
O	9.27±0.05	23.92±0.14	3.26±0.03	5.26±0.07
Ti	46.67±0.05	37.10±0.05	35.13±0.05	24.25±0.04
Zr	3.78±0.04	1.77±0.02	3.34±0.04	1.41±0.02
Nb	25.74±0.06	11.36±0.03	24.96±0.06	9.61±0.02
Ta	12.52±0.04	3.42±0.01	12.49±0.05	2.58±0.01
W	-	-	9.02±0.06	1.83±0.01
Total	**100.00**	**100.00**	**100.00**	**100.00**

4.4.6 Antibacterial test

The test aimed to investigate the effect of numerous energy levelled WEDM T-29Nb-13Ta-4.6Zr alloys against commonly encountered bacteria strains in healthcare-associated infections, which are Staphylococcus aureus and Escherichia coli, as well as opportunistic pathogen Pseudomonas aeruginosa. Bacillus subtilis will be used as a control, which is a nonpathogenic bacterial strain frequently found in soil and the gastrointestinal tracts of ruminants, humans, and marine sponges. The bacterial biofilm formation was assessed using the crystal violet staining method after incubation of machined and unmachined surfaces of the WEDM T-29 alloy with bacterial in culture broth for 72 h.

Figure 4.37 depicts the characteristic images of crystal violet stained, bright field, and detected biofilm developed by four different bacteria strains on a micro-EDM treated WEDM Ti-29Nb-13Ta-4.6 alloy surface at three different discharge energy level. The effects of discharge energy level on the amount of biofilm formed on the alloy for all bacterial strains are shown in Figure 4.38. It is worth noting that P. aeruginosa and E. coli showed minimal attachment toward high-energy treated alloy surfaces, and the amount of biofilm developed are less than 3% of the total surface area. Figure 4.38 further illustrates that different WEDM Ti-29Nb-13Ta-4.6Zr alloy surfaces have varying propensities of attraction to different bacterial species. For example, Figure 4.38 clearly indicates that the proportion of biofilm coverage for S. aureus are minimum at low discharge energy level while it is much higher at medium and high discharge energy. Overall, our results seem to suggest that treating the WEDM Ti-29Nb-13Ta-4.6 alloy surface with low discharge energy setting will minimize the formation of biofilm induced by all four selected strains of bacterial.

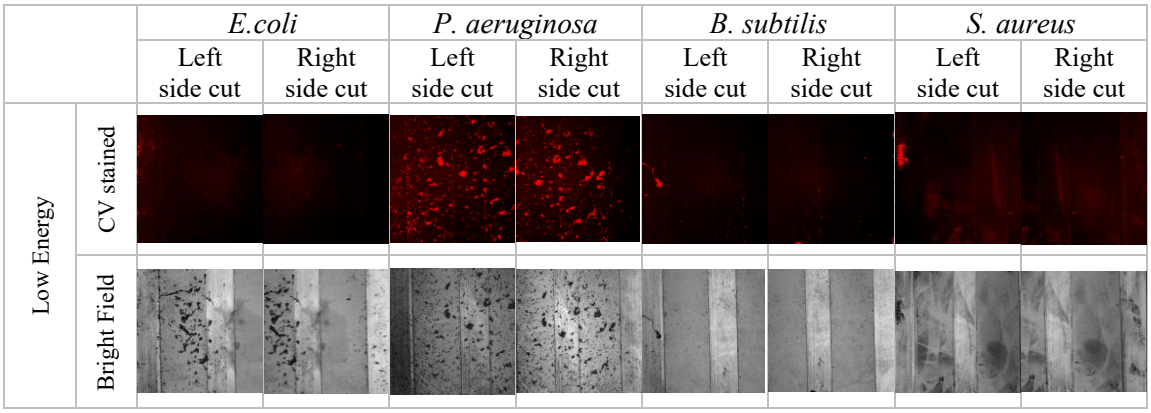

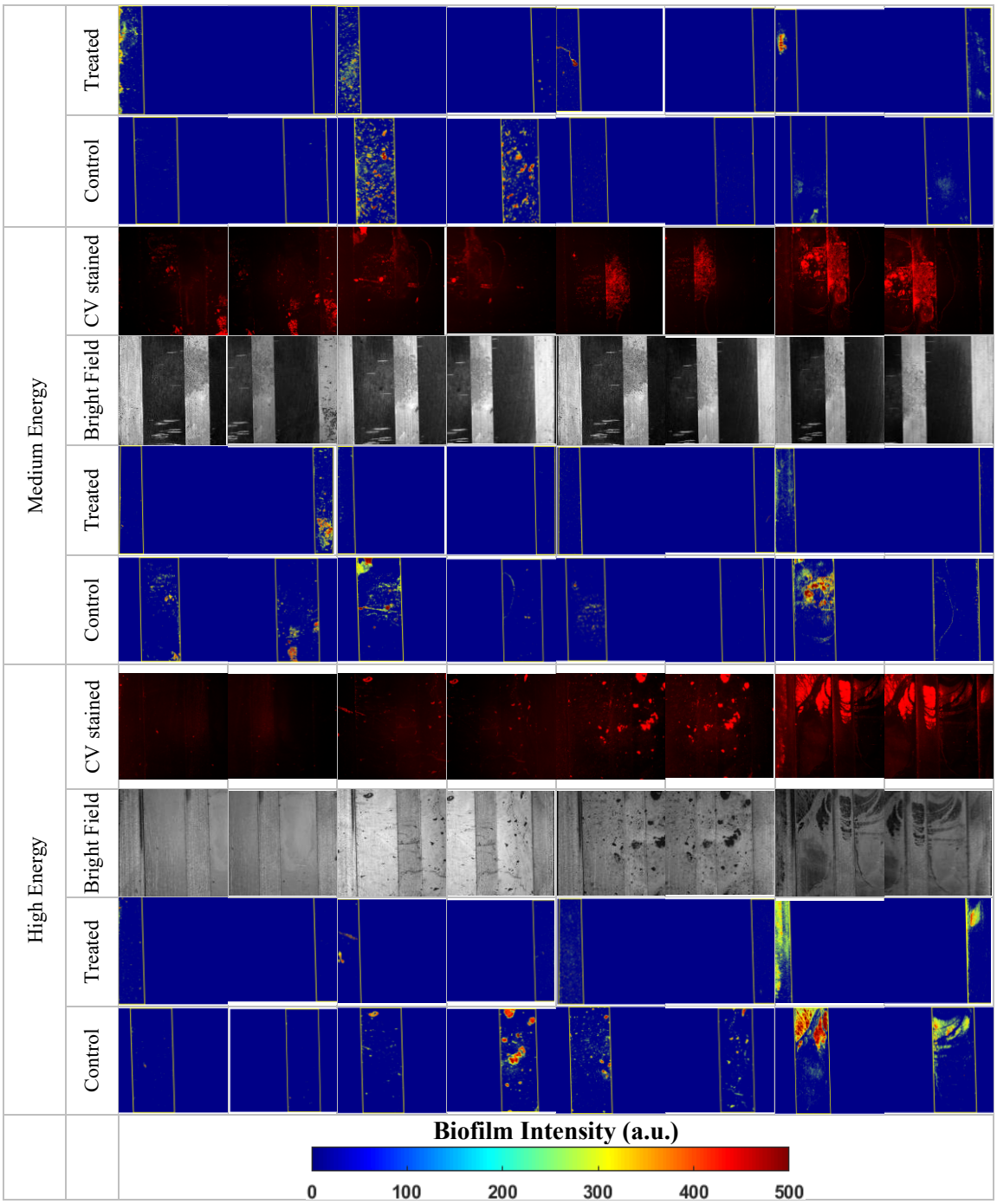

Figure 4.37: Representative images of Crystal Violet stained, bright field and biofilms detection for B. subtilis, E. coli, P. aeruginosa and S. aureus on machined WEDM T-29 alloy with numerous energy levels. Yellow box indicates the metrology of the proportion of biofilm formed on the surface was done in the machined area.

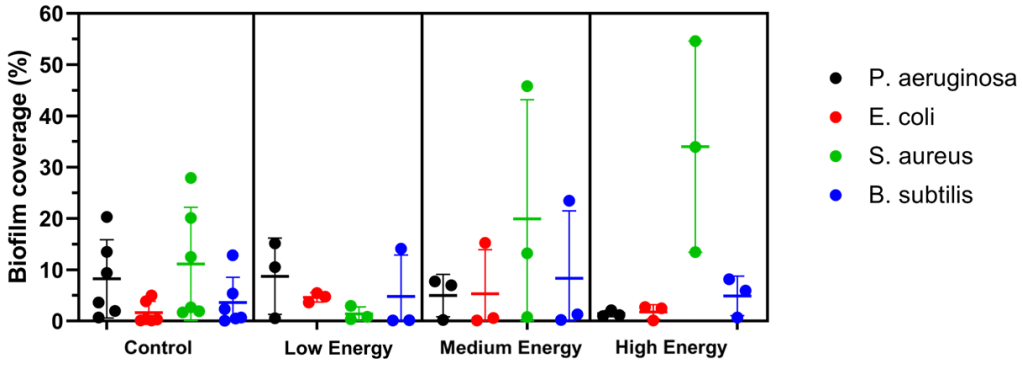

Figure 4.38: Quantification of biofilm coverage for all bacterial strains across all three different energy levels.

4.5 Numerical modeling for crater and its validation

The real volume of the crater developed during the µ-EDM process is impacted by the inefficiency of flushing molten material with the dielectric fluid. Plasma Flushing Efficiency is the ratio of numerical to experimental crater volumes (PFE). The volume of the crater during µ-EDM machining is assumed to be hemispherical [73]. The amount of metal removed in this case is equal to the volume of the crater that was made on the surface of the workpiece, as determined by the following equation:

$$PFE\% = \frac{V_{Experimental}}{V_{Numerical}} = \left(\frac{D_{EXP}}{D_{NUM}}\right)^3 \quad (4.1)$$

Where D_{EXP} and D_{NUM} represent the diameter of the crater from experimental and numerical results respectively. Figure 4.39 depicts the Scanning Electron Microscope (SEM) image of the µ-EDM machined surface measured by SEM JEOL JSM-IT200(LA). Figure 4.39 A, B, and C show the crater size at capacitance levels 1nF, 10nF, and 100nF respectively, however, the voltage was 80V. The craters were measured by using ImageJ software 1.54d. While Figure 4.40 represents the crater size developed by using thermal analysis on COMSOL on different levels of energy. Moreover, the domain size of Figure 4.40 A, B, and C are 20µm x 20µm, 30µm x 30µm, and 40µm x 40µm respectively.

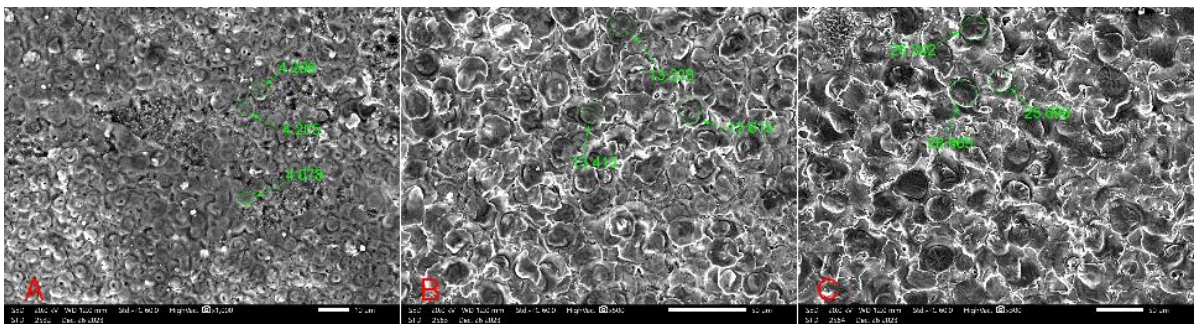

Figure 4.39: SEM Image of micro-EDM machined surface at (A) C=1nF & V=80V, (B) C=10nF & V=80V, and (C) C=100nF & V=80V.

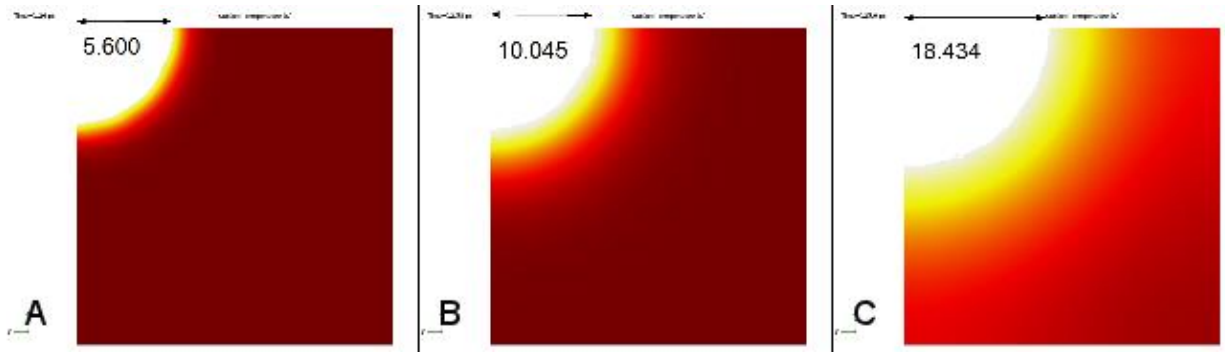

Figure 4.40: Numerical results of crater size at (A) C=1nF & V=80V, (B) C=10nF & V=80V, and (C) C=100nF & V=80V.

4.5.1 Regression model

Regression analysis was performed by using Minitab software is an efficient approach. In this process, both experimental and numerical crater sizes obtained from ImageJ software are recorded in Table 4.5. Averaging the crater sizes from experimental results (as shown in Figure 4.39) aids in minimizing errors within the dataset. Additionally, equation (4.1) facilitates the determination of Plasma Flushing Efficiency (PFE%).

Table 4.5: Numerical and experimental values of crater size employed for the regression model.

Capacitance (nF)	Voltage (V)	D_{EXP} (µm)	D_{NUM} (µm)	PFE%
1.00E-09	80	4.193	11.2	5.247114
1.00E-09	90	5.412	12.018	9.132228
1.00E-09	100	5.667667	12.604	9.092592
1.00E-09	110	5.91	13.364	8.648744
1.00E-08	80	13.41933	20.09	29.80252
1.00E-08	90	13.68733	21.816	24.69626
1.00E-08	100	13.87567	23.704	20.05842
1.00E-08	110	14.73667	24.436	21.93347
1.00E-07	80	26.901	36.868	38.84692
1.00E-07	90	30.12667	41.206	39.08156
1.00E-07	100	31.78733	47.24	30.46721
1.00E-07	110	33.48467	52.892	25.37278

Equations (4.2) establish the relationship between PFE% in relation to the capacitance and voltage, derived through polynomial regression modeling. These equations highlight the variability in the portion of heat allocated to the anode within the plasma channel. It is evident that this distribution ratio actually varies with changes in capacitance and voltage.

$$PFE\% = -8.3 + 2401985886 * C + 0.37 * V - 17015211618467900 * C^2 - 0.00223 * V^2 - 4492244 * C * V \quad (4.2)$$

Based on equation (4.2) it became easier to predict the crater size for different level of energy. Additionally, the surface plot of PFE% is illustrated in Figure 4.39.

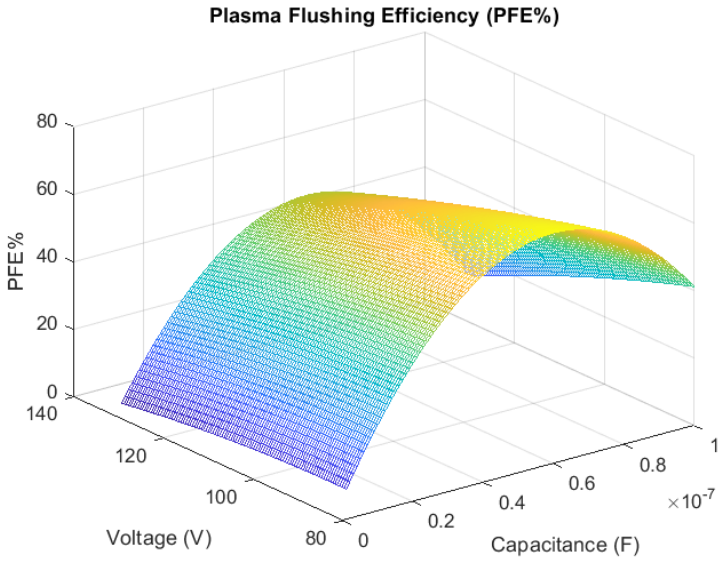

Figure 4.41: Surface plot of plasma flushing efficiency.

4.5.2 Model validation

The ongoing work has focused on a thermal distribution model within the workpiece during each discharge, in addition to establishing correlations between process input parameters and plasma flushing efficiency via regression modeling. Based on the analysis in section 4.51 the equation (3.9) can be expressed as:

$$q_o = 4.5\left(\frac{PFE * E}{t_d * \pi * R^2}\right) \tag{4.3}$$

To assess the accuracy of the model, 12 numerical simulations were performed for different settings of energy. These results, compared with the experimental value of crater size for identical process settings, are detailed in Table 4.6.

Table 4.6: Comparison between experimental and numerical values for crater size.

Capacitance (nF)	Voltage (V)	D_{EXP} (µm)	D_{NUM} (µm)	Error%
1.00E-09	85	5.246333	4.686	10.68048
1.00E-09	95	5.513667	5.248	4.81833
1.00E-09	105	5.707667	5.51	3.463178
1.00E-09	115	6.241333	5.4	13.48003
1.00E-08	85	13.47233	11.04	18.05428
1.00E-08	95	13.809	11.964	13.36085
1.00E-08	105	14.66833	13.132	10.47381
1.00E-08	115	15.256	13.776	9.701101
1.00E-07	85	29.454	24.202	17.83119
1.00E-07	95	31.36167	25.778	17.80411
1.00E-07	105	32.149	27.022	15.94762
1.00E-07	115	33.87733	27.886	17.68537

The comparisons presented in Table 4.6 indicate a consistent alignment between crater diameter values predicted by the numerical model and the experimental outcomes across all discharge conditions.

Chapter 5: Optimization of machining parameters

This chapter presents the optimization of findings from experimental studies for µ-EDM and µ-WEDM of Ti-35Nb-7Zr-5Ta and Ti-29Nb-13Ta-4.6Zr. This section includes the optimaization of parameters using Grey Relation Grade analysis.

5.1 Optimization of Micro-EDM response parameters

5.1.1 Material removal rate (MRR)

From Figure 5.1 and 5.2 shows the S/N response of material removal rate for Ti-35Nb-7Zr-5Ta and Ti-29Nb-13Ta-4.6Zr respectively, it is evident that Material Removal Rate (MRR) increases with higher values of capacitance and gap voltage. However, the higher variances of the mean values of the Signal-to-Noise (S/N) ratios for capacitance have a greater impact compared to voltage. By applying the "larger-is-better" criteria to Taguchi's orthogonal array. Equation 5.1 and 5.2 presents the regression equation for average MRR for Ti-35Nb-7Zr-5Ta and Ti-29Nb-13Ta-4.6Zr respectively. Where C_10, C_100, and C_400 represents the capacitance 10nF, 100nF, and 400nF respectively, in addition, V_80,V_105, and V_130 represents the voltage level of 80V, 105V, and 130V respectively.

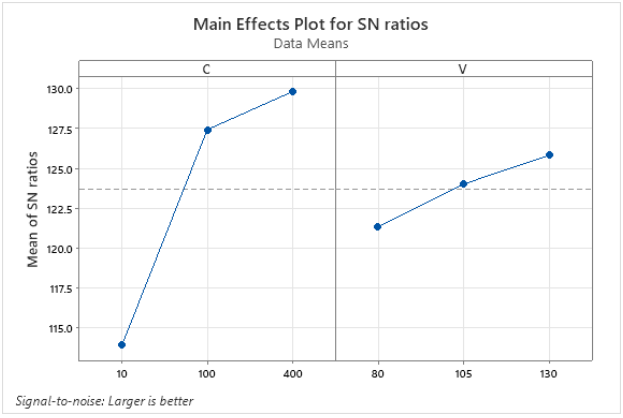

Figure 5.1: S/N response for MRR for µ-EDM for Ti-35Nb-7Zr-5Ta.

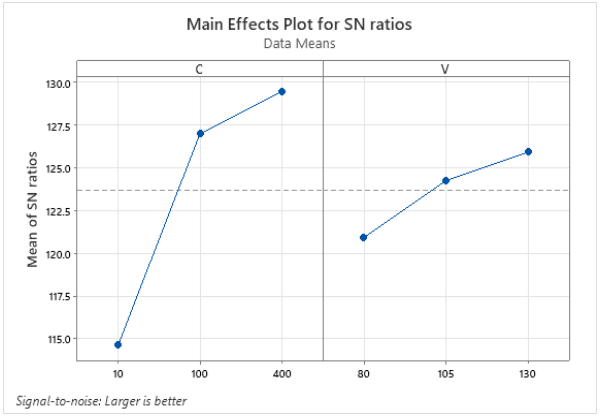

Figure 5.2: S/N response for MRR for µ-EDM for Ti-29Nb-13Ta-4.6Zr.

Regression equation:

$$\begin{aligned}\textbf{MRR} = {} & 2016205 - 1480788\ C\_10 + \\ & 379314\ C\_100 + 1101475 \\ & C\_400 - 283825\ V\_80 - 70670 \\ & V\_105 \\ & + 354495\ V\_130\end{aligned} \quad (5.1)$$

Regression equation:

$$\begin{aligned}\textbf{MRR} = {} & 1964136 - 1404167\ C\_10 \\ & + 361898\ C\_100 \\ & + 1042268\ C\_400 - \\ & 511901\ V\_80 + 60357\ V\_105 \\ & + 451543\ V\_130\end{aligned} \quad (5.2)$$

5.1.2 Overcut

From Figure 5.3 and 5.4 displays the S/N response of overcut for Ti-35Nb-7Zr-5Ta and Ti-29Nb-13Ta-4.6Zr respectively, it is evident that overcut of µ-holes increases with higher values of capacitance and gap voltage. However, the higher variances of the mean values of the Signal-to-

Noise (S/N) ratios for capacitance have a greater impact compared to voltage. By applying the "smaller-is-better" criteria to Taguchi's orthogonal array. Equation 5.3 and 5.4 presents the regression equation for average overcut for Ti-35Nb-7Zr-5Ta and Ti-29Nb-13Ta-4.6Zr respectively.

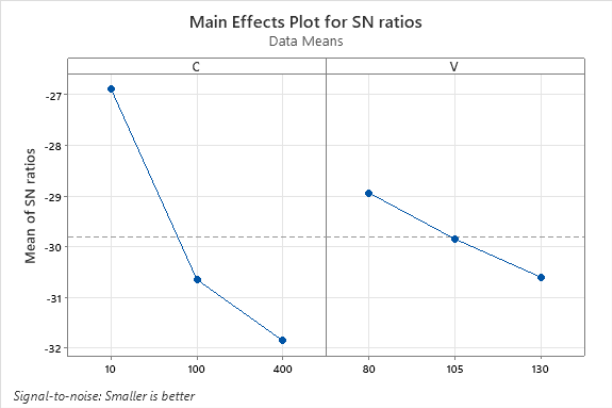

Figure 5.3: S/N response for overcut for µ-EDM for Ti-35Nb-7Zr-5Ta.

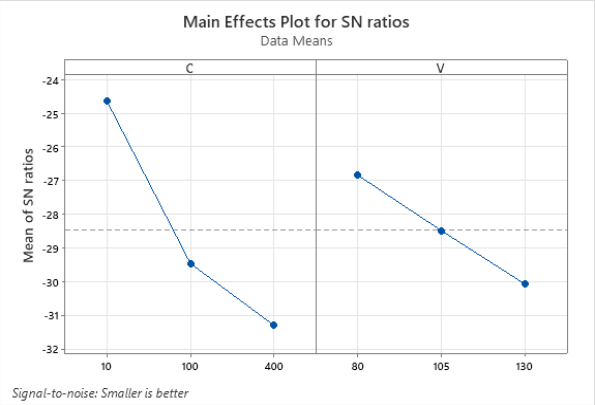

Figure 5.4: S/N response for overcut for µ-EDM for Ti-29Nb-13Ta-4.6Zr.

Regression equation:

$$\textbf{Overcut} = 31.889 - 9.752\ C\_10 + 2.341\ C\_100 + 7.410\ C\_400 - 3.160\ V\_80 - 0.005\ V\_105 + 3.165\ V\_130 \quad (5.3)$$

Regression equation:

$$\textbf{Overcut} = 28.197 - 10.94\ C\_10 + 1.83\ C\_100 + 9.12\ C\_400 - 5.34\ V\_80 + 0.17\ V\_105 + 5.17\ V\_130 \quad (5.4)$$

5.1.3 Crater size

From Figures 5.5 and 5.6, it is observed that the Signal-to-Noise (S/N) response of crater size for Ti-35Nb-7Zr-5Ta and Ti-29Nb-13Ta-4.6Zr respectively showcases an increase in the crater size during µ-EDM of µ-holes with higher values of capacitance and gap voltage. Nonetheless, the higher variances of the mean values of the S/N ratios for capacitance exert a more pronounced impact compared to voltage. By employing the "smaller-is-better" criteria to Taguchi's orthogonal array, Equations 5.5 and 5.6 present the regression equations for the average crater size for Ti-35Nb-7Zr-5Ta and Ti-29Nb-13Ta-4.6Zr respectively.

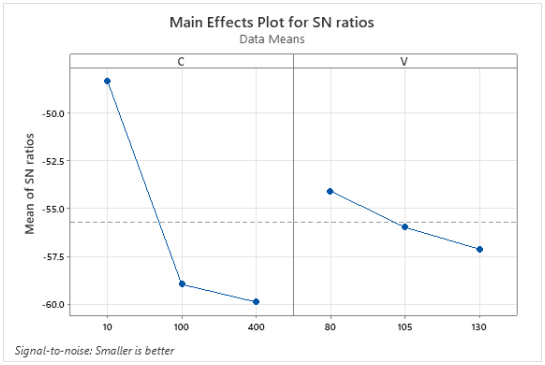

Figure 5.5: S/N response for crater size for µ-EDM for Ti-35Nb-7Zr-5Ta.

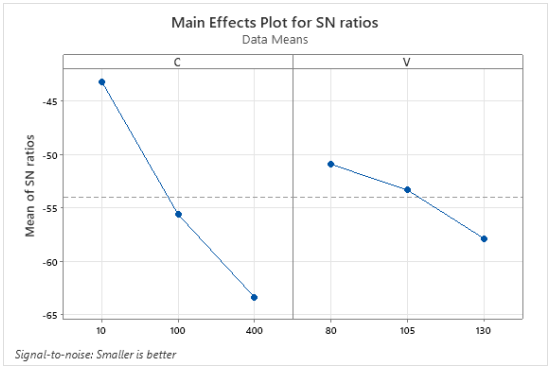

Figure 5.6: S/N response for overcut for µ-EDM for Ti-29Nb-13Ta-4.6Zr.

Regression equation:

$$\textbf{Crater size} = 718.2 - 448.6\ C\_10 + 171.5\ C\_100 + 277.1\ C\_400 - 93.9\ V\_80 + 1.1\ V\_105 + 92.8\ V\_130 \quad (5.5)$$

Regression equation:

$$\textbf{Crater size} = 776.3 - 621\ C\_10 - 135\ C\_100 + 756\ C\_400 - 237\ V\_80 - 90\ V\_105 + 328\ V\_130 \quad (5.6)$$

5.1.4 5.1.4 Circularity

The S/N response of circularity of µ-holes for Ti-35Nb-7Zr-5Ta and Ti-29Nb-13Ta-4.6Zr depicted in Figures 5.7 and 5.8 respectively illustrates a decrease in the circularity of µ-holes with higher capacitance and gap voltage values. However, it is noteworthy that the higher variances of the mean values of the Signal-to-Noise (S/N) ratios for capacitance exert a more substantial influence compared to voltage. By applying Taguchi's orthogonal array with the "larger-is-better" criteria, Equations 16 and 17 present the regression equations for the average circularity of µ-holes for Ti-35Nb-7Zr-5Ta and Ti-29Nb-13Ta-4.6Zr respectively.

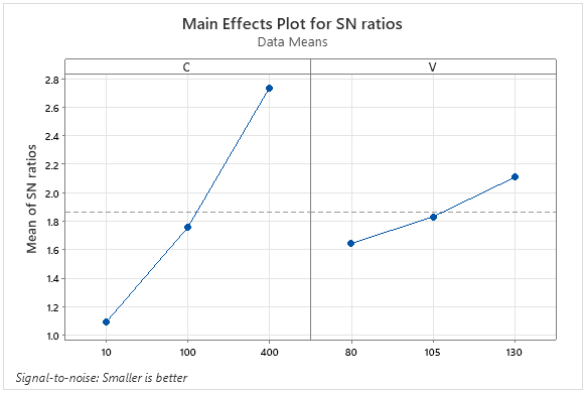

Figure 5.7: S/N response of circularity for µ-EDM for Ti-35Nb-7Zr-5Ta.

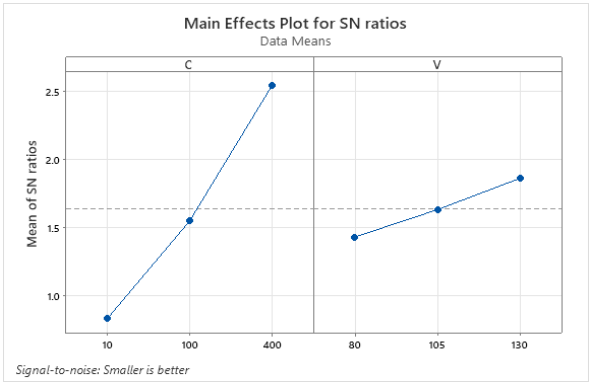

Figure 5.8: S/N response of circularity for µ-EDM for Ti-29Nb-13Ta-4.6Zr.

Regression equation:

$$\textbf{Circularity} = 0.80990 + 0.07271\ C\_10 + 0.00738\ C\_100 - 0.08009\ C\_400 + 0.02116\ V\_80 + 0.00278\ V\_105 - 0.02394\ V\_130 \quad (5.7)$$

Regression equation:

$$\textbf{Circularity} = 0.83078 + 0.07856\ C\_10 + 0.00622\ C\_100 - 0.08478\ C\_400 + 0.02089\ V\_80 + 0.00056\ V\_105 - 0.02144\ V\_130 \quad (5.8)$$

5.1.5 5.1.5 Microhardness

Analysis of Figures 5.9 and 5.10 reveals that the S/N response of surface microhardness for Ti-35Nb-7Zr-5Ta and Ti-29Nb-13Ta-4.6Zr respectively indicates an escalation in the microhardness with increased capacitance and gap voltage values. However, it is notable that the higher variances of the mean values of the Signal-to-Noise (S/N) ratios for voltage have a more effect compared to capacitance. Employing Taguchi's orthogonal array with the "Higher-is-better" criteria, Equations 5.9 and 5.10 provide the regression equations for the average surface microhardness for Ti-35Nb-7Zr-5Ta and Ti-29Nb-13Ta-4.6Zr respectively.

Figure 5.9: S/N response of microhardness for µ-EDM for Ti-35Nb-7Zr-5Ta.

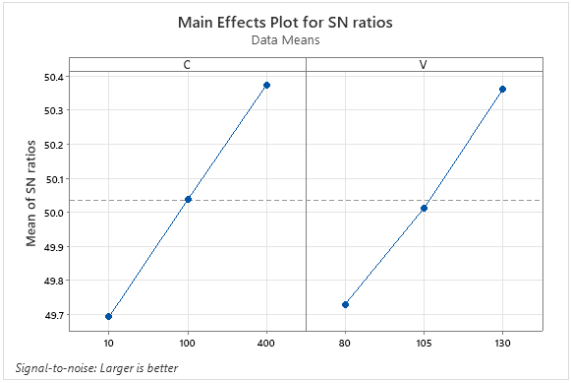

Figure 5.10: S/N response of microhardness for µ-EDM for Ti-29Nb-13Ta-4.6Zr.

Regression equation:

$$\text{Micro-hardness} = 329.65 - 11.26\ C\_10 - 0.04\ C\_100 + 15.30\ C\_400 - 8.93\ V\_80 - 0.93\ V\_105 + 14.85\ V\_130 \quad (5.9)$$

Regression equation:

$$\text{Micro-hardness} = 317.81 - 12.26\ C\_10 - 0.04\ C\_100 + 12.30\ C\_400 - 10.93\ V\_80 - 0.93\ V\_105 + 11.85\ V\_130 \quad (5.10)$$

5.1.6 5.1.6 Surface roughness

The S/N response of overcut for Ti-35Nb-7Zr-5Ta and Ti-29Nb-13Ta-4.6Zr is illustrated in Figures 5.11 and 5.12, respectively, indicating an augmentation in the surface roughness with higher capacitance and gap voltage values. However, the amplified variances of the mean values of the Signal-to-Noise (S/N) ratios for capacitance hold a more significant sway compared to voltage. Utilizing Taguchi's orthogonal array with the "smaller-is-better" criteria, Equations 5.11 and 5.12 are formulated to present the regression equations for the average surface roughness for Ti-35Nb-7Zr-5Ta and Ti-29Nb-13Ta-4.6Zr, correspondingly.

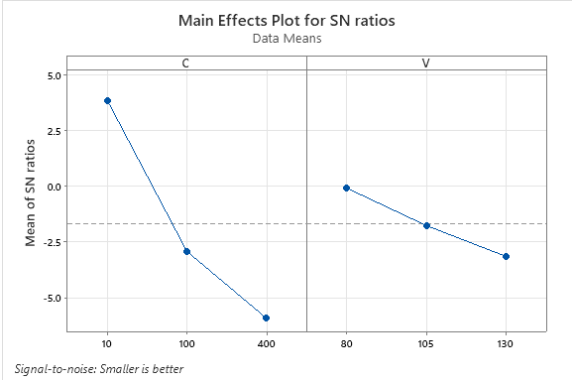

Figure 5.11: S/N response of surface roughness for µ-EDM for Ti-35Nb-7Zr-5Ta.

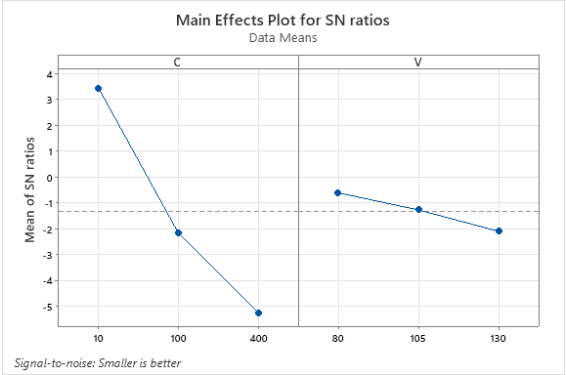

Figure 5.12: S/N response of surface roughness for µ-EDM for Ti-29Nb-13Ta-4.6Zr.

Regression equation:

$$\text{Surface roughness} = 1.3554 - 0.6938\ C\_10 + 0.0472\ C\_100 + 0.6466\ C\_400 - 0.2111\ V\_80 + 0.0042\ V\_105 + 0.2069\ V\_130 \quad (5.11)$$

Regression equation:

$$\text{Surface roughness} = 1.2679 - 0.5906\ C\_10 + 0.0188\ C\_100 + 0.5718\ C\_400 - 0.1086\ V\_80 + 0.0011\ V\_105 + 0.1074\ V\_130 \quad (5.12)$$

5.1.7 5.1.7 Optimal µ-EDM parameters

To analyze and estimate optimal machining parameters while considering multiple responses (MRR, overcut, crater size, circularity, microhardness, and surface roughness), Grey Relation Analysis (GRA) is employed. This technique involves several steps. Firstly, normalization of each output dataset is conducted based on the "larger-is-better" and "smaller-is-better" criteria. For data with Larger the better criteria, normalization is performed using the following equation:

$$y_i^*(k) = \frac{y(k) - min\ y_i(k)}{max\ y_i(k) - min\ y_i(k)} \quad (5.13)$$

Normalization of response parameters with criteria of lower the better can be expressed as:

$$y_i^*(k) = \frac{max\ y_i(k) - y(k)}{max\ y_i(k) - min\ y_i(k)} \quad (5.14)$$

Here, i stands for the experiment number, where k represents the data sample number. The notation $yi(k)$ refers to the measurement value of experiment i for data sample k, while max$yi(k)$ and min$yi(k)$ denote their respective maximum and minimum values. Subsequently, the deviation sequence can be expressed as:

$$\Delta_{oi}(k) = |y_o^*(k) - y_i^*(k)| \quad (5.15)$$

Additionally, the grey relation coefficient can be calculated by the following formula:

$$\zeta_i(k) = \frac{\Delta_{min} - \zeta.\Delta_{max}}{\Delta_{oi}(k) - \zeta.\Delta_{max}} \quad (5.16)$$

For this particular study the ζ is assumed to be 0.5. The grey relation grade (GRC) can be calculated by taking the average of all response grades, it can be expressed as:

$$Avg.GRC = \frac{1}{n}\sum_{k=1}^{n} \zeta_i(k) \quad (5.17)$$

Using equations (5.12-5.17), the Grey Relational Grade (GRG) for each response parameter was calculated and presented in Table 5.1 and 5.2 for micro-EDM of Ti-35Nb-7Zr-5Ta and Ti-29Nb-13Ta-4.6Zr respectively. According to these tables, experiment 1 exhibits the highest GRG compared to the other experiments. Consequently, machining parameters corresponding to capacitance 10nF and voltage 80V represent the most optimal condition for this experiment. Furthermore, the mean Signal-to-Noise (S/N) ratios of GRG for each experiment for micro-EDM of Ti-35Nb-7Zr-5Ta and Ti-29Nb-13Ta-4.6Zr are provided in Table 5.3 and 5.4 respectively. Based on these tables, the most optimal parameter set, determined through Grey Relation Analysis (GRA), corresponds to capacitance 10nF and voltage 80V, which aligns with experiment 1.

Table 5.1: Grey relation coefficient for μ-EDM of Ti-35Nb-7Zr-5Ta.

Exp. #	MRR	Hardness	Circula-rity	Overcut	Surface roughness	Crater size	GRC	Rank
1	0.351908	0.333333	1	1	1	1	0.780874	1
2	0.374003	0.572581	0.735189	0.817363	0.83939	0.819758	0.693047	2
3	0.387869	0.696078	0.562512	0.78287	0.712219	0.748113	0.648277	3
4	0.502764	0.464052	0.53741	0.520791	0.518426	0.420881	0.494054	8
5	0.646339	0.5	0.513745	0.466757	0.509393	0.40787	0.507351	7
6	0.709949	0.898734	0.424522	0.385725	0.480853	0.384723	0.547418	5
7	0.808619	0.645455	0.347823	0.434763	0.451605	0.417675	0.517657	6
8	0.333333	0.922078	0.333505	0.373532	0.37323	0.371463	0.45119	9
9	1	1	0.333333	0.333333	0.333333	0.333333	0.555556	4

Table 5.2: Grey relation coefficient for μ-EDM of Ti-29Nb-13Ta-4.6Zr.

Exp. #	MRR	Hardness	Circula-rity	Overcut	Surface roughness	Crater size	GRC	Rank
1	0.33333	0.33333	1.00000	1.00000	1.00000	1.00000	0.77778	1
2	0.34848	0.43871	0.71626	0.90970	0.95238	0.96972	0.72254	2
3	0.36108	0.67327	0.64486	0.69249	0.82450	0.87531	0.67859	3
4	0.43530	0.45638	0.54617	0.57951	0.52632	0.76807	0.55196	6
5	0.61016	0.51128	0.52141	0.49305	0.51737	0.67765	0.55515	5
6	0.70495	1.00000	0.43579	0.41244	0.48985	0.54674	0.59830	4
7	0.59437	0.71579	0.35875	0.50680	0.41176	0.49913	0.51443	9
8	0.71075	0.97141	0.34558	0.36910	0.35515	0.44817	0.53336	8
9	1.00000	0.91892	0.33333	0.33333	0.33333	0.33333	0.54204	7

Table 5.3: S/N response of GRC for μ-EDM of Ti-35Nb-7Zr-5Ta.

Level	Capacitance	Voltage
1	0.7074	0.5975
2	0.5163	0.5505
3	0.5081	0.5838
Delta	0.1993	0.047
Rank	1	2

Table 5.4: S/N response of GRC for µ-EDM of Ti-29Nb-13Ta-4.6Zr.

Level	Capacitance	Voltage
1	0.7263	0.6147
2	0.5685	0.6037
3	0.5299	0.6063
Delta	0.1964	0.011
Rank	1	2

5.2 Optimization of Micro-WEDM response parameters

5.2.1 Hardness

From Figure 5.13 and 5.14 shows the S/N response of material removal rate for Ti-35Nb-7Zr-5Ta and Ti-29Nb-13Ta-4.6Zr respectively, it is evident that surface microhardness increases with higher values of capacitance and gap voltage. However, the higher variances of the mean values of the Signal-to-Noise (S/N) ratios for capacitance have a greater impact compared to voltage. By applying the "larger-is-better" criteria to Taguchi's orthogonal array. Equation 5.18 and 5.19 presents the regression equation for average surface microhardness for Ti-35Nb-7Zr-5Ta and Ti-29Nb-13Ta-4.6Zr respectively. Where C_1, C_10, and C_100 represents the capacitance 1nF, 10nF, and 100nF respectively, in addition, V_80,V_95, and V_110 represents the voltage level of 80V, 95V, and 110V respectively.

Figure 5.13: S/N response for surface microhardness for µ-WEDM for Ti-35Nb-7Zr-5Ta.

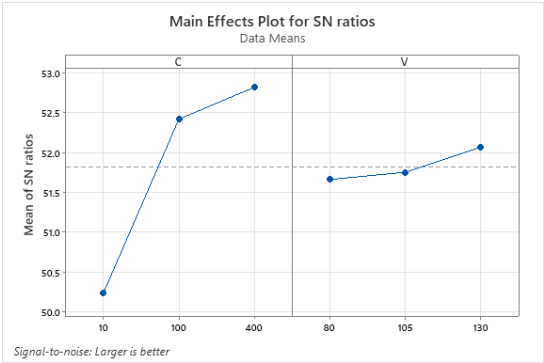

Figure 5.14: S/N response for surface microhardness for µ-WEDM for Ti-29Nb-13Ta-4.6Zr.

Regression equation:

$$\text{Hardness} = 366.19 - 13.52\ C\_1 - 1.63\ C\_10 + 15.15\ C\_100 - 26.07\ V\_80 - 1.85\ V\_95 + 27.93\ V\_110 \quad (5.18)$$

Regression equation:

$$\text{Hardness} = 393.37 - 67.93\ C\_1 + 24.19\ C\_10 + 43.74\ C\_100 - 6.37\ V\_80 - 3.70\ V\_95 + 10.07\ V\_110 \quad (5.19)$$

5.2.2 Kerf width

From Figure 5.15 and 5.16 displays the S/N response of overcut for Ti-35Nb-7Zr-5Ta and Ti-29Nb-13Ta-4.6Zr respectively, it is evident that kerf width of µ-cuts increases with higher values of capacitance and gap voltage. However, the higher variances of the mean values of the Signal-to-Noise (S/N) ratios for capacitance have a greater impact compared to voltage. By applying the "smaller-is-better" criteria to Taguchi's orthogonal array. Equation 5.20 and 5.21 presents the regression equation for average kerf width for Ti-35Nb-7Zr-5Ta and Ti-29Nb-13Ta-4.6Zr respectively.

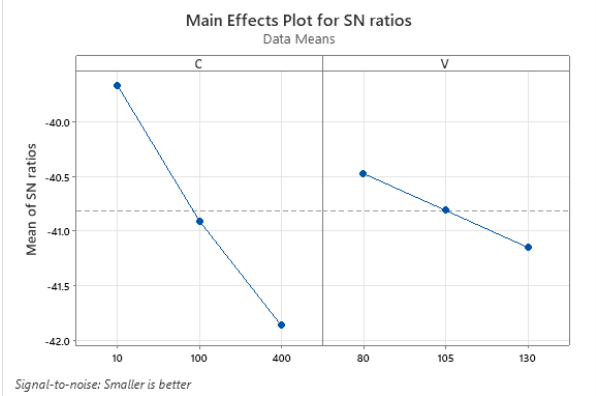

Figure 5.15: S/N response for kerf width for µ-WEDM for Ti-35Nb-7Zr-5Ta.

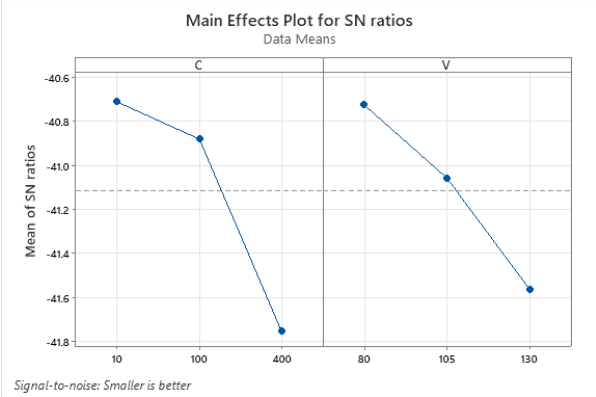

Figure 5.16: S/N response for kerf width for µ-WEDM for Ti-29Nb-13Ta-4.6Zr.

Regression equation:

$$\text{Overcut} = 110.48 - 14.18\ C\_1 + 0.70\ C\_10 + 13.48\ C\_100 - 4.16\ V\_80 - 0.10\ V\_95 + 4.26\ V\_110 \quad (5.20)$$

Regression equation:

$$\text{Overcut} = 113.989 - 5.38\ C\_1 - 3.20\ C\_10 + 8.57\ C\_100 - 5.09\ V\_80 - 0.94\ V\_95 + 6.03\ V\_110 \quad (5.21)$$

5.2.3 Surface roughness

The S/N response of overcut for Ti-35Nb-7Zr-5Ta and Ti-29Nb-13Ta-4.6Zr is illustrated in Figures 5.17 and 5.18, respectively, indicating an augmentation in the surface roughness with higher capacitance and gap voltage values. However, the amplified variances of the mean values of the Signal-to-Noise (S/N) ratios for capacitance hold a more significant sway compared to voltage. Utilizing Taguchi's orthogonal array with the "smaller-is-better" criteria, Equations 5.22 and 5.23 are formulated to present the regression equations for the average surface roughness for Ti-35Nb-7Zr-5Ta and Ti-29Nb-13Ta-4.6Zr, correspondingly.

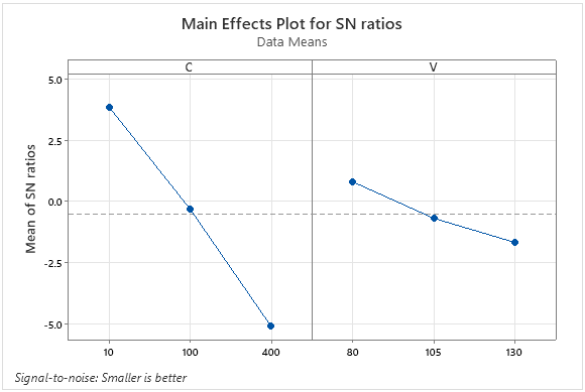

Figure 5.17: S/N response of surface roughness for µ-WEDM for Ti-35Nb-7Zr-5Ta.

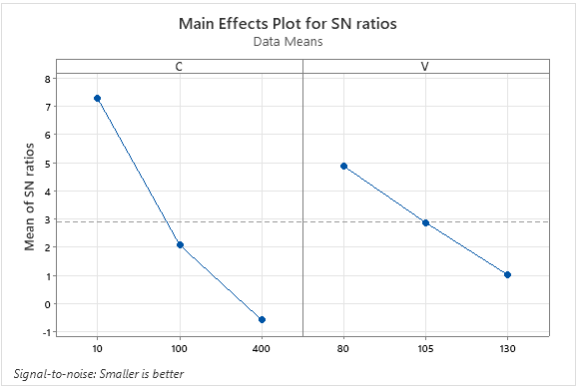

Figure 5.18: S/N response of surface roughness for µ-WEDM for Ti-29Nb-13Ta-4.6Zr.

Regression equation:

$$\text{Surface roughness} = 1.1679 - 0.5139\ C\_1 - 0.1272\ C\_10 + 0.6411\ C\_100 - 0.1459\ V\_80 - 0.0102\ V\_95 + 0.1561\ V\_110 \quad (5.22)$$

Regression equation:

$$\text{Surface roughness} = 0.7858 - 0.346\ C\_1 + 0.004\ C\_10 + 0.342\ C\_100 - 0.182\ V\_80 - 0.027\ V\_95 + 0.210\ V\_110 \quad (5.23)$$

5.2.4 Crater size

From Figures 5.19 and 5.20, it is observed that the Signal-to-Noise (S/N) response of crater size for Ti-35Nb-7Zr-5Ta and Ti-29Nb-13Ta-4.6Zr respectively showcases an increase in the crater size during µ-WEDM of µ-cuts with higher values of capacitance and gap voltage. Nonetheless, the higher variances of the mean values of the S/N ratios for capacitance exert a more pronounced impact compared to voltage. By employing the "smaller-is-better" criteria to Taguchi's orthogonal array, Equations 5.24 and 5.25 present the regression equations for the average crater size for Ti-35Nb-7Zr-5Ta and Ti-29Nb-13Ta-4.6Zr respectively.

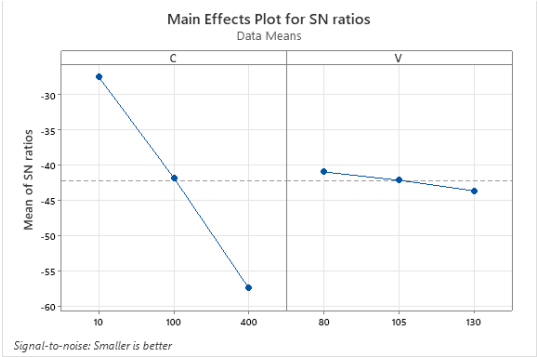

Figure 5.19: S/N response for crater size for µ-WEDM for Ti-35Nb-7Zr-5Ta.

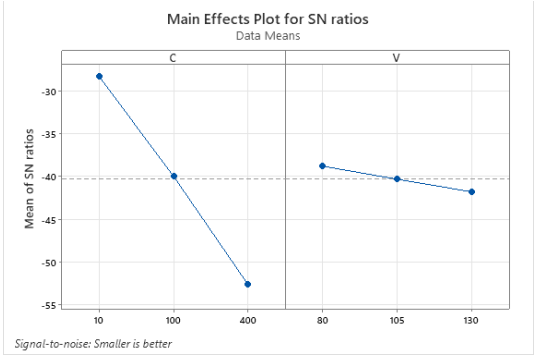

Figure 5.20: S/N response for overcut for µ-WEDM for Ti-29Nb-13Ta-4.6Zr.

Regression equation:

$$\text{Crater size} = 298.7 - 274.7\ C\_1 - 175.7\ C\_10 + 450.4\ C\_100 - 40.1\ V\_80 - 12.9\ V\_95 + 53.0\ V\_110 \quad (34)$$

Regression equation:

$$\text{Crater size} = 186.01 - 159.68\ C\_1 - 84.18\ C\_10 + 243.85\ C\_100 - 23.45\ V\_80 - 2.23\ V\_95 + 25.68\ V\_110 \quad (35)$$

5.2.5 Optimal µ-EDM parameters

To analyze and estimate optimal machining parameters while considering multiple responses (MRR, overcut, crater size, circularity, microhardness, and surface roughness), Grey Relation Analysis (GRA) is employed. Using equations (5.12-5.17), the Grey Relational Grade (GRG) for each response parameter was calculated and presented in Table 5.5 and 5.6 for micro-WEDM of Ti-35Nb-7Zr-5Ta and Ti-29Nb-13Ta-4.6Zr respectively. According to these tables, experiment 1 exhibits the highest GRG compared to the other experiments. Consequently, machining parameters corresponding to capacitance 1nF and voltage 80V represent the most optimal condition for this experiment. Furthermore, the mean Signal-to-Noise (S/N) ratios of GRG for each experiment for micro-WEDM of Ti-35Nb-7Zr-5Ta and Ti-29Nb-13Ta-4.6Zr are provided in Table 5.7 and 5.8 respectively. Based on these tables, the most optimal parameter set, determined through Grey Relation Analysis (GRA), corresponds to capacitance 1nF and voltage 80V, which aligns with experiment 1.

Table 5.5: Grey relation coefficient for µ-WEDM of Ti-35Nb-7Zr-5Ta.

Exp. #	Hardness	Kerf width	Surface roughness	Crater size	GRC	Rank
1	0.333333	1	1	1	0.833333	1
2	0.52	0.895288	0.799298	0.987336	0.80048	2
3	0.554098	0.7125	0.746136	0.978328	0.747766	3
4	0.44591	0.644472	0.643117	0.821675	0.638794	4
5	0.468144	0.448819	0.582024	0.813809	0.578199	6
6	0.582759	0.425373	0.563495	0.786301	0.589482	5
7	0.464286	0.36669	0.412801	0.410664	0.41361	8
8	0.488439	0.37804	0.39696	0.384842	0.41207	9
9	1	0.333333	0.333333	0.333333	0.5	7

Table 5.6: Grey relation coefficient for µ-WEDM of Ti-29Nb-13Ta-4.6Zr.

Exp. #	Hardness	Kerf width	Surface roughness	Crater size	GRC	Rank
1	0.333333	1	1	1	0.833333	1
2	0.363554	0.771838	0.860179	0.979179	0.743687	3
3	0.400599	0.639766	0.790055	0.962249	0.698167	4
4	0.73309	0.991506	0.635367	0.800675	0.790159	2
5	0.667221	0.657364	0.576871	0.746135	0.661898	5
6	0.800399	0.552865	0.570732	0.681284	0.65132	6
7	0.893096	0.522938	0.618453	0.383211	0.604424	7
8	0.897092	0.495304	0.495572	0.360086	0.562013	8
9	1	0.333333	0.333333	0.333333	0.5	9

Table 5.7: S/N response of GRC for μ-WEDM of Ti-35Nb-7Zr-5Ta.

Level	Capacitance	Voltage
1	0.7243	0.6077
2	0.6565	0.599
3	0.4243	0.5984
Delta	0.3	0.0092
Rank	1	2

Table 5.8: S/N response of GRC for μ-WEDM of Ti-29Nb-13Ta-4.6Zr.

Level	Capacitance	Voltage
1	0.7134	0.7102
2	0.7183	0.6427
3	0.5304	0.6092
Delta	0.1879	0.1011
Rank	1	2

Chapter 6: Conclusions

Micro-electrical discharge machining (μ-EDM) stands as a pivotal non-traditional method in precision manufacturing, allowing for the fabrication of intricate microstructures with high accuracy. Response variables such as capacitance and voltage serve as critical metrics for assessing the efficacy and quality of the performance parameters during the machining process. The response variables often encompass key characteristics of the machined surface, such as surface roughness, material removal rate, circularity, overcut, microhardness, etc. of micro-EDM operations. The study on micro-electro-discharge machining of Ti-35Nb-7Zr-5Ta and Ti-29Nb-13Ta-4.6Zr for creating micro-holes on the surface has led to several important findings. The results of the experiment indicate a direct relationship between the enhancement of machining parameters and the process parameters. Several important features of the machining process exhibit improvements as the energy input in the micro-EDM process increases.

- Increase in capacitance from 10nF to 100nF at voltage levels 80V, 105V, and 130V increases the average material removal rate (MRR) for Ti-35Nb-7Zr-5Ta by 6.38, 4.45, and 3.773 times respectively. However, for Ti-29Nb-13Ta-4.6Zr the MRR increased by the factor of 4.098, 4.445, and 3.953. The increase in discharge energy can benefit the amount of material removed per spark, insufficient debris removal results in poor machinability.
- The volume of the crater is notably influenced by the pulse energy, with higher energy levels generally resulting in larger craters so larger surface roughness. An increase in capacitance from 10nF to 100nF at voltage 80V, 105V, and 130V increases the surface roughness of μ-holes during μ-EDM of Ti-35Nb-7Zr-5Ta by 1.803, 2.012, and 1.74 times respectively. However, for Ti-29Nb-13Ta-4.6Zr increased by the factor of 2.825, 2.102, and 1.74 respectively.
- Whereas the circularity of the hole decreases with an increase in energy. An increase in capacitance from 10nF to 100nF at voltage 80V, 105V, and 130V decreases the circularity of μ-holes during μ-EDM of Ti-35Nb-7Zr-5Ta by 1.099, 1.068, and 1.071 times respectively. However, for Ti-29Nb-13Ta-4.6Zr the circularity reduced by the factor of 1.10047, 1.0635, and 1.0953 respectively.

The investigation on micro-wire-electro-discharge machining (μ-WEDM) of Ti-35Nb-7Zr-5Ta and Ti-29Nb-13Ta-4.6Z on the surface has led to several important findings. The results of the experiment indicate a direct relationship between the enhancement of machining parameters and

the process parameters. Several important features of the machining process exhibit improvements as the C and V escalates input in the micro-EDM process increases.

- Augmentation in capacitance from 1nF to 10nF at voltage levels 80V, 95V, and 110V increases the average surface roughness for Ti-35Nb-7Zr-5Ta by 1.137, 0.967, and 1.013 times respectively. However, for Ti-29Nb-13Ta-4.6Zr the surface roughness increased by the factor of 2.825, 2.102, and 1.74 times respectively.
- Whereas the surface micro hardness of the machined surface increase with an increase in energy. An increase in capacitance from 10nF to 100nF at voltage 80V, 105V, and 130V increase the microhardness of machined surface during μ-WEDM of Ti-35Nb-7Zr-5Ta by 1.099, 1.068, and 1.071 times respectively. However, for Ti-29Nb-13Ta-4.6Zr the circularity reduced by the factor of 2.825, 1.019, and 1.02 times respectively.

The past research mentions the different theoretical thermal transient models of the μ-EDM process suggested different values for the heat percentage driven into the workpiece. However, this study demonstrates that these fractions are depending on the input process parameters rather than being constant. An experimental study using Ti-6Al-4V workpiece and μ-EDM provided important quantitative insights into the attainment of high plasma flushing efficiency. The regression equation for plasma flushing efficiency was developed based on numerical and experimental results for crater size. The model was then validated by experimental results conducted on individual discharges. High and low energy discharges were the main subject of comparisons between theoretical predictions and real experimental craters. Overall, the investigation discovered that during single pulse discharges, the constructed theoretical model accurately approximates the size of craters on the workpiece. The percentage error between experimental results and numerical prediction is less than 20%.

Chapter 7: References

[1]. Snoeys, R., Staelens, F., & Dekeyser, W. J. C. A. (1986). Current trends in non-conventional material removal processes. *CIRP annals*, *35*(2), 467-480.

[2]. Masuzawa, T. (2000). State of the art of micromachining. *Cirp Annals*, *49*(2), 473-488.

[3]. Yeo, S. H., & Tan, L. K. (1999). Effects of ultrasonic vibrations in micro electro-discharge machining of microholes. *Journal of Micromechanics and Microengineering*, *9*(4), 345.

[4]. Izquierdo, B., Sanchez, J. A., Plaza, S., Pombo, I., & Ortega, N. (2009). A numerical model of the EDM process considering the effect of multiple discharges. *International Journal of Machine Tools and Manufacture*, *49*(3-4), 220-229.

[5]. Pérez, R., Carron, J., Rappaz, M., Wälder, G., Revaz, B., & Flükiger, R. (2007, April). Measurement and metallurgical modeling of the thermal impact of EDM discharges on steel. In *Proceedings of the 15th International Symposium on Electromachining, ISEM XV* (pp. 17-22).

[6]. Wu, H., Ma, J., Meng, Q., Jahan, M. P., & Alavi, F. (2018). Numerical modeling of electrical discharge machining of Ti-6Al-4V. *Procedia Manufacturing*, *26*, 359-371.

[7]. Verma, A., & Kumar, S. (2022). Modeling and Simulation of Electrical Discharge Machining—A Review. *Advancement in Materials, Manufacturing and Energy Engineering, Vol. I: Select Proceedings of ICAMME 2021*, 241-248.

[8]. Kaur, M., & Singh, K. (2019). Review on titanium and titanium based alloys as biomaterials for orthopaedic applications. *Materials Science and Engineering: C*, *102*, 844-862.

[9]. Liu, X., Chu, P. K., & Ding, C. (2004). Surface modification of titanium, titanium alloys, and related materials for biomedical applications. *Materials Science and Engineering: R: Reports*, *47*(3-4), 49-121.

[10]. Leinenbach, C., & Eifler, D. (2006). Fatigue and cyclic deformation behaviour of surface-modified titanium alloys in simulated physiological media. *Biomaterials*, *27*(8), 1200-1208.

[11]. de Souza Soares, F. M., Barbosa, D. M., Corado, H. P. R., de Carvalho Santana, A. I., & Elias, C. N. (2022). Surface morphology, roughness, and corrosion resistance of dental implants produced by additive manufacturing. *Journal of Materials Research and Technology*, *21*, 3844-3855.

[12]. Kaseem, M., & Choe, H. C. (2020). Triggering the hydroxyapatite deposition on the surface of PEO-coated Ti–6Al–4V alloy via the dual incorporation of Zn and Mg ions. *Journal of Alloys and Compounds*, *819*, 153038.

[13]. Liang, S. (2020). Review of the design of titanium alloys with low elastic modulus as implant materials. *Advanced Engineering Materials*, *22*(11), 2000555.

[14]. Ratner, B. D., Hoffman, A. S., Schoen, F. J., & Lemons, J. E. (2004). *Biomaterials science: an introduction to materials in medicine*. Elsevier.

[15]. Geetha, M., Singh, A. K., Asokamani, R., & Gogia, A. K. (2009). Ti based biomaterials, the ultimate choice for orthopaedic implants–A review. *Progress in materials science*, *54*(3), 397-425.

[16]. Wintermantel, E., & Ha, S. W. (2009). *Medizintechnik: Life Science Engineering*. Springer Science & Business Media.

[17]. Omarov, S., Nauryz, N., Talamona, D., & Perveen, A. (2022). Surface Modification Techniques for Metallic Biomedical Alloys: A Concise Review. *Metals*, *13*(1), 82.

[18]. Long, M., & Rack, H. J. (1998). Titanium alloys in total joint replacement—a materials science perspective. *Biomaterials*, *19*(18), 1621-1639.

[19]. Laing, P. G., Ferguson Jr, A. B., & Hodge, E. S. (1967). Tissue reaction in rabbit muscle exposed to metallic implants. *Journal of Biomedical Materials Research*, *1*(1), 135-149.

[20]. Niinomi, M., Liu, Y., Nakai, M., Liu, H., & Li, H. (2016). Biomedical titanium alloys with Young's moduli close to that of cortical bone. *Regenerative biomaterials*, *3*(3), 173-185.

[21]. Ricci, V. P., dos Santos, R. F., Asato, G. H., Roche, V., Junior, A. M. J., & Afonso, C. R. (2021). Assessment of anodization conditions and annealing temperature on the microstructure, elastic modulus, and wettability of β-Ti40Nb alloy. *Thin Solid Films*, *737*, 138949.

[22]. Gupta, K., & Laubscher, R. F. (2017). Sustainable machining of titanium alloys: a critical review. *Proceedings of the Institution of Mechanical Engineers, Part B: Journal of Engineering Manufacture*, *231*(14), 2543-2560.

[23]. Park, J., & Lakes, R. S. (2007). *Biomaterials: an introduction*. Springer Science & Business Media.

[24]. Staiger, M. P., Pietak, A. M., Huadmai, J., & Dias, G. (2006). Magnesium and its alloys as orthopedic biomaterials: a review. *Biomaterials*, *27*(9), 1728-1734.

[25]. Sidambe, A. T. (2014). Biocompatibility of advanced manufactured titanium implants—A review. *Materials*, *7*(12), 8168-8188.

[26]. Eliaz, N. (2019). Corrosion of metallic biomaterials: A review. *Materials*, *12*(3), 407.

[27]. Abbas, N. M., Solomon, D. G., & Bahari, M. F. (2007). A review on current research trends in electrical discharge machining (EDM). *International Journal of machine tools and Manufacture*, *47*(7-8), 1214-1228.

[28]. Eastwood, M., McGrouther, D. A., & Brown, R. A. (1998). Fibroblast responses to mechanical forces. *Proceedings of the Institution of Mechanical Engineers, Part H: Journal of Engineering in Medicine*, *212*(2), 85-92.

[29]. Azad, M. S., & Puri, A. B. (2012). Simultaneous optimisation of multiple performance characteristics in micro-EDM drilling of titanium alloy. *The International Journal of Advanced Manufacturing Technology*, *61*, 1231-1239.

[30]. Sapkal, S. U., & Jagtap, P. S. (2018). Optimization of micro EDM drilling process parameters for titanium alloy by rotating electrode. *Procedia Manufacturing*, *20*, 119-126.

[31]. Kibria, G., B. R. Sarkar, B. B. Pradhan, and B. Bhattacharyya. "Comparative study of different dielectrics for micro-EDM performance during microhole machining of Ti-6Al-4V alloy." *The International Journal of Advanced Manufacturing Technology* 48 (2010): 557-570.

[32]. Pradhan, B. B., Masanta, M., Sarkar, B. R., & Bhattacharyya, B. (2009). Investigation of electro-discharge micro-machining of titanium super alloy. *The International Journal of Advanced Manufacturing Technology*, *41*, 1094-1106.

[33]. Wang, K., Zhang, Q., Zhu, G., & Zhang, J. (2018). Effects of tool electrode size on surface characteristics in micro-EDM. *The International Journal of Advanced Manufacturing Technology*, *96*, 3909-3916.

[34]. Yu, Z., Jun, T., & Masanori, K. (2004). Dry electrical discharge machining of cemented carbide. *Journal of materials processing technology*, *149*(1-3), 353-357.

[35]. Wang, Y., Zhou, X. J., & Hu, D. J. (2006). An experimental investigation of dry-electrical discharge assisted truing and dressing of metal bonded diamond wheel. *International Journal of Machine Tools and Manufacture*, *46*(3-4), 333-342.

[36]. Ramani, V., & Cassidenti, M. L. (1985). Inert-gas electrical discharge machining. *NASA Tech Briefs*, *8*(MFS-19778).

[37]. Eastwood, M., McGrouther, D. A., & Brown, R. A. (1998). Fibroblast responses to mechanical forces. *Proceedings of the Institution of Mechanical Engineers, Part H: Journal of Engineering in Medicine*, *212*(2), 85-92.

[38]. Jeon, Y., Park, H. W., & Lee, C. M. (2013). Current research trends in external energy assisted machining. *International Journal of Precision Engineering and Manufacturing*, *14*, 337-342.

[39]. Mujumdar, S. S., Mastud, S. A., Singh, R. K., & Joshi, S. S. (2010). Experimental characterization of the reverse micro-electrodischarge machining process for fabrication of high-aspect-ratio micro-rod arrays. *Proceedings of the Institution of Mechanical Engineers, Part B: Journal of Engineering Manufacture*, *224*(5), 777-794.

[40]. Tiwary, A. P., Pradhan, B. B., & Bhattacharyya, B. (2015). Study on the influence of micro-EDM process parameters during machining of Ti–6Al–4V superalloy. *The International Journal of Advanced Manufacturing Technology*, *76*, 151-160.

[41]. Feng, W., Chu, X., Hong, Y., & Zhang, L. (2018). Studies on the surface of high-performance alloys machined by micro-EDM. *Materials and Manufacturing Processes*, *33*(6), 616-625.

[42]. Al-Ahmari, A. M. A., Rasheed, M. S., Mohammed, M. K., & Saleh, T. (2016). A hybrid machining process combining micro-EDM and laser beam machining of nickel–titanium-based shape memory alloy. *Materials and Manufacturing Processes*, *31*(4), 447-455.

[43]. Dewangan, S., Kumar, S. D., Jha, S. K., & Biswas, C. K. (2020). Optimization of Micro-EDM drilling parameters of Ti–6Al–4V alloy. *Materials Today: Proceedings*, *33*, 5481-5485.

[44]. Singh, R., Dvivedi, A., & Kumar, P. (2020). EDM of high aspect ratio micro-holes on Ti-6Al-4V alloy by synchronizing energy interactions. *Materials and Manufacturing Processes*, *35*(11), 1188-1203.

[45]. Chen, S. G., Lian, M. Q., Wu, X. Y., Lei, J. G., Zhao, H., Peng, T. J., ... & Xu, B. (2021). Study on the micro-EDM processing characteristics of Ti-6Al-4V alloy with different electrode materials. *The International Journal of Advanced Manufacturing Technology*, *116*, 3369-3376.

[46]. Rao, M. S., & Venkaiah, N. (2013). Review on wire-cut EDM process. *International Journal of Advanced Trends in Computer Science and Engineering*, *2*(6), 12-17.

[47]. Kumar, Naveen, Soni Kumari, Kumar Abhishek, Goutam Nandi, and Nabendu Ghosh. "Study on various parameters of WEDM using different optimization techniques: A review." *Materials Today: Proceedings* 62 (2022): 4018-4024.

[48]. Manna, A., & Bhattacharyya, B. (2006). Taguchi and Gauss elimination method: a dual response approach for parametric optimization of CNC wire cut EDM of PRAlSiCMMC. *The International Journal of Advanced Manufacturing Technology*, *28*, 67-75.

[49]. Singh, H., & Garg, R. (2009). Effects of process parameters on material removal rate in WEDM. *Journal of achievements in materials and manufacturing engineering*, *32*(1), 70-74.

[50]. Aravind, S. N., Sowmya, S., & Yuvaraj, K. P. (2012, March). Optimization of metal removal Rate and surface roughness on Wire EDM using Taguchi method. In *IEEE-International Conference On Advances In Engineering, Science And Management (ICAESM-2012)* (pp. 155-159). IEEE.

[51]. Kumar, A., Kumar, V., & Kumar, J. (2016). Investigation of micro-cracks susceptibility on machined pure titanium surface in WEDM process. *Journal for Manufacturing Science and Production*, *16*(2), 123-139.

[52]. Parashar, V., Rehman, A., & Bhagoria, J. L. (2012). Performance Measurement and Data Analysis of Material Removal Rate for Wire Cut Electro Discharge Machining Process. *Applied Mechanics and Materials*, *110*, 1683-1690.

[53]. Erdem, O., Cogun, C., Uslan, I., & Erbas, M. (2020). Thermo-fluid multi-physics modeling and experimental verification of volumetric workpiece material removal by a discharge pulse in electric discharge machining process. *Journal of Physics D: Applied Physics*, *53*(39), 395501.

[54]. Snoeys, R. (1971). Investigations of EDM operations by means of thermomathematical models. *Annals of the CIRP*, *20*, 35-36.

[55]. Van Dijck, F. S., & Dutre, W. L. (1974). Heat conduction model for the calculation of the volume of molten metal in electric discharges. *Journal of Physics D: Applied Physics*, *7*(6), 899.

[56]. DiBitonto, D. D., Eubank, P. T., Patel, M. R., & Barrufet, M. A. (1989). Theoretical models of the electrical discharge machining process. I. A simple cathode erosion model. *Journal of applied physics*, *66*(9), 4095-4103.

[57]. Pandey, P. C., & Jilani, S. T. (1986). Plasma channel growth and the resolidified layer in EDM. *Precision Engineering*, *8*(2), 104-110.

[58]. Salah, N. B., Ghanem, F., & Atig, K. B. (2006). Numerical study of thermal aspects of electric discharge machining process. *International Journal of Machine Tools and Manufacture*, *46*(7-8), 908-911.

[59]. Kansal, H. K., Singh, S., & Kumar, P. (2008). Numerical simulation of powder mixed electric discharge machining (PMEDM) using finite element method. *Mathematical and Computer Modelling*, *47*(11-12), 1217-1237.

[60]. Ummethala, R., Karamched, P. S., Rathinavelu, S., Singh, N., Aggarwal, A., Sun, K., ... & Prashanth, K. G. (2020). Selective laser melting of high-strength, low-modulus Ti–35Nb–7Zr–5Ta alloy. *Materialia*, *14*, 100941.

[61]. Niinomi, M. (2003). Fatigue performance and cyto-toxicity of low rigidity titanium alloy, Ti–29Nb–13Ta–4.6 Zr. *Biomaterials*, *24*(16), 2673-2683.

[62]. Meena, V. K., Azad, M. S., Singh, S., & Singh, N. (2017). Micro-EDM multiple parameter optimization for Cp titanium. *The International Journal of Advanced Manufacturing Technology*, *89*, 897-904.

[63]. Tiwary, A. P., Pradhan, B. B., & Bhattacharyya, B. (2018). Investigation on the effect of dielectrics during micro-electro-discharge machining of Ti-6Al-4V. *The International Journal of Advanced Manufacturing Technology*, *95*, 861-874.

[64]. Jahan, M. P., Wong, Y. S., & Rahman, M. (2009). A study on the quality micro-hole machining of tungsten carbide by micro-EDM process using transistor and RC-type pulse generator. *Journal of materials processing technology*, *209*(4), 1706-1716.

[65]. Bruyere, V., Touvrey, C., & Namy, P. (2014). A phase field approach to model laser power control in spot laser welding. In *COMSOL Conference* (Vol. 213, pp. 1-6).

[66]. Tang, J., & Yang, X. (2018). Simulation investigation of thermal phase transformation and residual stress in single pulse EDM of Ti–6Al–4V. *Journal of Physics D: Applied Physics*, *51*(13), 135308.

[67]. Joshi, S. N., & Pande, S. S. (2010). Thermo-physical modeling of die-sinking EDM process. *Journal of manufacturing processes*, *12*(1), 45-56.

[68]. Yeo, S. H., Kurnia, W., & Tan, P. C. (2007). Electro-thermal modelling of anode and cathode in micro-EDM. *Journal of Physics D: Applied Physics*, *40*(8), 2513.

[69]. Tang, L., Ji, Y., Ren, L., Zhai, K. G., Huang, T. Q., Fan, Q. M., ... & Liu, J. (2019). Thermo-electrical coupling simulation of powder mixed EDM SiC/Al functionally graded materials. *The International Journal of Advanced Manufacturing Technology*, *105*, 2615-2628.

[70]. Jahan, M. P., Wong, Y. S., & Rahman, M. (2010). A comparative experimental investigation of deep-hole micro-EDM drilling capability for cemented carbide (WC-Co) against austenitic stainless steel (SUS 304). *The International Journal of Advanced Manufacturing Technology*, *46*, 1145-1160.

[71]. Jahan, M. P., & Alavi, F. (2019). A study on the surface composition and migration of materials and their effect on surface microhardness during micro-EDM of Ti-6Al-4V. *Journal of Materials Engineering and Performance*, *28*, 3517-3530.

[72]. Aich, U. (2018). Investigation for the presence of chaos in surface topography generated by EDM. *Tribology International*, *120*, 411-433.

[73]. Jithin, S., Bhandarkar, U. V., & Joshi, S. S. (2017). Analytical simulation of random textures generated in electrical discharge texturing. *Journal of Manufacturing Science and Engineering*, *139*(11), 111002.

Chapter 8: Appendices

Table A.1: MRR

	Estimate	**SE**	**tstat**	**pvalue**
Intercept	3.2472e+06	3.5371e+05	9.1804	0.002733
x1: Capacitance	1.7506e+06	2.1149e+05	8.2774	0.0036934
x2: Voltage	2.764e+05	1.3076e+05	2.1138	0.12492
x1: x2	-46129	1.3869e+05	-0.33259	0.76133
$x1^2$	-1.4644e+06	3.1723e+05	-4.6161	0.019132
$x2^2$	79496	1.9614e+05	0.4053	0.71243
R^2 = 0.965	**Adj. R^2 = 0.907**			

Table A.2: Overcut

	Estimate	**SE**	**tstat**	**pvalue**
Intercept	40.248	1.2855	31.309	7.1594e-05
x1: Capacitance	11.523	0.76862	14.991	0.00064424
x2: Voltage	2.7244	0.47523	5.7327	0.010538
x1: x2	0.71449	0.50406	1.4175	0.25135
$x1^2$	-9.4118	1.1529	-8.1633	0.0038449
$x2^2$	0.018125	0.71285	0.025426	0.98131
R^2 = 0.99	**Adj. R^2 = 0.973**			

Table A.3: Crater Area

	Estimate	**SE**	**tstat**	**pvalue**
Intercept	1185.4	29.045	40.811	3.2374e-05
x1: Capacitance	536.56	17.366	30.896	7.4492e-05
x2: Voltage	80.869	10.737	7.5315	0.0048521
x1: x2	30.815	11.389	2.7057	0.073431
$x1^2$	-524.24	26.049	-20.125	0.00026818
$x2^2$	-1.2765	16.106	-0.079255	0.94182
R^2 = 0.997	**Adj. R^2 = 0.993**			

Table A.4: Circularity

	Estimate	**SE**	**tstat**	**pvalue**
Intercept	0.78171	0.0079398	98.455	2.3099e-06
x1: Capacitance	-0.083081	0.0047473	-17.501	0.00040666
x2: Voltage	-0.019527	0.0029352	-6.6528	0.0069218
x1: x2	0.011584	0.0031133	3.7209	0.033786
$x1^2$	0.034839	0.007121	4.8925	0.016336
$x2^2$	-0.0031337	0.0044028	-0.71176	0.52797
R^2 = 0.995	**Adj. R^2 = 0.986**			

Table A.5: Microhardness

	Estimate	**SE**	**tstat**	**pvalue**
Intercept	324.21	6.7591	47.967	1.9951e-05
x1: Capacitance	10.303	4.0413	2.5493	0.083991
x2: Voltage	10.777	2.4987	4.313	0.022955
x1: x2	-4.2757	2.6503	-1.6133	0.20509

$x1^2$	-2.9897	6.062	-0.49318	0.65573
$x2^2$	-1.7497	3.7481	-0.46684	0.67243
R^2 = 0.919	**Adj. R^2 = 0.783**			

Table A.6: Surface roughness

	Estimate	**SE**	**tstat**	**pvalue**
Intercept	1.8041	0.10333	17.461	0.00040942
x1: Capacitance	0.80571	0.061779	13.042	0.00097354
x2: Voltage	0.181	0.038198	4.7385	0.017822
x1: x2	0.090625	0.040515	2.2368	0.11129
$x1^2$	-0.50004	0.092669	-5.396	0.012474
$x2^2$	-0.00475	0.057297	-0.082902	0.93915
R^2 = 0.989	**Adj. R^2 = 0.969**			

Table A.7: MRR

	Estimate	**SE**	**tstat**	**pvalue**
Intercept	3.26E+06	3.07E+05	10.632	0.0017781
x1: Capacitance	1.66E+06	1.83E+05	9.0514	0.0028481
x2: Voltage	4.17E+05	1.13E+05	3.6786	0.034791
x1: x2	86746	1.20E+05	0.72115	0.52293
$x1^2$	-1.39E+06	2.75E+05	-5.0584	0.014909
$x2^2$	-67902	1.70E+05	-0.39916	0.71649
R^2 = 0.973	**Adj. R^2 = 0.927**			

Table A.8: Overcut

	Estimate	**SE**	**tstat**	**pvalue**
Intercept	36.752	1.7656	20.815	0.000243
x1: Capacitance	12.83	1.0557	12.153	0.001199
x2: Voltage	4.5539	0.65272	6.9767	0.006044
x1: x2	1.5512	0.69231	2.2406	0.1109
$x1^2$	-9.4307	1.5835	-5.9555	0.009469
$x2^2$	-0.19292	0.97908	-0.19704	0.85639
R^2 = 0.987	**Adj. R^2 = 0.966**			

Table A.9: Crater Area

	Estimate	**SE**	**tstat**	**pvalue**
Intercept	858.91	97.76	8.7859	0.0031062
x1: Capacitance	701.57	58.452	12.002	0.0012443
x2: Voltage	244.64	36.14	6.7691	0.0065883
x1: x2	158.34	38.333	4.1307	0.02574
$x1^2$	-194.75	87.678	-2.2212	0.11292
$x2^2$	101.79	54.211	1.8777	0.15705
R^2 = 0.991	**Adj. R^2 = 0.977**			

Table A.10: Circularity

	Estimate	**SE**	**tstat**	**pvalue**
Intercept	0.79567	0.0087832	90.589	2.97E-06
x1: Capacitance	-0.089947	0.0052516	-17.128	0.000434
x2: Voltage	-0.018331	0.003247	-5.6454	0.011

x1: x2	0.006813	0.003444	1.9782	0.1423
$x1^2$	0.040126	0.0078774	5.0938	0.014627
$x2^2$	-0.000625	0.0048705	-0.12832	0.90601
R^2 = 0.994	**Adj. R^2 = 0.984**			

Table A.11: Microhardness

	Estimate	**SE**	**tstat**	**pvalue**
Intercept	323.64	4.1672	77.663	4.71E-06
x1: Capacitance	14.14	2.4916	5.6752	0.010839
x2: Voltage	9.8631	1.5405	6.4023	0.0077192
x1: x2	-5.301	1.634	-3.2442	0.047699
$x1^2$	-7.5935	3.7374	-2.0318	0.13511
$x2^2$	1.0418	2.3108	0.45081	0.68271
R^2 = 0.971	**Adj. R^2 = 0.922**			

Table A.12: Surface roughness

	Estimate	**SE**	**tstat**	**pvalue**
Intercept	1.6202	0.050617	32.009	6.70E-05
x1: Capacitance	0.68346	0.030265	22.583	0.00019015
x2: Voltage	0.093531	0.018712	4.9983	0.015407
x1: x2	0.056221	0.019848	2.8326	0.066046
$x1^2$	-0.39511	0.045397	-8.7034	0.0031925
$x2^2$	-0.00125	0.028069	-0.044534	0.96728
R^2 = 0.971	**Adj. R^2 = 0.922**			

Table A.13: Kerf width

	Estimate	**SE**	**tstat**	**pvalue**
Intercept	140.87	7.2435	19.448	0.00029696
x1: Capacitance	32.783	5.2045	6.299	0.0080835
x2: Voltage	3.6421	1.2719	2.8636	0.064386
x1: x2	-1.1076	1.349	-0.82107	0.47177
$x1^2$	-34.309	7.8068	-4.3948	0.021832
$x2^2$	0.1125	1.9078	0.058969	0.95669
R^2 = 0.97	**Adj. R^2 = 0.921**			

Table A.14: Crater size

	Estimate	**SE**	**tstat**	**pvalue**
Intercept	367.52	38.42	9.5658	0.0024237
x1: Capacitance	399.61	27.605	14.476	0.0007147
x2: Voltage	40.32	6.7461	5.9768	0.0093743
x1: x2	49.661	7.1553	6.9404	0.0061344
$x1^2$	-91.872	41.408	-2.2187	0.11318
$x2^2$	14.464	10.119	1.4294	0.24823
R^2 = 0.999	**Adj. R^2 = 0.971**			

Table A.15: Surface microhardness

	Estimate	**SE**	**tstat**	**pvalue**
Intercept	387.23	43.077	8.9892	0.0029059
x1: Capacitance	28.398	30.951	0.91752	0.42653

x2: Voltage	23.383	7.5638	3.0914	0.053655
x1: x2	2.9797	8.0226	0.37142	0.73501
$x1^2$	-25.76	46.427	-0.55485	0.61768
$x2^2$	2.0833	11.346	0.18362	0.86602
R^2 = 0.806	**Adj. R^2 = 0.402**			

Table A.16: Surface roughness

	Estimate	**SE**	**tstat**	**pvalue**
Intercept	1.8524	0.17478	10.599	0.0017947
x1: Capacitance	0.99825	0.12558	7.9489	0.0041528
x2: Voltage	0.13077	0.03069	4.261	0.023707
x1: x2	0.049659	0.032551	1.5256	0.22454
$x1^2$	-0.78163	0.18837	-4.1493	0.025436
$x2^2$	0.0115	0.046034	0.24981	0.81886
R^2 = 0.99	**Adj. R^2 = 0.973**			

Table A.17: Kerf width

	Estimate	**SE**	**tstat**	**pvalue**
Intercept	115.3	5.584	20.648	2.48E-04
x1: Capacitance	8.1202	4.0121	2.0239	0.13614
x2: Voltage	4.819	0.98047	4.9149	0.016133
x1: x2	1.2434	1.0399	1.1956	0.31774
$x1^2$	-2.527	6.0182	-0.41989	0.70283
$x2^2$	1.0575	1.4707	0.71905	0.52406
R^2 = 0.959	**Adj. R^2 = 0.89**			

Table A.18: Crater size

	Estimate	**SE**	**tstat**	**pvalue**
Intercept	279.52	20.882	13.386	0.00090126
x1: Capacitance	254.59	15.004	16.969	0.00044579
x2: Voltage	21.278	3.6665	5.8032	0.010183
x1: x2	13.45	3.8889	3.4585	0.040685
$x1^2$	-107.71	22.505	-4.7861	0.017344
$x2^2$	2.5104	5.4998	0.45646	0.67908
R^2 = 0.999	**Adj. R^2 = 0.997**			

Table A.19: Surface microhardness

	Estimate	**SE**	**tstat**	**pvalue**
Intercept	591.83	16.834	35.157	5.06E-05
x1: Capacitance	183	12.096	15.13	0.0006269
x2: Voltage	7.1207	2.9559	2.409	0.095104
x1: x2	-3.1339	3.1352	-0.99958	0.39118
$x1^2$	-227.44	18.143	-12.536	0.0010944
$x2^2$	4.1667	4.4338	0.93975	0.41667
R^2 = 0.991	**Adj. R^2 = 0.975**			

Table A.20: Surface roughness

	Estimate	**SE**	**tstat**	**pvalue**
Intercept	1.4674	0.18609	7.8854	0.0042502
x1: Capacitance	0.78353	0.13371	5.8601	0.0099085
x2: Voltage	0.1697	0.032675	5.1935	0.013866
x1: x2	0.16035	0.034657	4.6267	0.019013
$x1^2$	-0.79746	0.20056	-3.9762	0.02845
$x2^2$	0.030637	0.049012	0.6251	0.57622
R^2 = 0.978	**Adj. R^2 = 0.941**			